

Geothermal systems in Indonesia – Influence on the corrosion resistance of stainless steel materials

vorgelegt von

Dipl.-Ing. Amela Keserović

aus Nikšić

von der Fakultät VI - Planen Bauen Umwelt
der Technischen Universität Berlin
zur Erlangung des akademischen Grades

Doktor der Ingenieurwissenschaften

- Dr.-Ing. -

Genehmigte Dissertation

Promotionsausschuss:

Vorsitzender: Prof. Dr. Wilhelm Dominik

Gutachter: Prof. Dr. Uwe Tröger

Gutachter: Prof. Dr. Ernst Huenges

Gutachter: Dr. Ralph Bäßler

Tag der wissenschaftlichen Aussprache: 28. Mai 2014

Berlin 2014

This thesis is dedicated to my father and my role model,

Dr. Hazim Keserović,

for his early inspiration, motivation and enthusiasm...

Table of Contents

Chapter 1	Introduction	1
Chapter 2	State of the Art	5
2.1	Geothermal energy.....	5
2.1.1	Geothermal hotspots.....	5
2.1.2	Utilization - electricity generation.....	6
2.1.3	Geothermal energy in Indonesia	7
2.1.3.1	Sibayak.....	8
2.1.3.2	Lahendong.....	8
2.2	Corrosion on geothermal power plants	9
2.2.1	Construction materials	10
2.2.1.1	Low-alloyed steel	10
2.2.1.2	Stainless steel.....	14
2.2.2	Common types of corrosion attack.....	15
2.2.2.1	Uniform corrosion.....	16
2.2.2.2	Pitting corrosion	17
2.2.2.3	Crevice corrosion	18
2.2.2.4	Stress corrosion cracking.....	19
2.2.3	Influencing factors.....	20
2.2.3.1	Temperature	20
2.2.3.2	Pressure	21
2.2.3.3	Fluid velocity	22
2.2.3.4	Acidity	22
2.2.3.5	Oxygen	23
2.2.3.6	Dissolved salts	24

Chapter 3	Experimental Setup	27
3.1	Investigated materials.....	27
3.1.1	Low-alloyed steel 1.7218	27
3.1.2	Stainless steel 1.4404	28
3.1.3	High-alloyed stainless steel 1.4562.....	28
3.2	Investigated geothermal brines.....	29
3.2.1	Sibayak geothermal site, wells SBY-03 and SBY-05.....	29
3.2.2	Lahendong geothermal site.....	30
3.2.2.1	Well LHD-05	30
3.2.2.2	Well LHD-23	30
3.3	Methods	30
3.3.1	Electrochemical techniques	30
3.3.1.1	Open circuit potential	31
3.3.1.2	Electrochemical impedance spectroscopy.....	31
3.3.1.3	Tafel extrapolation method.....	33
3.3.1.4	Cyclic polarization	34
3.3.2	Exposure Tests.....	35
3.3.3	Surface analysis	36
3.4	Test setup	36
3.4.1	Factors influencing corrosion	36
3.4.1.1	Temperature effect.....	37
3.4.1.2	Brine acidity	37
3.4.1.3	Brine concentration	37
3.4.2	Material sample preparation.....	38
Chapter 4	Corrosion Resistance of Low-alloyed Steel 1.7218	41
4.1	Introduction.....	41
4.2	Corrosion film growth.....	41
4.2.1	Short-term electrochemical methods.....	42
4.2.1.1	Open circuit potential monitoring.....	42
4.2.1.2	Electrode/solution interface characterization	42
4.2.2	Long-term exposure tests	44
4.3	Influence of temperature on corrosion performance.....	46
4.3.1	Short-term electrochemical methods.....	46

4.3.1.1	Open circuit potential monitoring	46
4.3.1.2	Electrode/solution interface characterization	46
4.3.1.3	Study of corrosion reaction kinetics and mechanisms	48
4.3.2	Long-term exposure tests	50
4.4	Influence of acidity on corrosion performance.....	53
4.4.1	Short-term electrochemical methods.....	53
4.4.1.1	Open circuit potential monitoring.....	53
4.4.1.2	Electrode/solution interface characterization	54
4.4.1.3	Study of corrosion reaction kinetics and mechanisms	56
4.4.2	Long-term exposure tests	57
4.5	Influence of salt concentration on corrosion performance	59
4.5.1	Short-term electrochemical methods.....	59
4.5.1.1	Open circuit potential monitoring.....	59
4.5.1.2	Electrode/solution interface characterization	60
4.5.1.3	Study of corrosion reaction kinetics and mechanisms	61
4.5.2	Long-term exposure tests	63
4.6	Investigation of crevice corrosion susceptibility.....	64
4.7	Investigation of stress corrosion cracking susceptibility	66
Chapter 5	Corrosion Resistance of Stainless Steel 1.4404	67
5.1	Introduction.....	67
5.2	Passive film growth.....	67
5.2.1	Short-term electrochemical methods.....	68
5.2.1.1	Open circuit potential monitoring.....	68
5.2.1.2	Electrode/solution interface characterization	68
5.2.1.3	Determination of critical potentials.....	70
5.2.2	Long-term exposure tests	71
5.3	Influence of temperature on corrosion performance.....	71
5.3.1	Short-term electrochemical methods.....	71
5.3.1.1	Open circuit potential monitoring.....	71
5.3.1.2	Electrode/solution interface characterization	72
5.3.1.3	Determination of critical potentials and pits characterization	73
5.3.2	Long-term exposure tests	76
5.4	Influence of acidity on corrosion performance.....	77

5.4.1	Short-term electrochemical methods.....	77
5.4.1.1	Open circuit potential monitoring.....	77
5.4.1.2	Electrode/solution interface characterization.....	78
5.4.1.3	Determination of critical potentials and pits characterization.....	80
5.4.2	Long-term exposure tests.....	83
5.5	Influence of salt concentration on corrosion performance.....	85
5.5.1	Short-term electrochemical methods.....	85
5.5.1.1	Open circuit potential monitoring.....	85
5.5.1.2	Electrode/solution interface characterization.....	85
5.5.1.3	Determination of critical potentials and pits characterization.....	87
5.6	Investigation of crevice corrosion susceptibility.....	90
5.7	Investigation of stress corrosion cracking susceptibility.....	92
Chapter 6	Corrosion Resistance of High-alloyed Stainless Steel 1.4562	95
6.1	Introduction.....	95
6.2	Passive film growth.....	95
6.2.1	Short-term electrochemical methods.....	96
6.2.1.1	Open circuit potential monitoring.....	96
6.2.1.2	Electrode/solution interface characterization.....	96
6.2.1.3	Determination of critical potentials.....	98
6.2.2	Long-term exposure tests.....	98
6.3	Influence of temperature on corrosion performance.....	99
6.3.1	Short-term electrochemical methods.....	99
6.3.1.1	Open circuit potential monitoring.....	99
6.3.1.2	Electrode/solution interface characterization.....	100
6.3.1.3	Determination of critical potentials and pits characterization.....	101
6.3.2	Long-term exposure tests.....	104
6.4	Influence of acidity on corrosion performance.....	105
6.4.1	Short-term electrochemical methods.....	105
6.4.1.1	Open circuit potential monitoring.....	105
6.4.1.2	Electrode/solution interface characterization.....	106
6.4.1.3	Determination of critical potentials and pits characterization.....	108
6.4.2	Long-term exposure tests.....	111
6.5	Influence of salt concentration on corrosion performance.....	112

6.5.1	Short-term electrochemical methods.....	112
6.5.1.1	Open circuit potential monitoring.....	112
6.5.1.2	Electrode/solution interface characterization	113
6.5.1.3	Determination of critical potentials and pits characterization	115
6.6	Investigation of crevice corrosion susceptibility.....	117
6.7	Investigation of stress corrosion cracking susceptibility	119
Chapter 7	Summary	121
Chapter 8	Conclusions & Outlook	127
Appendix A	Literature	A-01
Appendix B	List of Symbols	A-17
Appendix C	List of Figures	A-19
Appendix D	List of Tables	A-27
Appendix E	Publications	A-31
Appendix F	Acknowledgments	A-33
	Resume	

Chapter 1

Introduction

The growth in a global demand for energy, as well as the awareness of a significant climate change, have evolved a very strong incentive for utilizing and expanding the use of clean and renewable energy resources.¹⁻⁶ Geothermal energy is considered as one of a few alternatives ideal for replacing conventional sources due to its consistency and reliability, and is receiving ever more attention.^{2,7,8} However, geothermal systems are found to be the most aggressive natural environments in terms of corrosion. High temperature and pressure conditions, as well as the existence of almost an entire periodic system of elements in form of corrosive salts, present a major threat to the integrity of the construction material.⁹ Therefore, in order to achieve a safer and continuous energy production, and increase the competitiveness of geothermal energy on the world scene, a comprehensive assessment of the materials suitability is of high importance for operators and vendors. Finally, this would lead to an increased lifespan of the power plant, as well as its economic profit, due to the reduced maintenance costs.

Among the studied literature, a vast of them deals with the corrosion performance of different steel grades in geothermal environments.¹⁰⁻²⁰ However, none of them studied the combined influence of different physical and chemical factors, such as temperature, pressure, solution acidity and salt concentration, on the materials behavior. These factors determine the corrosion rate of metals in geothermal fluids. However, they are prone to periodic changes due to the instability of the geothermal systems,²¹⁻²⁵ and their influence needs to be elucidated thoroughly prior to the initial design phase to ensure a “safer operating window” of a power plant.²⁶⁻²⁸

Higher temperatures were found to increase the corrosion rate only when the metal dissolution was controlled by the chemical reaction and/or diffusion and migration of aggressive species toward the metal surface.²⁹⁻³¹ In case the corrosion was influenced by other factors, such as solubility of corrosive gases (O₂, H₂S, CO₂), formation of stable and compact corrosion product film on the steel surface, etc., the corrosion rate of steel in aqueous media decreases with temperature.^{30,32,33} Increased concentration of chloride ions leads to a higher amount of active sites susceptible to chloride adsorption and larger driving forces toward the bottom of the initiated pits, having as a consequence higher localized corrosion propagation rates.^{14,34,35} However, reduction in the corrosion rate has also been observed with an increased salt content due to the metal surface saturation and lower oxygen solubility.³⁶ It was revealed that the solution acidity has the most profound effect on the metal dissolution when pH decreases below 4.^{16,33,37,38} In such environments hydrogen reduction is a dominant cathodic reaction. An increase in its rate, due to the hydrogen ion abundance, results in an increased anodic (metal dissolution) reaction rate.³⁹ Furthermore, hydrogen may incorporate in the passive film formed on the metal surface,⁴⁰ thereby forming positively charged localized sites and promoting the adsorption of negative chloride ions on the metal surface.⁴¹⁻⁴³

The objective of this work, performed within the framework of the multidisciplinary project *Sustainability concepts for exploitation of geothermal reservoirs in Indonesia – Capacity building and methodologies for site deployment*, funded by the German government (Ministry of Education and Research, BMBF), was to evaluate which materials currently available on the market could overcome the problem of corrosion and withstand highly aggressive conditions in the exploitation of geothermal resources in volcanic environments, and what are the dominating environmental factors. The focus was set on the above-ground material application for construction of the first binary power plant in Indonesia. The main investigated materials were alloyed steels considering their excellent corrosion resistance, appropriate mechanical properties and lower costs compared to other materials.⁴⁴⁻⁴⁶

The research approach focused on three materials, selected out of different alloying steel grades based on their chemical composition, and their corrosion performance in electrolyte solutions that simulated the conditions present on the geothermal sites Sibayak (North Sumatra) and Lahendong (North Sulawesi) – the geothermal “hotpots” of Indonesia. The difference in the chemical composition of the brines, as well as the temperature and the pressure conditions in the system were used as border limits, i.e. factors, whose influence on the corrosion behavior of the selected alloys was investigated. The methodology comprised of a combined use of both electrochemical and exposure testing methods in the static conditions of the artificial brines that simulated the period of a power plant temporary

shutdown, for instance during the maintenance. Exposure tests provided a rational insight into materials behavior at open circuit conditions during long-term periods of immersion in the investigated conditions. On the other hand, the advantage of short-term electrochemical methods was the elucidation of corrosion reactions kinetics and mechanisms, and prediction of corrosion rates and the materials susceptibility to different types of corrosion. Furthermore, after each alloy/condition experimental set, the surface of the corroded materials was analyzed to characterize the type of corrosion attack and study the evolution and change of the formed surface layer.

The approach and methodology used in this research enabled a comprehensive evaluation and comparison of the selected alloys performance in specific geothermal environments. Nevertheless, the achieved results could be transferable also to other applications other than geothermal and allow a behavioral prediction of the metallic materials, grades and types other than the investigated ones. The research is certainly of the greatest value for operators and vendors of geothermal power plants. It would doubtless serve its purpose and help to maintain the sustainability and integrity of geothermal systems, and assure a continuous, reliable and safer energy production.

Chapter 2

State of the Art

2.1 Geothermal energy

Continuous growth on energy demand and constant increase in greenhouse gas emissions have raised the world's consciousness and awareness for the need of a renewable and clean type of energy.¹⁻⁶ As one of a few alternatives ideal for replacing supply-limited and environment-polluting fossil fuels, geothermal energy is considered the most consistent and reliable resource among all the renewables^{2,7,8} due to its multitude valuable characteristics.^{3,5,8,47-54}

2.1.1 Geothermal hotspots

Geothermal energy is the natural heat of the Earth stored inside the Earth's core, mantle and crust.^{5,47} For normal geological conditions an average geothermal temperature gradient (an increase in temperature with depth) is 25 - 30 °C/km depth reaching the maximum of 6,650 °C in the core of the Earth (Figure 2.1).^{3,55} There are, however, some areas in which the geothermal gradient is far beyond the average value, reaching the values up to 10 times higher than the average ones. These high enthalpy regions, often called the "hotspots", are located nearby tectonic plate boundaries and recent volcanism, and cover about 10 % of the Earth's surface.³ They represent the most common geographical places for geothermal fields, as the crust is highly fractured and thus, permeable to geothermal fluids, and sources of the heat are readily available.⁴⁷

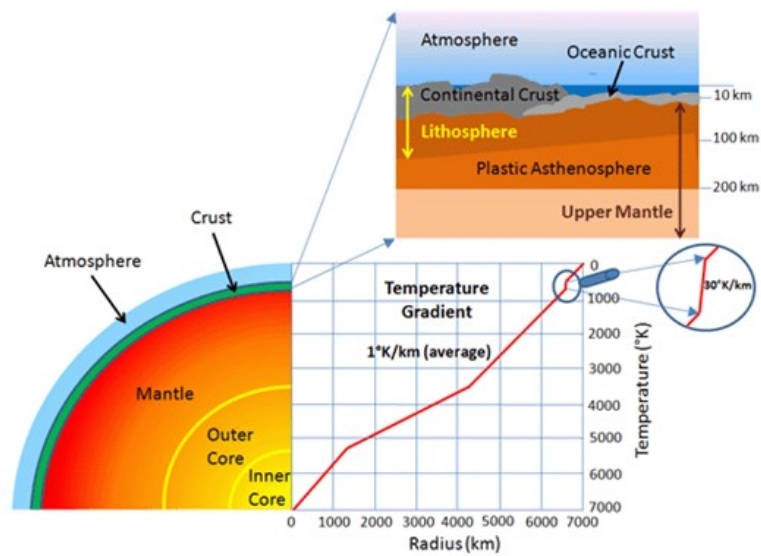


Figure 2.1 Structure of the Earth and the average geothermal gradient⁵⁶

2.1.2 Utilization - electricity generation

One of the ways to utilize the geothermal energy is for the electricity generation.^{47,57,58} In order to be cost effective, conventional electric power production is commonly limited to the fluid temperatures above 100 °C.⁵³ To reach the minimum requirements, wells within the earth are drilled up to several kilometers in depth to extract the heat in form of a geothermal fluid.⁵⁵ The fluid is piped from the production well through a turbine, which drives the generator and produces electrical energy. Upon that, the fluid is transmitted to a condenser and reinjected back into the reservoir through the injection well (Figure 2.2).^{47,48}

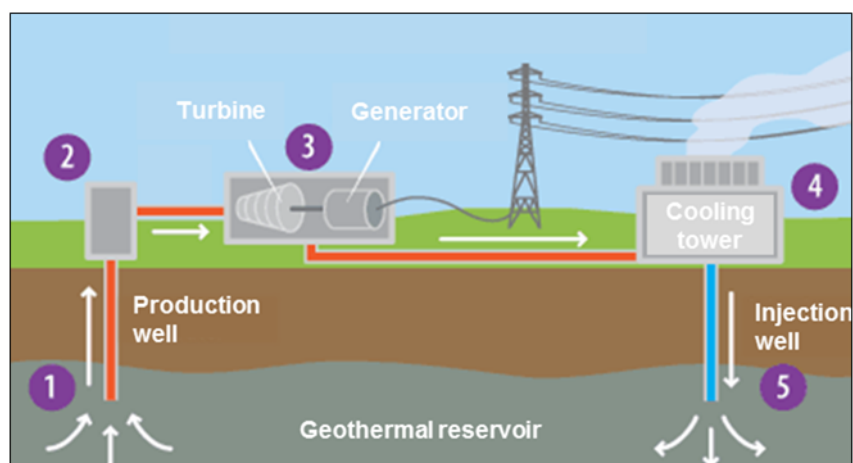


Figure 2.2 Geothermal system – geothermal fluid exploitation⁵⁹

2.1.3 Geothermal energy in Indonesia

Located in the Pacific “Ring of Fire” volcano belt, one of the top ten geothermal hotspots, Indonesia has the largest estimated geothermal energy reserves in the world of approximately 27,000 MW_e or 40 % of the global total.^{3,57,58,60-62} Based on the available reports from 2011,^{57,63} it utilizes less than 5 % of the estimated potential or 1,196 MW_e, being the 3rd largest producer of geothermal energy, behind USA and the Philippines. The major contributor to the country’s total energy production are fossil fuel-fired power plants with approximately 87 %⁶³ out of 174 Mtce (million tons of coal equivalent) putting Indonesia in the top 3 or 4 global contributors to greenhouse gas emissions.⁷ In order to minimize the environmental impact and meet the rapidly increasing demand of the electricity (from 1990 to 2007 annual increase by about 6 %; more the 3 times faster than the world’s average annual growth),⁷ Indonesia is devoting a lot of effort in accelerating the development of geothermal energy (from 2005 to 2010 the installed capacity increased 50 % and the electricity production 58 %).³ The main target is reaching 6,000 MW_e of energy production until 2020 and 9,500 MW_e by 2025.

With 256 geothermal potential locations in Indonesia, there are currently 7 operated geothermal fields in the country (Figure 2.3).^{58,60} The focus of the present study was set on two prospective areas, geothermal fields Sibayak (North Sumatra) and Lahendong (North Sulawesi), operated by Pertamina Geothermal Energy (PGE), one of the energy resource companies in Indonesia.

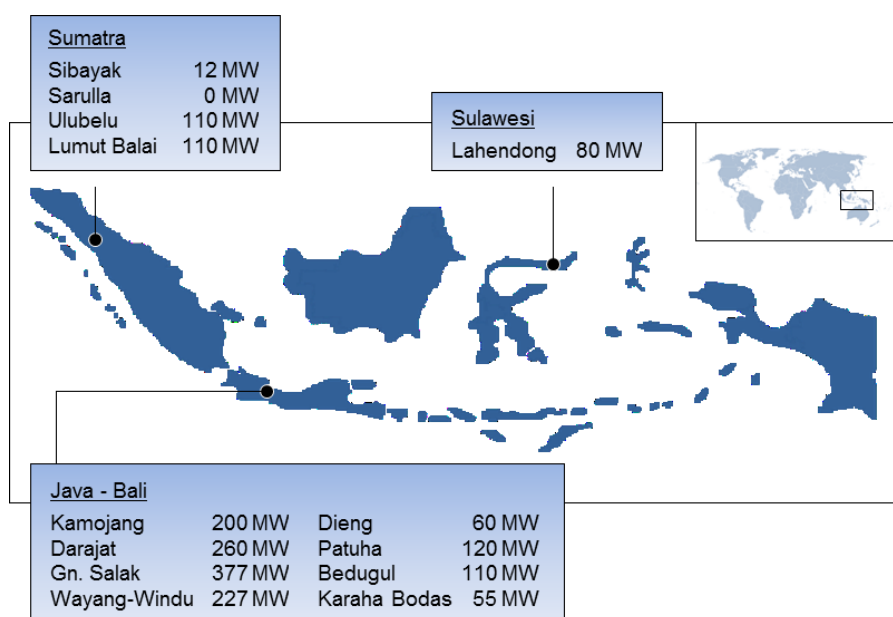


Figure 2.3 Operating geothermal fields in Indonesia⁶⁰

2.1.3.1 Sibayak

Located within the Singkut caldera rim 65 km SW of Medan in North Sumatra at an elevation between 1,400 m a.s.l. and 2,200 m a.s.l., and surrounded by 3 active volcanoes, Sibayak is one of the prospective geothermal fields in Indonesia. According to the internal reports from 2011, it consists of 3 clusters with all together 7 production and 3 reinjection wells.⁶⁴ The reservoir is liquid-dominated with temperature ranges between 240 °C and 300 °C and pressure variations between 45 bar and 110 bar. The enthalpy of the reservoir reaches 1100 kJ/kg.⁶⁵⁻⁶⁷ The fluids are discharged from the wells at approximately 170 °C and 8 bar. They are low acidic (pH 4.82 - 5.45) and contain relatively high chloride (1,115 mg/L) and silica (567 mg/L) content.^{21,65} Physicochemical properties of the brines produced from the wells SBY-03 and SBY-05 are shown in Table 2.1.^{21-24,62,65}

Currently, Sibayak geothermal field utilizes dry steam for production of 12 MW_e energy out of estimated 25 MW_e potential.⁶⁵

2.1.3.2 Lahendong

Lahendong geothermal field is located 30 km S of Manado in North Sulawesi, one of the major geothermal resources in Indonesia with an estimated potential of 865 MW_e.⁵⁸ Lying at an elevation between 600 m a.s.l. and 900 m a.s.l., it is characterized by active volcanoes that formed the volcanic inner arc of Minahasa.⁶⁸ Due to such a unique geological position, Lahendong area itself has the potential of 170 MW_e.⁵⁸ Currently, only 80 MW_e has been utilized (4 units x 20 MW_e), but still enough to supply 60 % of North Sulawesi with electrical energy.^{58,62,64,69}

The field consists of 28 wells drilled in 5 clusters.⁶⁴ Geothermal reservoirs in Lahendong field are two-phased high-temperature geothermal systems, divided into two categories based on their temperature and chemical characteristics.^{62,68,70} In the southern part the temperature of the reservoir reaches 350 °C, the fluids are steam-dominated (80 %) and contain relatively high silica (750 mg/L) and moderate chloride (440 mg/L) content when discharged from the wells. The temperatures in the northern part of the geothermal system do not exceed 250 °C, the fluids are liquid-dominated (80 %) and contain low silica (48 mg/L) and chloride (20 mg/L) concentration at the surface.^{21-24,68,70} The whole geothermal area is characterized as low acidic (pH 3.77 - 5.35) above the ground at 175 °C and 9 bar, with an exception of the fluid discharged from the well LHD-23 (northern part), having relatively low pH (2 - 3) and high chloride (1,500 mg/L) and sulphate (1,600 mg/L) content.²¹⁻²⁴ Physicochemical properties of the brines produced from the wells LHD-05 and LHD-23 are shown in Table 2.1.^{21-24,62,65}

Table 2.1 Characteristics of the brines produced from the wells SBY (SBY-03 and SBY-05), LHD-05 and LHD-23 on the geothermal fields Sibayak and Lahendong^{21-24,62,65}

	SBY	LHD-05	LHD-23
Physicochemical parameters			
T [°C]	22 - 23	26 - 28	27
pH	5.4 - 5.5	3.8 - 4.6	1.1
E° [mV]	-210 - -187	-157 - 289	36
EC [μ S/cm]	4820 - 4920	220 - 580	9700
Brine composition [mg/L]			
F ⁻	2.6 - 4.4	0.05 - 0.15	1.9 - 2.0
Cl ⁻	1144 - 1611	4 - 21	475 - 1559
Br ⁻	7.5 - 10.6	0.06 - 0.06	0
HCO ₃ ⁻	0	0 - 11.6	0.00 - 0.90
NO ₃ ⁻	0 - 0.06	0.10 - 0.10	0
SO ₄ ²⁻	9.9 - 12.8	6.9 - 27.4	537 - 1609
PO ₄ ³⁻	0	0.0 - 1.3	0
B ³⁺	0	0	23.0 - 23.0
Ca ²⁺	194 - 210	1.0 - 4.1	0 - 3.2
Fe ²⁺	< 0.1	0.1 - 4.5	5.4 - 9.4
K ⁺	238 - 248	< 10 - 0	79 - 173
Mg ²⁺	0.9 - 2	0.00 - 0.69	1.8 - 5.0
Mn ²⁺	2.6 - 2.7	< 0.1 - 0	6.4
Na ⁺	560 - 590	20	579 - 1637
Li ⁺	0	0	2.8
Sr ²⁺	1.6 - 1.8	< 0.01	0.04
Zn ²⁺	< 0.1	0.92	0.80
Si ⁴⁺	302 - 306	9.6 - 20.0	461 - 962

2.2 Corrosion on geothermal power plants

During an average lifespan of approximately 30 years,⁷¹ geothermal power plants are more than 90 % of the time in operation, i.e. they are producing electrical energy. One of the major problems that could affect the stable and continuous energy production is the corrosion of construction materials and equipment due to their interaction with an aggressive environment.^{9,72} Among all the existing electric power generation facilities, corrosion is considered to be the most severe on geothermal power plants.¹⁶ This can be attributed to the extreme high temperature and pressure conditions present in geothermal systems, as well as the existence of almost an entire periodic system of elements in form of corrosive salts.⁹

Therefore, geothermal fluids are found to be extremely hostile for the construction material and equipment installed at geothermal power plants. If insufficient and inadequate measures for material selection are undertaken during the initial design phase of the plant, a huge risk of equipment degradation and system failure is present. This could not only lead to the reduction in the energy production, but also to the shutdown of the entire geothermal power plant.³⁸

The corrosion on geothermal power plants depends on the physicochemical conditions prevailing on the site. Given that each geothermal system is different and unique; depending on the geographical location, reservoir depth, geology of the rocks beneath the surface etc.,⁷³ for a reliable and reasonable material selection it is necessary to evaluate the corrosion behavior of materials for the specific geothermal field, the field where the power plant will be installed. That way appropriate materials would be chosen that would in the same time withstand such aggressive environments and still be cost-effective. Eventually, safer operation of geothermal power plant, as well as its longer lifetime would be accomplished.

2.2.1 Construction materials

Geothermal systems consist of various constructional units required for the power plant operation. In order to exploit the geothermal fluid from the reservoir and transfer it to the turbine in the geothermal power plant, several hundred meters of transport pipeline is installed, along with different equipment necessary for plants' performance. The most commonly used materials for construction of these units are metallic materials, primarily steels, due to their excellent corrosion resistance in aggressive geothermal environments, appropriate mechanical properties and lower costs compared to other materials.¹⁶⁻¹⁸ Since this study focused only on alloyed steel materials, in the further text only their characteristics are being further discussed.

2.2.1.1 Low-alloyed steel

Low-alloyed steels are ferrous materials exhibiting higher corrosion resistance and superior mechanical properties to plain carbon steels as a result of addition of alloying elements such as nickel, chromium and molybdenum etc.⁷⁴ Depending on the chemical composition they can be classified as nickel, nickel-chromium, molybdenum or chromium-molybdenum steels. Total element addition could range from 2 wt% up to 10 wt%.

Exposing low-alloyed steel to an aqueous solution, iron tends to dissolve uniformly, forming different corrosion products, depending on the steel composition and the surrounding medium. In the initial phase of exposure, the layer of the corrosion products, formed on the surface of low-alloyed steel, is extremely porous causing the corrosion rate to be substantially high. As a function of time and the type of surrounding environment, these compounds may become more or less compact. The more compact they are, the more the corrosion rate is reduced.^{39,75,76}

Corrosion in neutral solutions

Exposing low-alloyed steel to an aqueous solution containing oxygen, iron tends to dissolve uniformly according to the reaction:



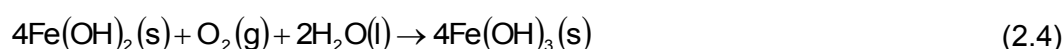
The most common cathodic reaction in neutral solutions, which consumes the liberated electrons, is the reduction of dissolved oxygen:



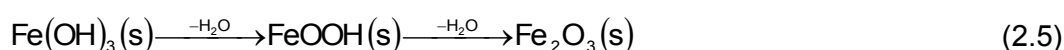
Ferrous ion, Fe^{2+} , formed during the anodic oxidation of iron, reacts with the hydroxyl anion, OH^{-} :



forming a ferrous (II) hydroxide, $\text{Fe}(\text{OH})_2$, also known as the “green rust”. Due to the instability of $\text{Fe}(\text{OH})_2$, it is readily oxidized to insoluble ferric (III) hydroxide, $\text{Fe}(\text{OH})_3$, even in the presence of only traces of oxygen:



$\text{Fe}(\text{OH})_3$ is an amorphous brown-red compound, thermodynamically unstable. It easily transforms to ferric (III) oxide, Fe_2O_3 , with the formation of dehydrated ferric oxy-hydroxides as intermediate products:⁷⁷

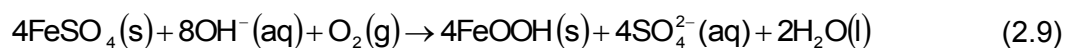
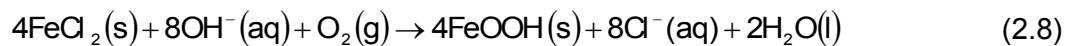


When there is no dissolved oxygen in the water or its supply is limited (difficulties in oxygen diffusion, oxygen depletion, deaerated conditions, etc.), iron, Fe^{2+} and Fe^{3+} , and hydronium ions, H_3O^+ , can act as oxidizing agents and continue corrosion reactions on the surface of low-alloyed steel. Since their concentration in neutral and alkaline aqueous solutions is usually very small, their influence on the cathodic reaction is not significant, causing the corrosion rate to slow down.⁷⁷

Among numerous iron oxides possible to form on the surface of low-alloyed steel, (Table 2.2), the most common are $\gamma\text{-FeOOH}$ (lepidocrocite), $\alpha\text{-FeOOH}$ (goethite), Fe_3O_4 (magnetite) and $\gamma\text{-Fe}_2\text{O}_3$ (maghemite).⁷⁸ These products can coexist partly as crystalline and partly as amorphous structures, the ratio depending on the environmental conditions. The layer can incorporate as well various impurities, such as chlorides, sulphates, carbonates, calcium, magnesium, etc., present in the medium.⁷⁷ Anions, such as chlorides and sulphates, can accelerate corrosion by promoting anodic dissolution:



Due to the instability of the formed corrosion products, they are readily oxidized to FeOOH in the presence of oxygen or other oxidizing agent:



releasing $\text{Cl}^{\text{-}}$ and $\text{SO}_4^{2\text{-}}$ anions and restarting another cycle.⁷⁹

Corrosion in acidic solutions

Exposing low-alloyed steel to a solution containing high concentration of protons, indicated by the low pH, the most common cathodic reaction is hydrogen evolution:



The anodic reaction that precedes the hydrogen reduction is the oxidation of iron, Fe , to ferrous ion, Fe^{2+} , as shown in reaction (2.1), which occurs on the ferrite phase of the low-alloyed steel. Due to the more noble potential (+0.37 V_{SHE} in acid), carbide phase serves as a cathode indicating how the rate of low-alloyed steel corrosion depends strongly on the steel

chemical composition, especially the carbon content; the higher the carbon content, the larger the cathodic area leading to the rapid consumption of electrons and thus, the greater the increase of the anodic reaction rate.^{77,80}

Table 2.2 The list of known iron oxides⁷⁸

Oxy-hydroxides and hydroxides	Oxides
Goethite, α -FeOOH	Hematite, α -Fe ₂ O ₃
Lepidocrocite, γ -FeOOH	Magnetite, Fe ₃ O ₄ (Fe ^{II} Fe ^{III} ₂ O ₄)
Akaganéite, β -FeOOH	Maghemite, γ -Fe ₂ O ₃
Schwertmannite, Fe ₁₆ O ₁₆ (OH) _y (SO ₄) _z · nH ₂ O	β -Fe ₂ O ₃
δ -FeOOH	ϵ -Fe ₂ O ₃
Feroxyhyte, δ' -FeOOH	Wüstite, FeO
High pressure FeOOH	
Ferrihydrite, Fe ₅ HO ₈ ·4H ₂ O	
Bernalite, Fe(OH) ₃	
Fe(OH) ₂	
Green Rusts, Fe ^{II} _x Fe ^{III} _y (OH) _{3x+2y-z} (A ⁻) _z ; A ⁻ = Cl ⁻ ; 1/2 SO ₄ ²⁻	

In deaerated conditions, the total reaction of the iron dissolution in hydrochloric acid could be presented as:



In case when low-alloyed steel is exposed to acid containing dissolved oxygen, oxygen reduction also occurs on the cathode areas of the steel, next to the hydrogen evolution:⁷⁷



leading to the same reaction path as in the reactions (2.3) - (2.5).

As noticed, the formation of different phases on low-alloyed steel surface during its exposure in corrosive environment depends on many factors; the chemical composition of the steel, environment composition and conditions, exposure time etc. In the initial phase of the exposure, the layer of corrosion products is usually extremely porous, causing substantially high corrosion rates. As a function of time and the type of surrounding environment, these compounds may become more or less compact. The more compact they are, the more decreased is the corrosion rate.³⁹⁻⁷⁶

2.2.1.2 Stainless steel

Stainless steel is an alloy containing minimum 12 wt% chromium.^{46,35,77,81} When exposed to certain environments containing oxygen, a stable, passive film is readily formed on its surface, consisting mostly of chromium (III) oxides, hydroxides and/or oxy-hydroxides.^{82,83}



The film is impervious to water and air, and provides excellent protection against uniform corrosion, preventing further surface corrosion and retarding it from spreading into the alloy's internal structure. It forms instantly on the steel surface and grows slowly with time. Depending on the surrounding environment and conditions, it normally results in an extremely thin film (several orders of nm thick) invisible to the naked eye, making the metal surface remain lustrous. In contrast to the corrosion products formed on low-alloyed steel surface, the properties of the passive layer formed on stainless steel do not significantly change after the first 24 h, unless exposed to a new environment.⁸² In case the surface is scratched, the film has the possibility to quickly reform, thereby repassivating the stainless steel surface.^{16,77,81,84}

The characteristics of the passive film are strongly dependent on the metal composition, surrounding environment and exposed conditions. In the acidic environments it was found that it is enriched with chromium (III) oxides and hydroxides, due to the sufficient chromium content.⁸² The reason why the presence of iron, the most abundant element in the alloy, has not been detected in the passive layer, is mainly due to its selective dissolution in acidic media. However, in alkaline media the passive layer contains more iron oxides and hydroxides thanks to their superior stability compared to chromium compounds.^{82,85}

Beside chromium, stainless steels are alloyed with other elements as well (nickel, molybdenum, nitrogen, copper, etc.), in order to increase their resistance to localized corrosion and improve their mechanical properties.^{44,46,16,77,81,39,86-88} These elements can also be incorporated in the protective layer formed on the surface of the stainless steel.^{82,89} Nickel is, therefore, found mostly in the layer closest to the metal/oxide interface, in its metallic state, since it oxidizes less readily than iron and chromium. Similarly, molybdenum in its oxidizing state 6+ is found to be enriched at the surface region. However, Mo⁴⁺ oxides and oxy-hydroxides show more homogenous distribution through the passive layer.^{16,73,75} Knowing the content of the specific alloying elements, it is possible to calculate and roughly estimate the tendency of the alloy to pitting corrosion using the following equation for pitting resistance equivalent number, PREN:³⁵

$$\text{PREN} = w\% \text{Cr} + 3.3 w\% \text{Mo} + 20 w\% \text{N} \quad (2.14)$$

Stainless steel grades with a PREN of 40 or more are known as “superaustenitic” or “superduplex” types, depending on which type of structure they have.⁴⁶ The most common stainless steels according to the type of structure are austenitic, ferritic, martensitic and duplex stainless steels. Besides the difference in the crystal lattice and mechanical properties, these phases discern in the corrosion resistance. Since austenitic stainless steels are the primary steels being used in the present study, their corrosion resistance will be briefly discussed in the following text.

Austenitic stainless steels are a class of alloys with a face-centered-cubic crystal structure of austenite over the whole temperature range from the cryogenic region to the melting point of the alloy. With more than 70 % of the total stainless steel production, austenitic grades are the most common steels used when both the properties of steel and resistance to corrosion are required.⁹⁰ The reason for such a common use is mainly because, next to the duplex steels, they are found to be the most corrosion resistant among the stainless steel grades due to the high chromium and nickel content.⁴⁶ They contain minimum 16 wt% chromium; providing them excellent resistance to uniform corrosion, maximum 0.15 wt% carbon; reducing the possibility to intergranular corrosion, and sufficient nickel and molybdenum; to retain an austenitic structure and to reduce the susceptibility to localized corrosion.^{39,35,84} Despite such low carbon content, the tendency to carbide precipitation in the structure of austenitic grades still exists. Therefore, grades with very low carbon content have been designed in order to reduce the sensitization effect and, that way, the susceptibility to intergranular corrosion. These grades are usually called the “L” grades; “L” indicating the low carbon content, < 0.03 %. One of the austenitic grades, exhibiting even better corrosion resistance than normal austenitic steels, is superaustenitic steel. Such steels have greater resistance to pitting and crevice corrosion ensured by the higher molybdenum and nitrogen content, what is evident in the high PREN (PREN > 40). In addition, the nickel content is higher as well, compared with the normal austenitic grades, making them less susceptible to stress corrosion cracking.^{39,35,84}

2.2.2 Common types of corrosion attack

Depending on the type of alloy and the operating conditions, there are many different types of corrosion possible to occur on the construction material. The most common forms observed on steels in geothermal systems containing high salinity brines are uniform corrosion, and localized corrosion in form of pitting corrosion, crevice corrosion and stress corrosion cracking.^{26,27,28} In the further text these forms of corrosion are discussed in detail.

2.2.2.1 Uniform corrosion

Uniform corrosion is a type of corrosion attack uniformly distributed over the entire metal surface area.^{39,77} It is the most common form of corrosion having rates that can vary over wide ranges, depending on the environmental factors affecting it. Due to its predictive nature, uniform corrosion rarely causes disastrous failures in modern engineering systems.^{91,92}

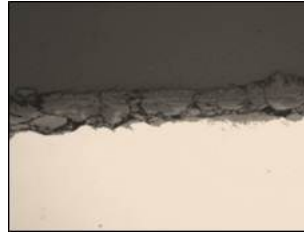


Figure 2.4 Uniform corrosion

On the surface exhibiting uniform corrosion, anodic and cathodic sites are constantly switching positions, because the conditions both on the steel surface and in the solution are changing with time. This leads to the uniform loss of the alloy surface and homogeneous distribution of corrosion products formed on it.⁷⁷ If the products of anodic reaction, e.g. ferrous ions, Fe^{2+} , dissolve in the surrounding medium, the rate of the metal loss may become quite high, due to the formed concentration cell between the solution and the steel/solution interface. On the other hand, depending on various factors, one of them being chemical composition of the exposed metal, an insoluble and compact layer of corrosion products is possible to form on the metal, presenting a physical barrier between the surface and the corrosive environment, and protecting the metal from the rapid corrosion. The formation of such kind of protective layer is usually a characteristic of higher alloyed steels ($\text{Cr} > 12 \text{ wt}\%$) and it is known as 'passivity',^{16,77,78} as already been addressed in the previous text. However, it has been observed that stainless steels can also suffer from uniform corrosion in specific environments, such as strongly acidic or alkaline solutions.⁹³ Low-alloyed steel, on contrary, corrodes uniformly forming loosely bound and porous corrosion products on the surface. In particular conditions, these layers can become adherent and non-porous, thereby providing protection to the metal by reducing the corrosion rate.^{11,17,77}

The nature and properties of the protective films formed on the steel surface are very important from the corrosion resistance viewpoint. When strength, dense and adherent film on a metal surface breaks down locally, it may give rise to highly localized regions of corrosion attack such as pitting.^{39,77,35}

2.2.2.2 Pitting corrosion

Pitting corrosion is characterized as a highly localized corrosion attack that occurs in the form of pits, which occupy a very small surface area, but which can be quite deep. The overall metal loss is usually minimal and difficult to detect, making this form of corrosion extremely dangerous due to its unpredictable nature. It occurs only on specific sites of a metal surface due to the surface inhomogeneity, caused by physical or chemical defects, such as mechanical damage, imperfection of surface passive films, presence of flaws, impurities and inclusions on the metal surface, etc.^{77,35,84}



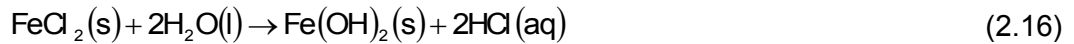
Figure 2.5 Pitting corrosion

The most common requirements for pitting corrosion to occur are the presence of a heterogeneous passive film on the metal surface and aggressive anionic species in the surrounding environment. Even though a passive layer does not commonly form on low-alloy steel surface, susceptibility of low-alloyed steel to pitting corrosion may occur, since some parts of the active surface tend to dissolve faster than the others.¹³

The most detrimental anionic species are found to be the chlorides, especially in the presence of oxidizing agents. Due to their small size and high diffusivity, they penetrate easily through the passive film and reach the bare metal surface. The mass transport of larger compounds, such as oxygen and other oxidizing agents, is limited through the same path, causing their depletion inside the pit and a formation of differential aeration cell. As a result cathodic reaction is shifted on a boldly exposed metal surface where these reactants are more plentiful. The anodic reaction, on contrary, occurs within the pit and causes the agglomeration of cations, due to the larger cathodic area that acts as a driving electric force of corrosion and stimulates the anodic dissolution within the pit. In order to maintain the electrical neutrality, chlorides electromigrate inside the pit and react with metallic cations forming soluble, non-protective corrosion products within the pit:



The products easily hydrolyze, lowering the pH of the pit solution due to the formation of hydrochloric acid:



That way, a critical acidic environment is generated, presenting a much aggressive medium for most of the metals that tends to propagate the pit growth.^{39,35,84}

2.2.2.3 Crevice corrosion

Crevice corrosion is a form of localized attack, usually associated with a stagnant solution present inside the shielded areas, i.e. crevices.³⁵ Such microenvironments are usually formed under gaskets, washers, insulation materials, lap joints, clamps, etc. They can occur between two metals or a metal/non-metal connection, the latter being more critical.²⁶ Mechanisms of crevice corrosion and pitting propagation are very similar due to the difficulties in oxygen transport inside the occluded site (crevice), which causes an oxygen depletion and, eventually, the formation of a large cathodic area outside the crevice. As a consequence, metal dissolution, i.e. the anodic reaction, within the crevice rapidly increases, causing a buildup of corrosion products. Eventually, the latter hydrolyze and form extremely acidic crevice solutions (pH could be as low as 1)⁷⁷ that cause the propagation of a crevice corrosion. The composition of a solution within the crevice depends only on the composition of the metal and not on the composition of the bulk solution. The bulk electrolyte has an influence only on the rate at which the composition of the crevice solution changes with time.^{39,35}

The main difference between crevice and pitting corrosion is the fact that, in order for crevice corrosion to occur, the existence of previously formed passive film on the metal surface is not required, as well as the presence of aggressive anionic species. Furthermore, crevice corrosion is more detrimental than pitting. It initiates more rapidly, due to the critical acidity that is reached much faster, causing critical (pitting) potential reduction and earlier onset of localized corrosion.^{39,35}

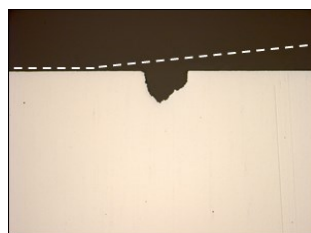


Figure 2.6 Crevice corrosion

2.2.2.4 Stress corrosion cracking

Stress corrosion cracking (SCC), also known as environmental induced cracking, is a form of localized corrosion induced from a combined influence of a tensile stress and a corrosive environment. The required tensile stress may be in a form of residual or applied (operational) stresses, the latter being more common reason for SCC failures in service. The effect of the applied stress is found to be mainly as the crack “opener”, thereby allowing easier diffusion of corrosive species inside the crack and causing higher metal dissolution rates.⁹⁴ Most likely locations for cracking to occur are regions of high residual stresses (welded, bolted and riveted joints) and regions where stress or environment concentration can occur (notches and crevices).



Figure 2.7 Stress corrosion cracking

Stress corrosion cracking can occur on numerous alloys. The main requirement for SCC is the presence of surface discontinuities or pits, which act as the crack initiation sites. For highly corrosion resistant metals, in addition, the presence of aggressive ions is necessary for the cracks to propagate. Usually, most of the metal surface is not attacked, while cracks appear and initiate through it along a path of higher than normal corrosion susceptibility. It is generally observed that the cracks progress rapidly perpendicular to the applied stress, along the grain boundaries (intergranular SCC) or without the preference for boundaries (transgranular SCC). The second path is more likely to occur,³⁹ though the first case is not unusual as well. It is considered that, in case of intergranular SCC precipitation of chromium carbides along the grain boundaries occurs, causing an impoverishment in chromium of the adjacent sites and making the structure more susceptible to corrosion attack. Thereby, SCC is more likely to occur on sensitized austenitic stainless steels with high yield strengths (> 1200 MPa), although it was observed on lower strength stainless steels, as well as on low-alloyed steels.^{15,95,96}

Beside the tensile stress, an adequate corrosive environment (chlorides, pH, T, etc.) and an alloy composition and structure, SCC is influenced by an electrochemical factor;

only within the certain potential ranges for particular metal/environment conditions cracking can occur.^{77,97}

By all means, the synergism of the aforementioned factors can reach catastrophic proportions, leading to devastating and unexpected failure of the material integrity due to the formation of a one single crack.

2.2.3 Influencing factors

From corrosion viewpoint the performance of construction materials in geothermal systems depends on numerous factors, divided into internal and external. Internal factors generally relate to the metallurgical properties of the materials: chemical composition, structure, treatment methods, imperfections present on the surface, flaws in the crystal lattice, presence of stresses, etc., which can be influenced only during the initial phase of material development. All other factors are considered as external, such as environment (chemical composition of the fluid, presence of dissolved salts and suspended solids, etc.) and operational conditions (temperature, pressure, flow rate, presence of other materials, presence of stray electrical currents, etc.).⁷⁷ In the further text the focus is put on the external factors, which have been addressed in this research.

2.2.3.1 Temperature

Temperature has a great influence on both thermodynamics and kinetics of metallic corrosion. Increase of temperature usually accelerates anodic and cathodic reactions on the metal surface, according to the Arrhenius equation,⁹⁸ and migration (diffusion, adsorption, absorption, etc.) of the species (e.g. oxidizers toward the cathode O_2 , H_3O^+ , Fe^{3+} , etc.).^{77,99} It also changes the dissolution and transformation of corrosion products on a metal surface.⁷⁷ However, increase in temperature causes a reduction in solubility of oxidizing gases present in the solution (O_2 , H_2S , CO_2 , etc.), resulting in solution degassing and its decreased corrosiveness.^{33,39,77} It was found that at 100 °C and 1 bar pressure nearly all dissolved oxygen escapes from the water. Thus, temperature influences corrosion rate by two factors; it accelerates both anodic dissolution of a metallic surface and cathodic reduction of oxidizing species, and diminishes the concentration of oxygen responsible for cathodic reaction.^{77,100} At some temperatures these two factors are equal, they compensate each other and corrosion rate reaches the maximum value. With further temperature increase, oxygen diminishes from the solution thereby, causing depletion in reactants needed for cathodic reaction, resulting in corrosion rate reduction (Figure 2.8). Increasing the temperature of the closed system further above 100 °C its pressure increases, causing a

higher solubility of the gases and further increase in the solution aggressiveness. However, a dielectric constant of the water decreases with the temperature increase resulting in a lower dissociation constant of the salts and acids present in the solution.^{101,102} Consequently, the solution conductivity is reduced, causing a lower solution oxidizing nature.

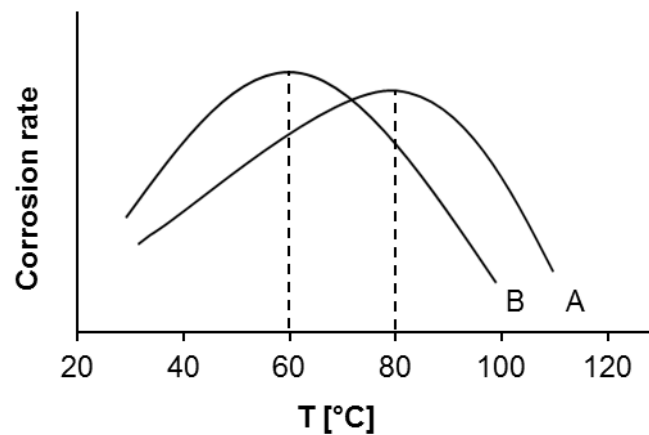


Figure 2.8 Temperature influence on corrosion of low-alloyed steel in pure water (A) and neutral aqueous solutions of electrolyte (B)⁷⁷

Except on uniform corrosion, temperature has an influence on pitting corrosion as well, namely the pitting potential. It was found that many materials do not suffer pitting at temperatures below a certain value; the critical pitting temperature (CPT). At low temperatures, they exhibit extremely noble pitting potential, corresponding to the transpassive dissolution. At higher temperatures, pitting potential decreases with the temperature increase and chloride concentration.^{35,84} In case of stainless steels a reduction of pitting potential of approximately 0.5 V has been observed in the temperature range between 0 °C and 70 °C. Usually, for many stainless steels CPT is in the range of 10 °C and 100 °C; the higher the CPT, the more resistant the alloy to pitting corrosion.³⁹

The susceptibility of metals and alloys to stress corrosion cracking is generally inversely proportional to the temperature increase. It was found that the severity of SCC is highest at normal atmospheric temperatures and decreases as temperature increases due to the surface relaxation.^{37,97}

2.2.3.2 Pressure

Geothermal fluids can be pressurized to several hundred bars within the geothermal system.^{10,103,104} Such high pressures can affect corrosion by increasing the solubility of oxygen and other corrosive gases.³⁷ Furthermore, the dielectric constants of aqueous solutions increases as well, resulting in higher dissociation constants of salts and

acids present in the solutions.^{101,105} That way more aggressive anionic species are present in the system, resulting in higher uniform and localized corrosion rates.

2.2.3.3 Fluid velocity

Fluid velocity is generally found to increase the corrosion rate.^{13,14,39,77,80,103,106-108} Compared to static conditions, during the fluid flow a constant supply of the aggressive corrosive species inside the system is enabled, causing their continual replenishment and thereby, higher corrosion rates.¹⁴ Furthermore, mass transport, for example of soluble iron from the oxide surface into the bulk solution or oxidizing species toward the metal surface, is greatly enhanced.^{107,108} Thus, the destruction of a protective passive layer formed on the metal is very likely to occur under high fluid velocities. However, there had been particular cases when certain fluid velocity decreased the corrosion rate.^{33,107} This is attributed to the fact that with higher turbulent flows, aggressive anionic species, such as chlorides, do not have time to adsorb on the metal surface, so they are easily removed from the latter, resulting in reduced localized corrosion rates.

Clearly, the influence of the solution velocity on the materials performance depends on the type of material being exposed. Low-alloyed steel is negatively affected by the dynamic conditions in the system, unlike the stainless steels, which show better performance in terms of corrosion.

2.2.3.4 Acidity

Influence of pH, a scale measuring hydrogen ion concentration in solution, plays a very important role in corrosion process.³⁷ In acidic environments due to the abundance of hydrogen ion, the reduction of hydrogen is a dominant cathodic reaction. The higher the hydrogen concentration (the more the acidic the solution), the higher the dissolution rate of the metal surface.^{38,39,77} When a metal is exposed to the acidic environments, it commonly corrodes uniformly, unless preferential, more active anodic sites are present on the metal surface, as well as aggressive anionic species. Investigating an effect of pH on the pitting corrosion, it was revealed that the pitting potential does not change significantly in the range of pH between approximately 1.6 and 10.^{45,35} This is related to the hydrolysis reaction of corrosion products, occurring inside the pits, that generates its own critical acidity, which is little influenced by the acidity of the bulk solution. However, in alkaline solutions pitting potential is displaced in nobler direction, due to the formation of stable, compact hydroxide corrosion products on the metal surface.

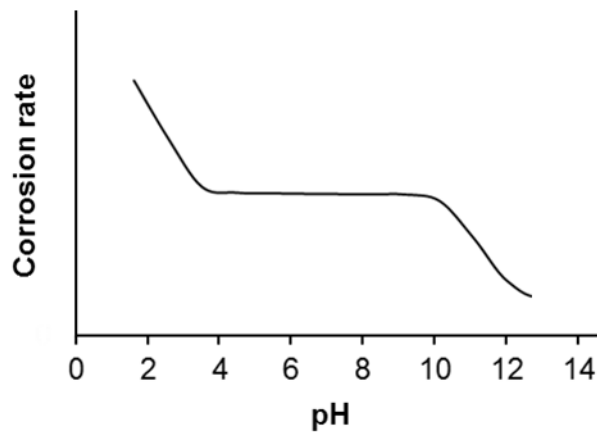


Figure 2.9 Influence of solution acidity on corrosion of steel⁷⁷

Iron and chromium, the most relevant components of alloyed steel materials, are found to corrode with relatively high rates in the solutions with pH below 4 and above 13.5 at temperatures higher than 80 °C. With pH increase to values between approximately 6 and 8 corrosion rate is significantly reduced, almost pH independent, due to the formation of stable chromium and iron compounds on the steel surface,³⁸ while at pH between 9 and 13 it is considered to be near zero considering the stability of iron hydroxides (Figure 2.9).⁷⁷

2.2.3.5 Oxygen

Geothermal systems are usually characterized as reducing environments, with redox potentials mostly below the hydrogen evolution line in Pourbaix diagram. Although it is not common for oxygen to occur in these systems, its intrusion has been noted on operating geothermal fields, mostly due to the contact of geothermal fluid with an atmosphere or with surface and shallow ground waters containing oxygen.^{12,13,15,109-111} An air infiltration at the pump seals, located in the system above the ground is likely to occur as well, particularly during the maintenance of the geothermal power plant, even though the fluid system is maintained mostly at overpressure.^{72,106}

The reason why presence of oxygen in geothermal systems is found to have an important role in corrosion is because, as soon as it enters the system, it quickly oxidizes the reduced species, promoting the corrosion of a metal surface.^{15-17,20,26,33,100,110} There have been cases noticed when a 30 µg/L concentration of oxygen caused a 4-fold increase of corrosion rate on carbon and low-alloyed steel in comparison to the deaerated conditions.¹⁰⁶ An increase of oxygen concentration will cause acceleration in corrosion process due to its participation in cathodic reaction, thereby promoting electrical current flow rate, i.e. metal dissolution.

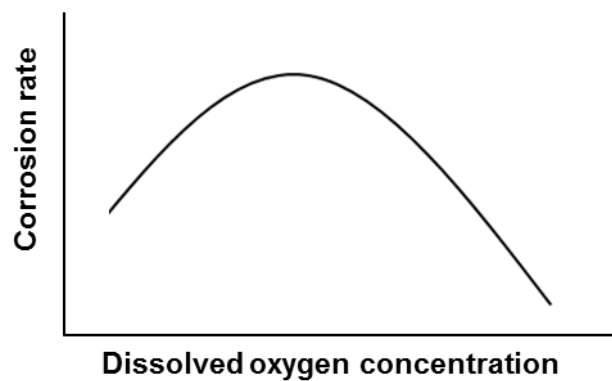


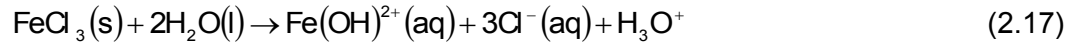
Figure 2.10 Influence of dissolved oxygen concentration in water of high purity on corrosion rate of low-alloyed steel⁷⁷

If present in sufficient concentrations, oxygen has a great effect on uniform corrosion, unless some preferential anodic sites exist on the metal surface, which act as sites for localized corrosion attack. It also has an indirect influence on the solution acidity; forming unstable and soluble corrosion products on the metal surface, products tend to hydrolyze, decreasing the pH of a solution and causing an even more profound effect on the exposed material.²⁶ However, it was found that oxygen presence in sufficient concentration in the system in some particular conditions may result also in the formation of stable oxide corrosion products that form a stable, compact passive film and provide protection to the metal against further corrosion.^{39,100} In some power stations it is sometimes injected even on purpose as one of the corrosion control methods.⁷⁷ Beside uniform corrosion, it was found that oxygen concentration below 100 µg/L is responsible for serious pitting corrosion and can cause chloride-stress corrosion cracking of some austenitic stainless steels when present in conjunction with chlorides and high temperatures.¹⁰⁶

2.2.3.6 Dissolved salts

Geothermal brines are being exploited from geothermal reservoirs, which can be found sometimes several km beneath the earth's surface. Due to the extreme conditions of temperatures and pressures present at such depths, the surrounding rocks tend to be dissolved by the hot brines, making them abundant in salts and thus, highly concentrated. The salts tend to dissociate into ions causing an increase in the brine electrical conductivity. The higher the conductivity, the higher the ability of the brine to carry an electric current on a metal surface between anodic and cathodic sites resulting in higher corrosion rates.⁷⁷ However, not all the dissolved salts have the same effect on the corrosion process. The most aggressive salts are acidic salts, e.g. ferric chloride, FeCl_3 , aluminum sulphate, $\text{Al}_2(\text{SO}_4)_3$,

sodium dihydrophosphate, NaH_2PO_4 , etc. Upon dissolution in the geothermal brine, they tend to hydrolyze to form acids, which decrease the solution pH:



As a consequence, corrosion rate of the metals exposed to such brines increases due to the higher cathodic reaction rates caused by an increase of hydrogen ion concentration.

In geothermal systems the most common anionic groups found in the brines are chlorides and sulphur compounds, originating from magma and/or hot rocks present inside the earth.^{112,113} These ions do not have an effect on overall corrosion rate since they do not participate in cathodic reactions. However, their influence on the localized corrosion rate is significant, especially that of chlorides due to their smaller size and higher diffusion coefficient, already addressed in the previous paragraph.^{35,84} Generally, as the concentration of these ions increases, the conductivity of the brine increases as well, resulting in a higher localized corrosion rate.^{14,39}

Other than acidic salts, salts that form deposits are a very common feature in geothermal brines. They are mainly silicate and carbonate minerals, precipitating on the metal surface due to the pressure and temperature drops occurring inside the geothermal systems (e.g. after heat-exchangers, before reinjection wells, etc.). In most of the recorded cases they form compact and stable corrosion product film on the metal surface, presenting a physical barrier between the metal surface and corrosive environment.^{13,17,33,114} However, cases where corrosion product film did not provide protection were observed as well.¹² This was attributed to the formation of porous and loosen layers, which easily fall off during the plant operation due to the high flow rates of geothermal fluids.

Chapter 3

Experimental Setup

3.1 Investigated materials

The focus of the research was put on steel materials currently available on the world market and commonly used as construction materials for piping and various equipment elements in different industries. Three types of steels were chosen as representatives of different grades, depending on the content of alloying elements, such as chromium, molybdenum and nickel considering their great influence on the materials corrosion behavior.^{44,16,81,39,77,78,115} The study disregarded carbon steel and focused only on alloyed steels basing on their superior corrosion performance and hence, more suitable application in geothermal systems.¹¹⁶⁻¹¹⁸ Hence, low-alloyed steel 1.7218, stainless steel 1.4404 and high-alloyed stainless steel 1.4562, were chosen for this study. The cross reference of the selected materials equivalent grades, their exact chemical composition determined with a spark emission spectrometer SPECTRO LAB and mechanical properties are shown in

Table 3.1 - Table 3.3, respectively. Additional details for each of the selected steel type are given in the further text.

3.1.1 Low-alloyed steel 1.7218

Low-alloy steel 1.7218 is a chromium-molybdenum steel with a ferritic (body-centered cubic) crystal structure. Addition of alloying elements, such as nickel, chromium, molybdenum etc., improves its mechanical properties and resistance to corrosion in certain environmental conditions, making them superior to plain carbon steel. They are widely used in oil & gas industries, and in fossil fuel and nuclear power plants.¹¹⁹

3.1.2 Stainless steel 1.4404

Stainless steel 1.4404 is an austenitic (face-centred cubic crystal structure) steel, with the widest and most significant usage in marine application. It is also regarded as a “marine grade stainless steel”.^{120,121}

Alloy 1.4404 has an excellent resistance to uniform corrosion due to its high chromium content of more than 16 wt%. Even in the atmospheres with only traces of oxygen, Cr₂O₃ passive layer readily forms on the surface, protecting the metal from the aggressive corrosive environments. Owing the additional presence of molybdenum and nickel, and low carbon content, alloy 1.4404 shows an excellent corrosion resistance when exposed to a range of corrosive environments.^{44,16,81,39,76,77,122-124} Its vulnerability is observed with an increase in temperature and concentration of halide ions that initiate localized corrosion (PREN = 23.1 - 28.5).^{88,120,121} The alloy provides excellent elevated temperature tensile, creep and stress-rupture strengths.

3.1.3 High-alloyed stainless steel 1.4562

Alloy 1.4562 is an austenitic high-alloyed stainless steel designed to bridge the cost-performance gap between standard stainless steels and nickel alloys.^{58,86,87}

Combining the advantages of high-chromium alloyed materials, i.e. an excellent resistance to corrosive attack by oxidizing media,³⁵ with molybdenum content of more than 6 %, remarkable resistance to localized corrosion is achieved in a variety of media.^{16,58,81,76,77,115,116} The alloy is also referred to as superaustenitic due to its high pitting resistance equivalent number (PREN = 50.3 - 58.6), indicating excellent resistance to pitting corrosion. Increasing the nickel content, resistance to stress corrosion cracking is improved,^{44,84}. Addition of nitrogen approved thermal stability and mechanical properties of the alloy.^{44,86} Owing the outstanding combination of local resistance, high mechanical strength and ease of workability, alloy 1.4562 has an extensive usage, particularly in chemical and petrochemical industries, environmental engineering and oil and gas production.^{86,87,124}

Table 3.1 Equivalent grades of the selected materials¹²⁵⁻¹²⁷

Germany DIN, WNr	Europe EN 10088-2	USA	
		ASTM	UNS
1.7218	25CrMo4	4130	G41300
1.4404	X2CrNiMo17-13-2	316L	S31603
1.4562	X1NiCrMoCu32-28-7	31	N08031

Table 3.2 Chemical composition of the selected materials in wt% (Fe bal.)

	C	Si	Mn	P	S	Cr	Mo	Ni	N	Cu
1.7218	0.212	0.249	1.332	0.008	0.007	0.497	0.013	0.038	0.016	-
1.4404	0.030	0.396	1.825	0.028	0.003	16.410	2.471	11.870	0.034	0.256
1.4562	0.011	0.063	1.732	0.018	0.005	26.580	6.230	32.930	0.148	1.048

Table 3.3 Mechanical properties of the selected materials¹²⁸⁻¹³⁰

Steel	T [°C]	v	R_{p0.2} [MPa]	R_m [MPa]
1.7218	20	0.28	931	1034
1.4404	20	0.28	≥ 240	530 - 680
	100	0.31*	166	420*
	150	0.32*	152	360*
	200	0.33*	137	270*
1.4562	20	0.28	≥ 276	≥ 650
	100	0.31*	210	630
	150	0.32*	195*	605*
	200	0.33*	180	580

* interpolated values

3.2 Investigated geothermal brines

Corrosion resistance of the selected materials was investigated in three artificial geothermal brines. Using commercially available reagents, the electrolyte solutions were prepared in the laboratory based on the analysis of the fluid aquifers (Table 2.1) discharged from the wells SBY-03, SBY-05, LHD-05 and LHD-23 present on Sibayak and Lahendong geothermal sites (Indonesia).^{22,23} Due to the observed geothermal system instability with time,^{21,22} the worst-case scenario respective to the corrosion was assumed.

3.2.1 Sibayak geothermal site, wells SBY-03 and SBY-05

SBY-03 and SBY-05 are production wells in cluster B on the Sibayak geothermal field (North Sumatra, Indonesia). The wells are located at 1,479 m elevation, at N 3° 13' 35.5", E 98° 30' 04.0" geographical surface coordinates. The reservoir temperature ranges between 264 °C and 310 °C and the gauge pressure varies between 45 bar and 110 bar.⁶⁵⁻⁶⁷ The brines from the wells are collected after the separator into one transmission

pipeline, having the temperature 175 °C and pressure 9 bar. The chemical composition and the resulting acidity of the artificial brine are shown in Table 3.4.

3.2.2 Lahendong geothermal site

3.2.2.1 Well LHD-05

LHD-05 is a production well in the cluster 5 on the Lahendong geothermal field. It is located at 878 m elevation, at N 1° 16' 36.49", E 124° 50' 58.67" geographical surface coordinates.⁶² The reservoir temperature is at 250 °C temperature and 150 bar pressure.⁶⁸ Above the ground the system temperature and pressure drop down to 175 °C and 9 bar. The chemical composition and the resulting acidity of the artificial brine are shown in Table 3.4.

3.2.2.2 Well LHD-23

LHD-23 is a production well in the cluster 5 on the Lahendong geothermal field. It is located at 878 m elevation, at N 1° 16' 36.49", E 124° 50' 58.67" geographical surface coordinates.⁶² The reservoir temperature is at 280 °C temperature and 120 bar pressure.⁶⁸ Above the ground the system temperature and pressure drop down to 175 °C and 9 bar. The chemical composition and the resulting acidity of the artificial brine are shown in Table 3.4.

Table 3.4 Chemical composition and the resulting acidity of the artificial geothermal brines

mg /L →	Cl ⁻	SO ₄ ²⁻	HCO ₃ ⁻	Ca ²⁺	K ⁺	Na ⁺	pH _{25 °C}
SBY	1,500	20	15	200	250	600	4
LHD-05	21	20	15	-	6	20	4
LHD-23	1,500	1,600	-	-	200	1,000	2

3.3 Methods

The experimental methods utilized in this work to evaluate the corrosion resistance of selected materials were standard electrochemical methods and exposure tests, conducted in the laboratory in the artificial geothermal brines.

3.3.1 Electrochemical techniques

Electrochemical measurements were carried out in a standard three electrode cell, consisting of a saturated Ag/AgCl reference electrode, Ti/TiO₂ net counter electrode and a working electrode made of the investigated material spot-welded on a nickel holder and

completely immersed in the testing electrolyte. Low temperature experiments were performed in glass vessels equipped with water condensers. For high temperature and pressure conditions autoclaves, equipped with manometers for pressure control and aluminum cylinder mantles to avoid heat dissipation, were used. External heating mantles and ceramic heating plates, together with a temperature regulator, precision ± 3 K, and Pt-100 sensor were employed to assure the constant heating during the experiments.

The measurements were performed using Gamry Potentiostatic System Model Reference 600. The obtained data were analyzed with Gamry Echem Analyst Software. All of the recorded electrode potentials, mentioned in the current work, are referred to the standard Ag/AgCl reference electrode potential.

3.3.1.1 Open circuit potential

Open circuit potential (E_{oc}), also referred to as the free corrosion potential (E_{corr}) is a measure of a tendency of the investigated, i.e. working electrode to dissolve (lose electrons) and undergo oxidation.¹⁰⁰ It is measured versus a stable reference electrode, when no potential or current is being applied to the electrochemical cell. Prior to the beginning of an electrochemical experiment, it is necessary to allow a sufficient time for the system to stabilize, i.e. for the various corrosion reactions to reach a constant rate. It is generally considered as a steady state when E_{oc} does not change more than 5 mV over a 10 minute period.¹³¹

E_{oc} can provide useful information about the system under study, e.g. corrosion behavior of the investigated metal, oxidation power of the electrolyte etc. However, in order to obtain information of the corrosion mechanism and quantify the corrosion rates, additional electrochemical methods need to be employed.

In the current research the steady state of the investigated systems was reached after several hours of immersion. In order to obtain a comparable corrosion behavior of the materials under study, the subsequent electrochemical methods were performed after 20 h of immersion.

3.3.1.2 Electrochemical impedance spectroscopy

Electrochemical impedance spectroscopy (EIS) is a very powerful electrochemical method that has seen a tremendous increase in popularity in recent years due to its versatile application in studying uniform^{132,133} and localized corrosion,^{134,135} elucidating reaction mechanisms,^{136,137} studying metal/solution interfaces,¹³⁸⁻¹⁴² oxide films,^{132,138} coatings,^{133,143} corrosion inhibitors effectiveness^{137,144,145} and general characterization of

surface films.^{100,132,138,141,146-148} Beside the aforementioned capabilities, its advantage over direct current techniques lies in its unlimited performance, due to the non-destructive nature, and the possibility in measuring corrosion rates in poorly conducting media,^{133,149} or of metals covered by high-resistant surface layers, such as organic coatings.^{16,128,150,151}

EIS is based on applying a small sinusoidal AC signal (potential or current) to the electrochemical cell in a steady state over a wide frequency range, and measuring the system's response. The cell voltage and current are subsequently converted into the complex impedance, Z ; a measure of the circuit ability to resist the flow of the electrical current. The obtained results are presented in Nyquist; imaginary impedance part ($-Z''$) vs. real impedance part (Z') and Bode; impedance modulus ($|Z|$) and phase angle (θ) vs. log frequency (f) plots. Considering the shape of the plots and basic assumptions regarding the nature and the structure of the system under investigation, it is possible to model its electrochemical behavior using an equivalent electrical circuit (EC) model comprised of different electrical elements, representing specific parts and/or interactions of the studied system. The precondition for the proper EIS modelling is that the selected EC has a reasonable physical interpretation of the studied system and the physicochemical events taking place in it.^{100,131,152} Assuming the correct model selection, it is possible to obtain quantitative information on the EC constructive blocs, such as solution resistance (R_s), capacitance (C), polarization resistance (R_p) etc. and that way, characterize the studied system quantitatively. In most cases the impedance response of the system shows non-ideal behavior due to the electrode surface heterogeneity or continuously distributed time-constants for charge-transfer reactions.¹⁵³ Such time-constant dispersion is commonly represented in equivalent EC as a constant phase element (CPE) instead of pure capacitance (C) and it is characterized with parameters Q and α ($\alpha \neq 1$).

In the current study a 10 mV potential perturbation was superimposed on the electrochemical system over a 100 kHz to 10 mHz frequency domain (10 points per decade) under E_{oc} conditions upon the system stabilization. After careful examination of the obtained impedance data, the electrical circuits, presented in Figure 3.1, were chosen to model the electrochemical interface of the studied systems. The number of the observed relaxation times in the impedance spectra and their relationship corresponded to the number of R-CPE loops and how they were connected in the circuit (parallel vs. series). Parallel connection of two R-CPE loops, as in Figure 3.1: B, was used to describe two different physical processes (e.g. charge transfer, diffusion, adsorption, etc.) occurring simultaneously on the electrode/solution interface. Generally, the inner layer, modelled in the current study with R-CPE (Figure 3.1: A) and R_2 -CPE₂ (Figure 3.1: B) loops, is associated with an electrical double

layer.^{152,153} To support this fact, interface capacitance was extracted from the corresponding CPE according to the equation¹⁵⁴

$$C = Q^{\frac{1}{\alpha}} \cdot \left(\frac{1}{R_s} + \frac{1}{R} \right)^{\frac{\alpha-1}{\alpha}} \quad (3.1)$$

If the capacitance value was within the range characteristic for the double layer capacitance (10 - 100 $\mu\text{F}/\text{cm}^2$), the phenomenon occurring on the electrode/solution interface was linked to the charge transfer. Accordingly, the resistance related to the capacitance was charge transfer resistance, directly associated with the single kinetically controlled electrochemical reaction. Higher capacitance is usually correlated to the evolved corrosion layer formed on the electrode surface due its oxidation.

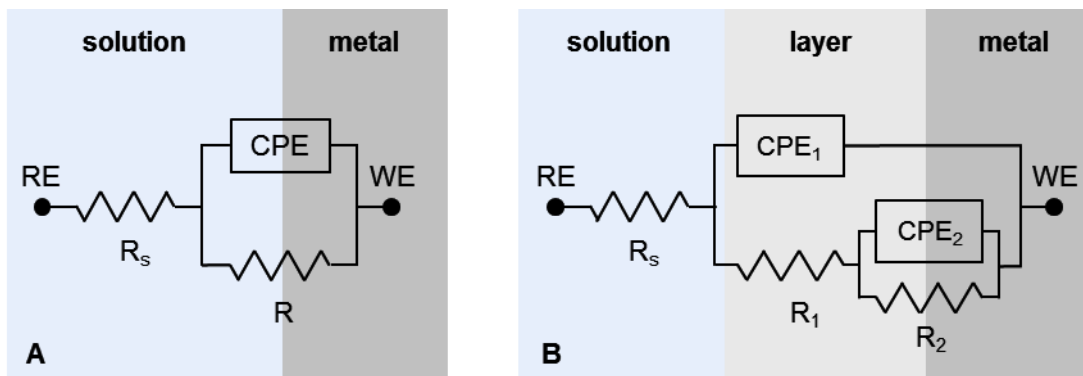


Figure 3.1 Equivalent electrical circuits used for fitting the results obtained by EIS and their physical interpretation

3.3.1.3 Tafel extrapolation method

Tafel extrapolation method is used to experimentally evaluate and predict the rate of uniform corrosion, and to study the kinetics and mechanisms of the anodic and cathodic reactions, through the short-time experiments. It is based on applying a slow linear potential sweep from -250 mV to 250 mV relative to E_{corr} , and measuring the current response of the electrochemical cell. Typical graphical output of the experiment is a plot log current density (j) vs. potential (E). From the intersection of the extrapolated linear anodic and cathodic branches at the zero overpotential, corrosion current (j_{corr}) and free corrosion potential (E_{corr}) are determined (Figure 3.2). Consequently, corrosion rate (CR) can be calculated according to the equation:¹⁵⁵

$$\text{CR} = \frac{j_{\text{corr}} \cdot M}{z \cdot F \cdot \rho} \quad (3.2)$$

Furthermore, from the slopes of Tafel lines the kinetics and the mechanisms of the corresponding reactions are elucidated.^{100,131,156-158}

One rule of thumb that needs to be taken into account for Tafel extrapolation to be valid is that the corrosion reactions need to be under the charge transfer control. Also, in order to perform an accurate extrapolation, at least one of the branches of the polarization curves should exhibit linearity over at least one decade of current density.^{100,131,159}

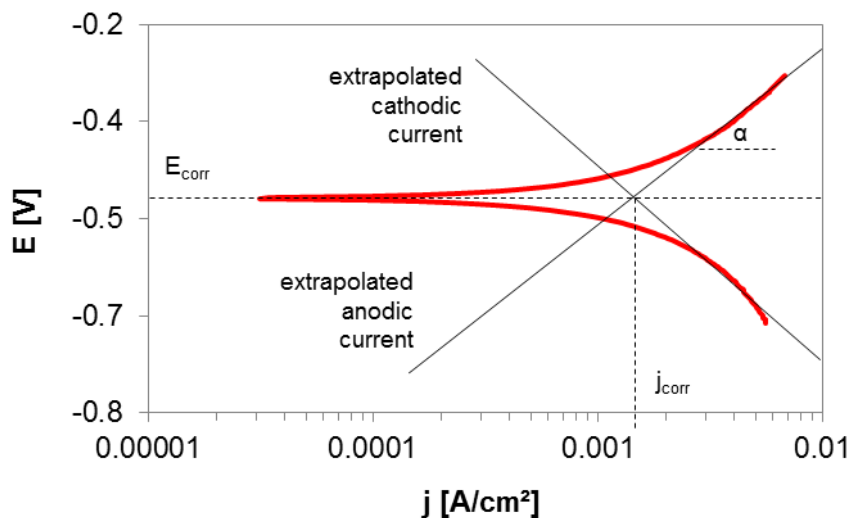


Figure 3.2 Principle of Tafel extrapolation technique

In the present study the potential range from -200 mV to 200 mV relative to E_{corr} was used, with the 0.2 mV/s sweep rate. The corrosion rate was calculated from j_{corr} , obtained from the intersection of E_{corr} line and Tafel branch that showed the linearity over at least one decade of j_{corr} .

3.3.1.4 Cyclic polarization

Potentiodynamic polarization is used for studying various aspects of corrosion. One of its major applications is in understanding the passivity of stainless steels and their susceptibility to localized corrosion.^{16,91,123,160}

The method is based on a slow linear sweep of the potential in the noble (positive, anodic) direction relative to E_{oc} and recording the resulting current (i) (Figure 3.3). In the active region of the potential scan the measured current tends to increase with the applied potential. During this *active* phase the metal corrodes (dissolves) uniformly in film-free conditions. When the passivation potential (E_{p}) is reached, a dramatic decrease of the current occurs due to the passive film formation. The beginning of the decrease is known as the *active-passive* transition. At the time of reaching the perfect passivation potential (E_{pp})

the metal surface is entirely passivated, evident by the current drop to a very low value, i_p (passive current). In the passive potential range, further potential increase usually has a little effect on the passive current density. The measured current remains very low and constant until the pitting potential (E_{pit}) is reached, signifying the beginning of the protective film breakdown. Consequently, the current tends to increase again as more and more pits propagate. In order to evaluate the repassivation ability of the investigated material, as soon as the certain, previously defined, maximum of current or potential is reached, the scan potential is reversed in the negative (active, cathodic) direction toward E_{oc} . During the reverse scan measured current decreases with potential sweep. At the intersect of a reverse scan with the forward scan, repassivation potential is determined (E_{rep}).^{45,131,161}

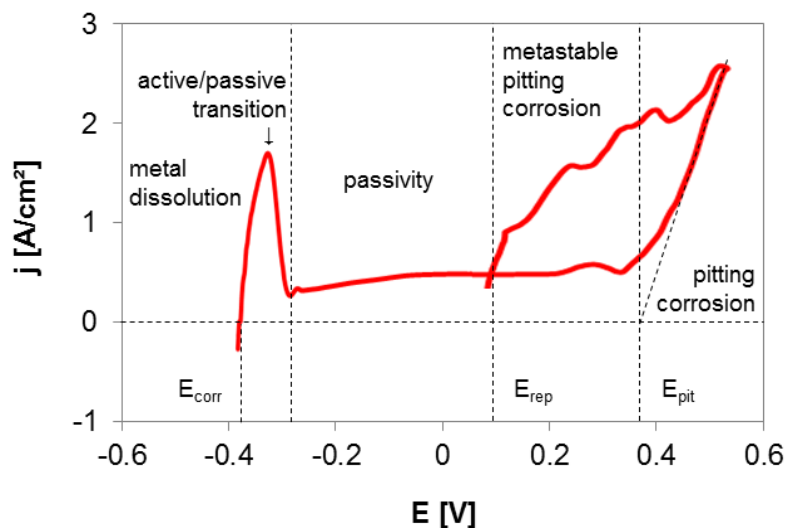


Figure 3.3 Principle of cyclic polarization technique

In the current work the potential scan started at -200 mV relative to E_{oc} and proceeded in the anodic direction with 0.2 mV/s linear sweep rate. As soon as E vs. $E_{oc} = 1.2$ V or $j_{corr} = 2$ mA/cm² was reached, the scan was reversed in the cathodic direction, back to -200 mV vs. E_{oc} . The critical potentials, E_{pit} and E_{rep} , were determined when $j_{corr} = 0.1$ mA/cm².

3.3.2 Exposure Tests

Perhaps the most common method for estimating the corrosion resistance of a material is exposing it in the environment of interest for a certain period of time and assessing the corrosion rate using different techniques. In the current work the weight loss method was used.

The tested coupons were prepared according to the ASTM G1-03 standard, weighed on an analytical laboratory scale to an accuracy 10^{-4} g, and vertically immersed in

the investigated solution for a certain time interval. After exposure, the corrosion products were firstly removed mechanically, using a paper towel and a nonmetallic bristle brush. Afterwards, it was followed by chemical cleaning in an ultrasonic bath, immersing the coupons in the solution specifically designed to remove the corrosion products with minimal dissolution of the base metal. For this purpose an aqueous solution of 250 mL/L HCl (conc.) containing 3.5 g inhibitor hexamethylenetetramine was used for pickling the surface of 1.7218 grade, and a mixture of 100 mL/L HNO₃ and 20 mL/L HF (4 wt%) for cleaning 1.4404 and 1.4562 grades.^{160,162} The coupons were subsequently weighed on the same analytical scale as prior to the exposure. The corrosion rate was determined according to the equation:¹⁶²

$$CR = \frac{m_2 - m_1}{A \cdot t \cdot \rho} \quad (3.3)$$

Low temperature tests were performed in glass vessels equipped with water condensers to avoid water evaporation. For high temperature and pressure conditions autoclaves made of 316L stainless steel with PTFE vessels were used. During the exposure, the equipment was put in a climate chamber that provided the needed heat and uniform temperature distribution.

3.3.3 Surface analysis

Upon the end of each experiment, the metal specimens were removed from the environment, rinsed with an acetone and dried in the air. For surface analysis Reichert-Jung Polyvar MET optical microscope with a 2000-fold magnification was used to determine the type of corrosion attack. If corrosion was in the localized form, the width and depth of the formed pits were determined. Additionally, cross-section of the coupons was analyzed to resolve the progress of the corrosion attack into the bare metal, and to determine the thickness and morphology of the corrosion layer formed on the metal surface.

3.4 Test setup

3.4.1 Factors influencing corrosion

Considering the occasional variation in conditions due to the instability of the geothermal systems, an influence of different parameters on the corrosion behavior of the selected materials in the static conditions was investigated by means of electrochemical methods and exposure tests.

3.4.1.1 Temperature effect

Influence of three different temperatures on the corrosion behavior of the selected materials was examined. The most extreme investigated conditions were 175 °C, where the gauge pressure in the autoclaves reached 9 bar, simulating the actual service conditions in the technical facilities above the ground (e.g. pipelines, separators, heat exchangers etc.) at Sibayak and Lahendong geothermal power plants. Additionally, to simulate the possible conditions in the pipeline after the heat exchangers, prior to the injection wells, 70 °C and 100 °C at 1 bar pressure were investigated as well.

3.4.1.2 Brine acidity

The main difference in the chemistry of the LHD-23 and SBY geothermal brines was the brine acidity (pH 2 vs. pH 4). Comparing the corrosion behavior of the materials in the aforementioned brines, it was possible to extract the influence of pH on the corrosion process. In the current work it was done at 175 °C (9 bar).

3.4.1.3 Brine concentration

Geothermal brines from the LHD-05 and SBY wells differ in the salt concentration; chlorides having the main influence on the corrosion behavior (20 mg/L vs. 1,500 mg/L). In order to determine the influence of the brine concentration, corrosion behavior of the materials in the formerly mentioned conditions was examined at 175 °C (9 bar).

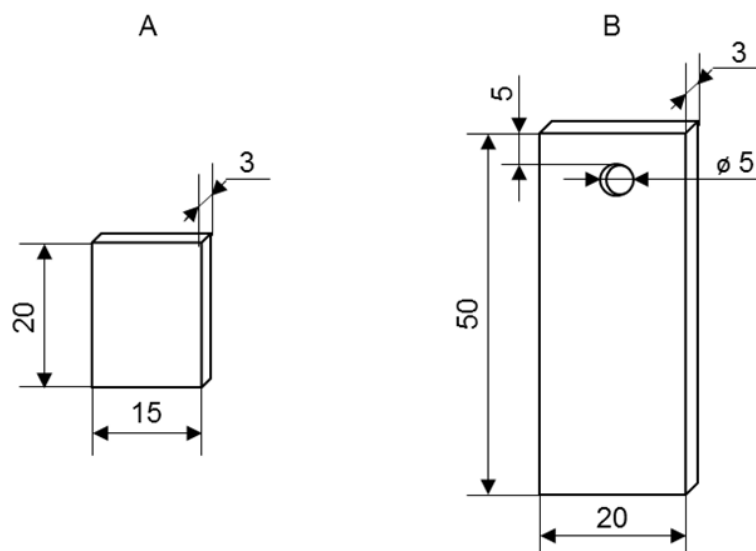


Figure 3.4 Schematic illustration of the electrodes (A) and coupons (B) used for electrochemical and exposure testing, respectively

3.4.2 Material sample preparation

The materials were provided in the form of an A4 sheet. Employing the water jet method they were cut into smaller rectangular samples, to obtain electrodes ($20 \times 15 \times 3 \text{ mm}^3$) and coupons ($50 \times 20 \times 3 \text{ mm}^3$) for electrochemical measurements and exposure tests, respectively (Figure 3.4). The electrodes were spot-welded on a metal rod made of highly resistant Nickel alloy grade 2.4886 (Figure 3.7: A). The coupons, in addition, had a 5 mm diameter hole used for fixation during the exposure tests (Figure 3.4: B and Figure 3.7: B).

Crevice corrosion susceptibility of the selected materials was examined in the artificial SBY geothermal brine at $100 \text{ }^\circ\text{C}$. The crevice was simulated using a rubber pad, imbedded on approximately 30 % of the material's surface. The electrode design for this particular test is shown in Figure 3.7: B.

Stress corrosion cracking (SCC) investigations were performed in the artificial LHD-23 geothermal brine at $175 \text{ }^\circ\text{C}$ using U-bend coupons according to the ASTM G-30 standard¹⁶³ (Figure 3.5 and Figure 3.7: C). The coupons were bent at room temperature beyond their elastic limits in order to produce a tensile stress on their surface and that way, reduce the initiation time and promote the SCC. Due to the stress relief and surface relaxation with temperature elevation, coupons were additionally tightened with titanium screw embedded in PTFE tape to avoid an occurrence of galvanic corrosion. The stresses produced on the coupons during the experimental temperature application were calculated using ANSYS Workbench Mechanical computer software.

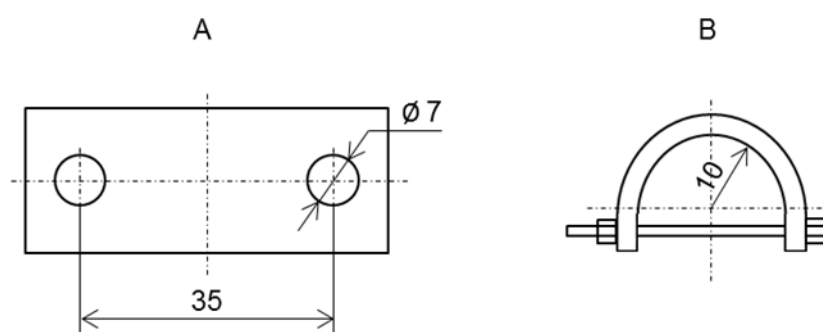


Figure 3.5 Schematic illustration of the pre-formed (A) and U-bend (B) coupons for SCC

Prior to each experiment, materials were wet ground with a 320 SiC sand paper, thoroughly rinsed with deionized water and degreased ultrasonically in alcohol and acetone to remove the residual impurities, according to the ASTM G1 standard.¹⁶² The microscopic appearance of the metals surface after the treatment is shown in Figure 3.6.

In order to assure the results reproducibility, each of the experiment set was performed three times.

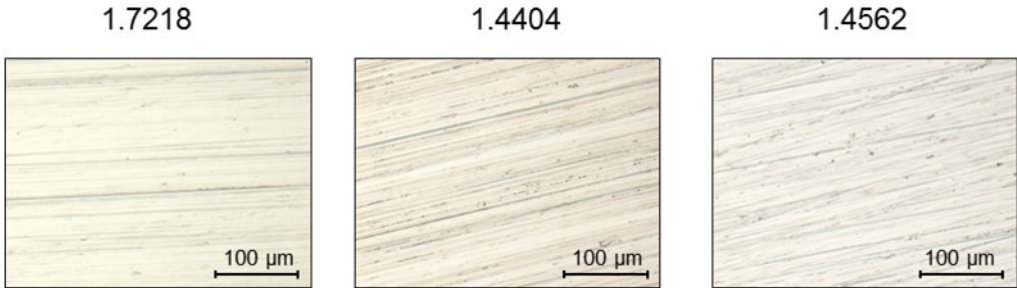


Figure 3.6 Microscopic view of the metals surface after the surface treatment and prior to the corrosion investigations

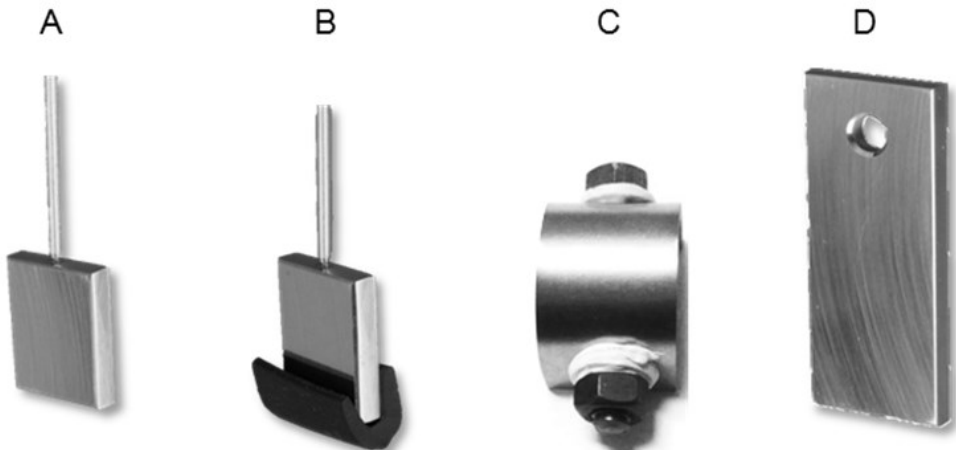


Figure 3.7 Material sample test setup for: A) electrochemical tests, B) crevice corrosion tests using electrochemical methods, C) SCC in exposure tests, D) exposure tests

Chapter 4

Corrosion Resistance of Low-alloyed Steel 1.7218

4.1 Introduction

In this chapter dependence of corrosion resistance of low-alloyed steel grade 1.7218 on various factors is evaluated, as well as the alloy's susceptibility to crevice corrosion and stress corrosion cracking. The results were obtained by means of potentiostatic (electrochemical impedance) and potentiodynamic (Tafel extrapolation) electrochemical methods, and long-term exposure tests (up to 6 months).

4.2 Corrosion film growth

Low-alloyed steels normally corrode uniformly over the entire surface. The metal dissolution starts immediately upon the immersion of the metal in the corrosive solution. The rates are highest in the beginning and tend to decrease with time due to the accumulation of corrosion products on the metal surface, providing the physical barrier between the metal and the corrosive environment.^{10,11,14,198} In what degree do the corrosion products lower the corrosion rate of low-alloyed steel 1.7218 in the artificial SBY geothermal brine at 100 °C as a function of time, is shown in the current paragraph.

4.2.1 Short-term electrochemical methods

4.2.1.1 Open circuit potential monitoring

Open circuit potentials (E_{oc}) of low-alloyed steel 1.7218 exposed in the artificial SBY geothermal brine at 100 °C were recorded during 10 days of immersion. The corresponding results are shown in Figure 4.1. E_{oc} tended to increase with time, which could be attributed to the formation of corrosion products, causing an ennoblement of the metal surface as suggested by different authors.¹⁶⁴⁻¹⁶⁶

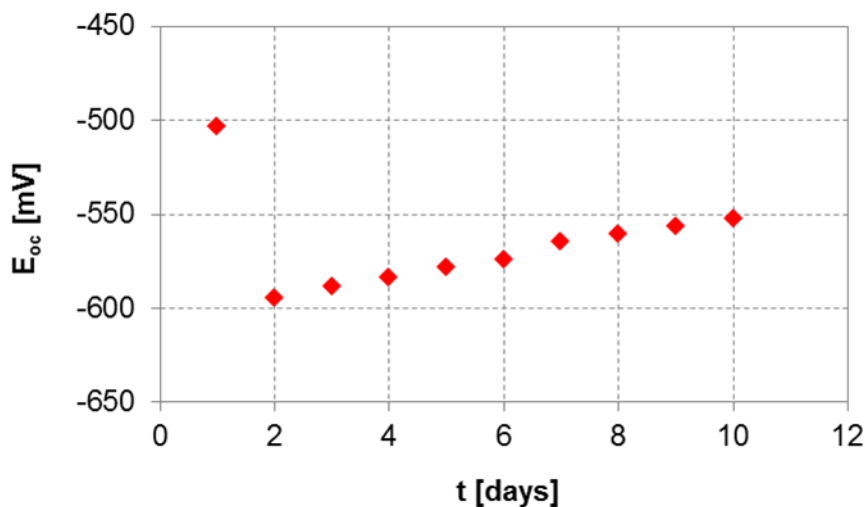


Figure 4.1 Monitoring of open circuit potential of 1.7218 steel in the artificial SBY geothermal brine at 100 °C during a 10-day immersion test

4.2.1.2 Electrode/solution interface characterization

Electrode/solution interface on the surface of 1.7218 steel was studied by means of electrochemical impedance spectroscopy during a 10-day period. The obtained results are shown in Figure 4.2. Irrespective of the immersion time, the impedance spectra resembled two depressed semi-circles, implying to the existence of two different processes occurring on the electrode surface (e. g. charge-transfer, diffusion, adsorption, etc.).¹⁵³ The diameter of the semi-circles increased with time, suggesting an increase in the impedance and relaxation time of the interface after the potential perturbation. Such findings could be linked to the evolution of a corrosion film on the electrode surface, as suggested by Frateur *et al.*,¹⁶⁷ causing the resistance increase.

According to the visual observations of the obtained spectra and the physical interpretation of the electrochemical behavior of the studied system the equivalent electrical circuit presented in Figure 3.1: B was chosen to fit the impedance data. The corresponding

results are shown in Table 4.1. A non-ideal capacitive behavior was confirmed given that α values were < 1 . According to Orazem and Tribollet,¹⁵³ this was caused by the electrode surface heterogeneity and/or continuous distribution of time constants for charge-transfer reaction. To determine which of the phenomena occurred, the true capacitance values (C) were calculated from the corresponding CPE according to Equation (3.1). Their values suggest that both layers correspond to the corrosion film and that no electrical double layer was detected on the metal/solution interface. Such finding is not unusual in the systems where thick layers of corrosion products form on the steel surface.^{144,168-171} It could be attributed either to the interference of a thick adjacent corrosion layer and its capacitance on a thin double layer, or to the too short double layer relaxation time due to which in the applied frequency range the layer was not observed experimentally, as suggested by Orazem and Tribollet.¹⁵³ Regardless of the cause, R_1 and R_2 were attributed to the resistances of the corrosion product layers formed on the electrode surface during the metal oxidation.

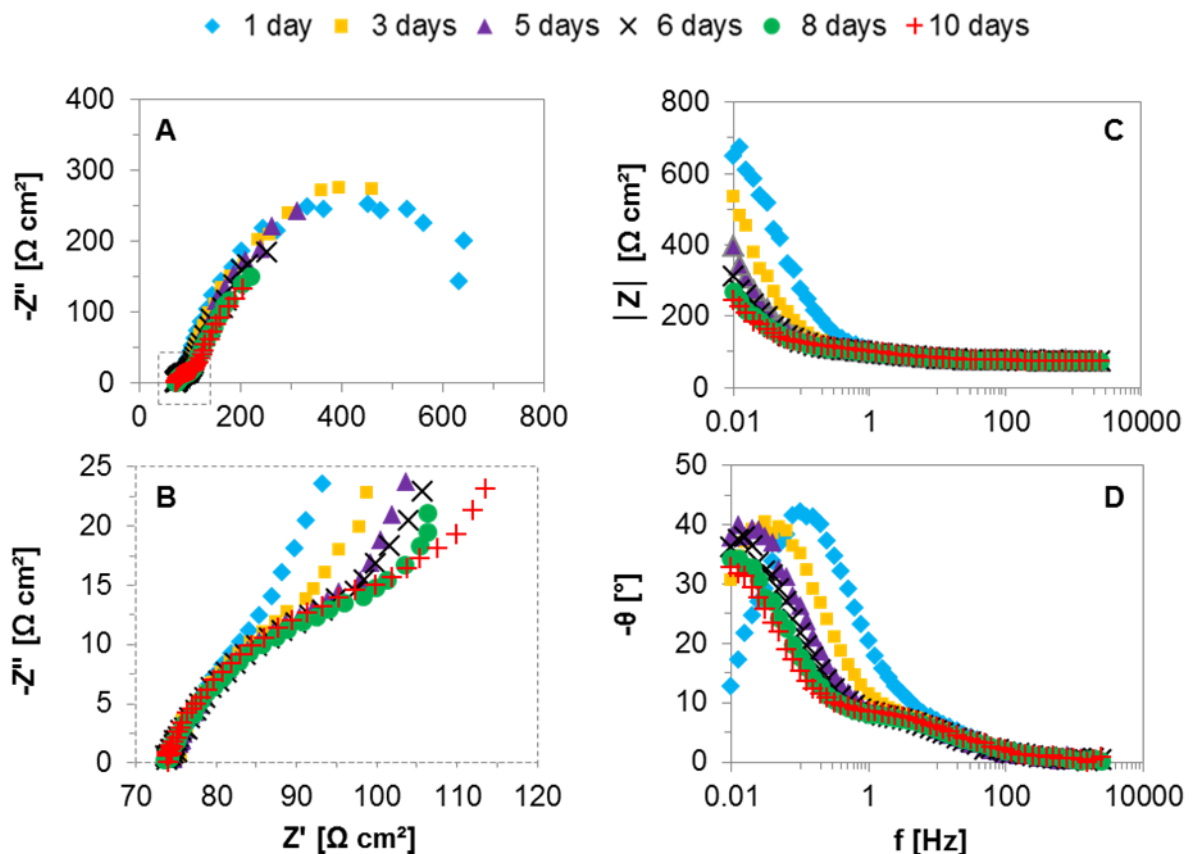


Figure 4.2 Typical impedance spectra for 1.7218 in the artificial SBY geothermal brine at 100 °C under E_{oc} conditions as a function of immersion time

Studying the characteristics of the layers and their change with immersion time, one could conclude that the outer layer, characterized with R_1 and C_1 , was much thinner in comparison

to the inner layer, characterized with R_2 and C_2 , providing lower resistance to the transfer of corrosive species toward the metal surface. According to Table 4.1, the resistance of the inner layer (R_2) increased during the first 5 days, implying to the growth of the layer. However, with further exposure time a reduction in R_2 was observed. Since the capacitance C_2 exhibited a continuous growth during the whole testing period, one could conclude that the inner layer became more porous, i.e. less compact during the 10 days of immersion. On the other hand, the outer layer showed a constant increase in the resistance R_1 and capacitance C_1 . Based on the observations, it could be assumed that the outer layer grew on the expense of the inner layer, presenting a fully oxidized form consisting of ferric (Fe^{3+}) ions. Due to the high thermodynamic stability of ferric compounds in the investigated conditions,⁷⁸ the formed corrosion film on the surface of 1.7218 could present a physical barrier between the metal and the corrosive environment that would subsequently reduce the metal oxidation rate, as shown in the research of Carter and Cramer.¹⁷

Table 4.1 Electrochemical data obtained by EIS for 1.7218 during a 10-day immersion test in the artificial SBY geothermal brine at 100 °C under E_{oc} conditions

t [days]	R_s [Ω]	R_1 [Ω cm ²]	Q_1 [mS s ^{α_1} /cm ²]	α_1	C_1 [μ F/cm ²]	R_2 [Ω cm ²]	Q_2 [mS s ^{α_2} /cm ²]	α_2	C_2 [μ F/cm ²]
1	9	31	2	0.817	922	637	4	0.860	3,157
2	9	34	3	0.776	1,188	724	7	0.842	5,795
3	9	34	4	0.733	1,384	756	10	0.826	8,909
4	9	36	4	0.712	1,526	798	13	0.815	13,151
5	9	36	4	0.699	1,604	812	18	0.805	18,442
6	9	41	6	0.629	1,735	727	25	0.782	29,293
7	9	40	5	0.640	1,611	719	29	0.752	35,568
8	9	48	6	0.618	1,784	655	33	0.790	41,155
9	9	47	5	0.632	1,753	653	35	0.758	45,935
10	9	55	6	0.605	1,970	586	39	0.782	50,626

4.2.2 Long-term exposure tests

To support and confirm the aforementioned conclusions, long-term exposure tests up to 6 months were performed. Corrosion rates, calculated according to the weight loss method (Equation (3.3)) for different exposure times, are presented in Figure 4.3. Exposing the metal coupons in the artificial SBY geothermal brine at 100 °C showed a reduction in the corrosion rate. The cross section of the exposed specimens revealed

uniform dissolution of the metal and the presence of a corrosion layer on its surface (Figure 4.4). The thickness of the layer increased significantly during 6 months of exposure; maximum thickness after 1 month was 18 μm , whilst after 6 months 54 μm . This confirms the increase of the weight loss, but due to the increased test period, the resulting corrosion rate was lower. Such observation corroborates the results obtained by EIS; an adherent and stable corrosion film formed on the surface of 1.7218 steel with time, serving as a protection to the metal from the further dissolution.

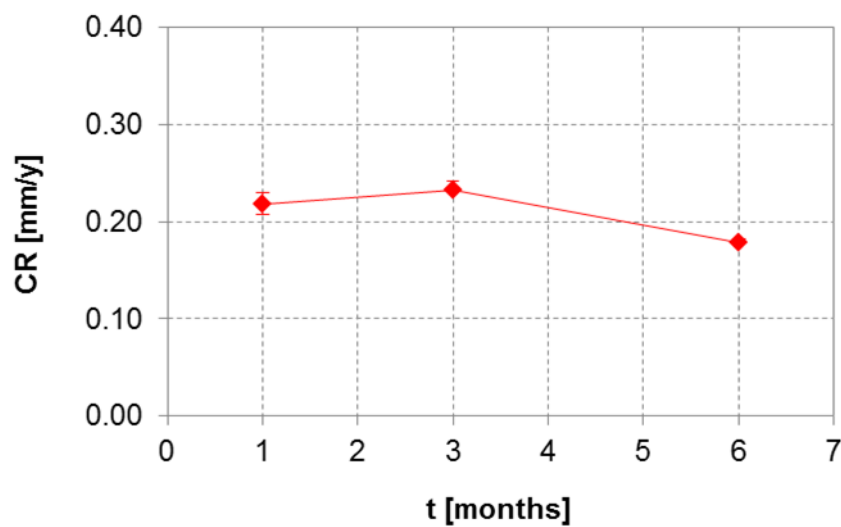


Figure 4.3 Corrosion rates of low-alloyed steel 1.7218 in the artificial SBY geothermal brine at 100 °C during a 6-month exposure test

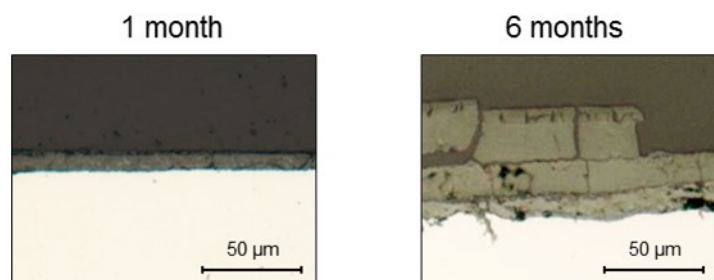


Figure 4.4 Cross section of 1.7218 coupons after 1 and 6 months of exposure in the artificial SBY geothermal brine at 100 °C

4.3 Influence of temperature on corrosion performance

Temperature effect on the corrosion behavior of 1.7218 was investigated in the artificial SBY geothermal brine at 70 °C, 100 °C and 175 °C.

4.3.1 Short-term electrochemical methods

4.3.1.1 Open circuit potential monitoring

After 20 h of immersion in the artificial SBY geothermal brine at different temperatures, open circuit potential (E_{oc}) of 1.7218 electrode surface was determined. The corresponding results are shown in Figure 4.5. Increasing the temperature E_{oc} shifted in the anodic direction, resulting in a lower affinity of the surface to oxidation. Such behavior suggests less active surface, possibly due to the accumulation of corrosion products on it, as suggested by different authors.^{10,11,185} In order to obtain more detailed information about the corrosion behavior of the studied alloy and confirm the above proposed explanation for E_{oc} ennoblement, additional testing methods were performed.

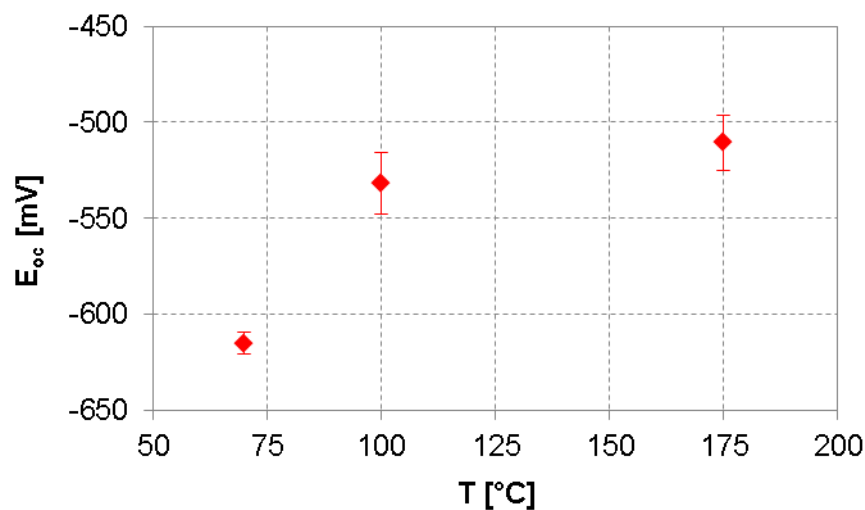


Figure 4.5 Open circuit potentials of low-alloyed steel 1.7218 in the artificial SBY geothermal brine at different temperatures

4.3.1.2 Electrode/solution interface characterization

Electrode/solution interface, formed on the surface of 1.7218 in the artificial SBY geothermal brine under E_{oc} conditions, was studied by means of electrochemical impedance spectroscopy (EIS). The temperature influence on the obtained impedance spectra is depicted in Figure 4.6. Irrespective of the temperature, the spectra resembled two overlapping distorted semicircles, implying to the existence of two processes occurring

simultaneously on the electrode surface (e.g. charge transfer, diffusion, adsorption, etc.). The high-frequency (HF) impedance loop was best defined at 70 °C. As the temperature increased, it was superpositioned with the low-frequency (LF) semi-circle, resulting in less distinguishable time constants. The diameter of the LF semi-circle increased with the temperature, indicating an increase of the resistance to the reaction occurring in this frequency range. This was supported with the Bode modulus plot (Figure 4.6: C), which showed an increase in the impedance in the LF domain with temperature.

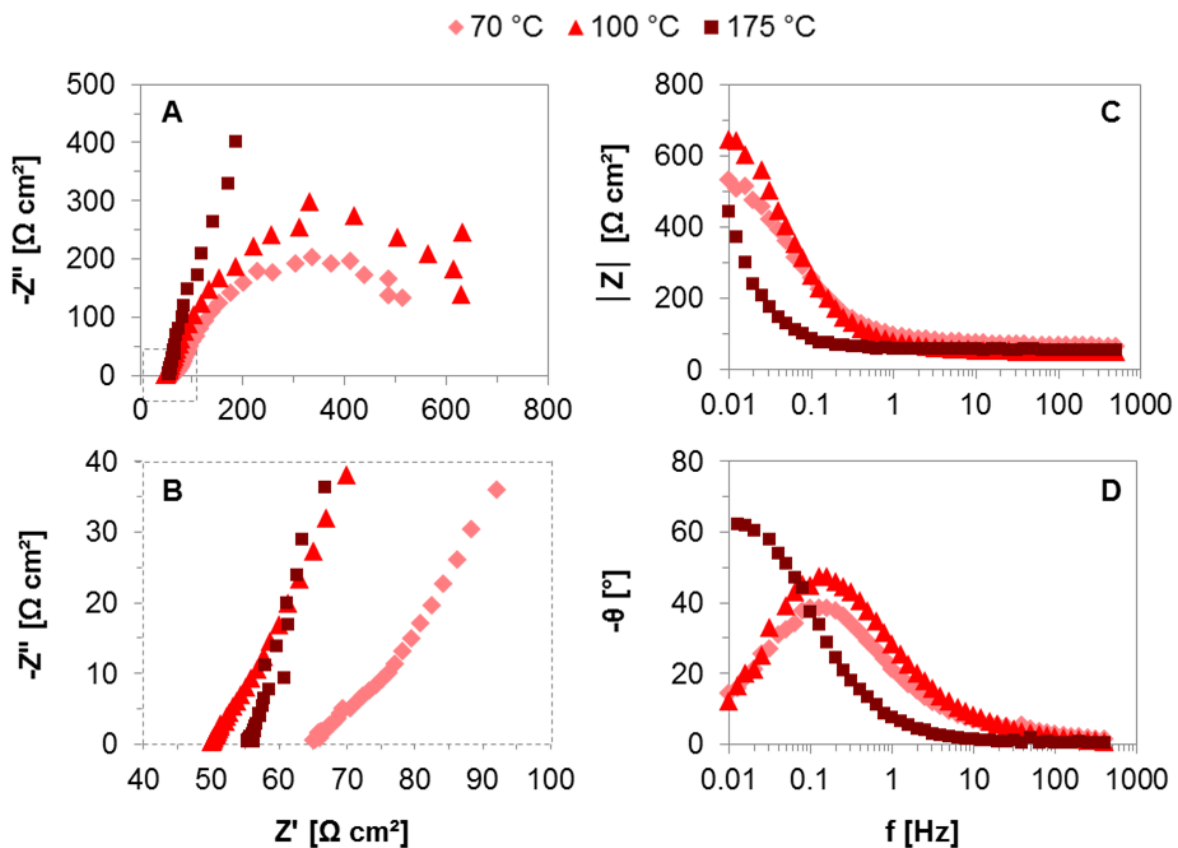


Figure 4.6 Typical impedance spectra for 1.7218 steel in the artificial SBY geothermal brine at different temperatures under E_{oc} conditions

Based on the interpretation of the spectra, the electrochemical behavior of the system was modeled with an electrical circuit presented in Figure 3.1: B. The corresponding results are shown in Table 4.2. The CPE behavior was clearly confirmed given that α values were always < 1 , irrespective of the temperature. The true capacitance values (C) calculated according to Equation (3.1), were not in the range characteristic for the double layer capacitance. It is, therefore, assumed that none of the resistances R_1 and R_2 , associated with the corresponding Q_1 and Q_2 , respectively, were attributed to the charge transfer resistances across the double layer, but to the corrosion layers formed on the electrode. Accordingly, it could be concluded that two different layers of corrosion products formed,

similar to the results of several different authors.^{144,168-171} The outer layer had a significantly lower resistance and capacitance compared to the inner layer, irrespective of the temperature. It can, therefore, be assumed that adjacent to the electrode surface a much thicker and porous inner layer was formed. Accordingly, the transport of ions to and from the electrode surface through the inner layer was a rate limiting step in the overall corrosion reaction. With the temperature increase both of the layers grew considering the increase in the resistance, indicating a buildup of corrosion products on the surface. This could eventually cause a reduction in the corrosion rate as the temperature increases, due to the reduced electrode/solution contact area. To support this assumption, Tafel extrapolation method was performed.

Table 4.2 Electrochemical data obtained by EIS for 1.7218 in the artificial SBY geothermal brine under E_{oc} conditions at different temperatures

T [°C]	R_s [Ω]	R_1 [$\Omega \text{ cm}^2$]	Q_1 [$\text{mS s}^a/\text{cm}^2$]	α_1	C_1 [$\mu\text{F}/\text{cm}^2$]	R_2 [$\Omega \text{ cm}^2$]	Q_2 [$\text{mS s}^a/\text{cm}^2$]	α_2	C_2 [$\mu\text{F}/\text{cm}^2$]
70	8	23	2	0.762	679	523	4	0.823	4,956
100	6	35	3	0.863	1,744	627	3	0.864	3,453
175	7	28	20	0.880	18,108	2,278	8	0.908	10,396

4.3.1.3 Study of corrosion reaction kinetics and mechanisms

Owing the observed fact that the low-alloyed steels corrode uniformly, Tafel extrapolation method was employed to study the corrosion reactions kinetics and mechanisms, and to predict the corrosion rates of 1.7218 in the investigated conditions. Typical polarization curves generated for 1.7218 in the artificial SBY geothermal brine at different temperatures are shown in Figure 4.7. Similar shape of the cathodic curves suggests the same mechanisms of the cathodic reactions, irrespective of the investigated temperature. Considering the conditions in which the curves were generated (aerated conditions, pH 4, negative E_{oc}) reaction occurring on the cathode was predominantly an oxygen reduction (Equation (2.2)). Linearity of the cathodic branch was clearly observed in most of the applied potential range. However, in the initial stage of the potential scan a curve non-linearity was apparent. Such behavior was perceived also in the work of Zhang *et al.*,¹⁵⁸ and they characterized it as a disturbance of a non-faradaic charging current. Very high slopes of the linear approximation of the cathodic region (201 - 399 mV/dec) compared to the anodic one (38 - 55 mV/dec) suggest overall corrosion rate was predominantly limited by the rate of reduction of oxidizing species. This is generally attributed to the potential drop on the electrode/solution interface, due to the formation of an adherent corrosion layer.¹⁷²

The shape of the anodic polarization curves pointed out to the active corrosion of the electrode surface. According to the iron Pourbaix diagram,¹⁷³ assuming the ferrous (Fe^{2+}) ion activity of 10^{-6} M and a bulk solution pH 4, at the mean E_{oc} (from the experimental curves) and for the more positive applied potentials, the following mechanisms of the anodic reactions were proposed:



Formation of ferric (Fe^{3+}) compounds generally results in a formation of a uniform non-passive conductive film on the electrode surface, thereby imparting a resistance to the electrode and causing the recorded anodic potentials to be greater than the true ones.¹⁷²

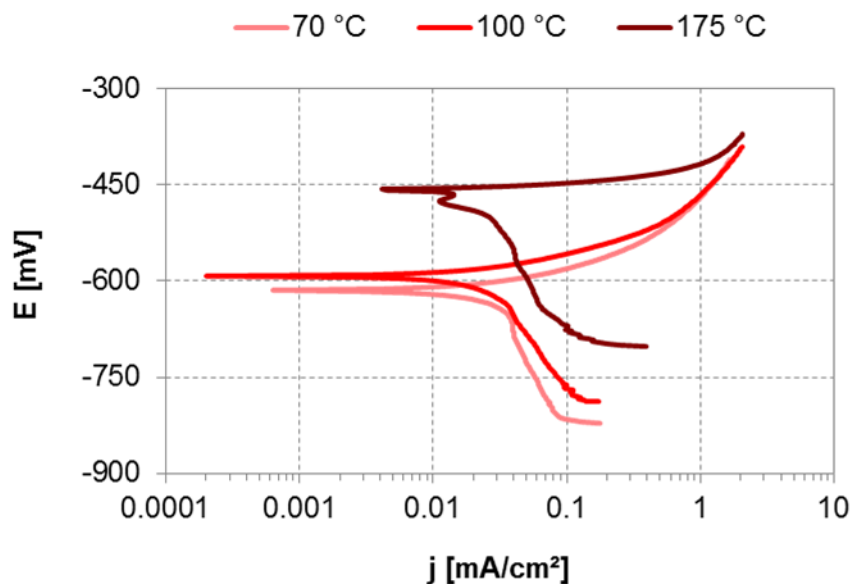


Figure 4.7 Typical cathodic and anodic polarization curves of low-alloyed steel 1.7218 in artificial SBY geothermal brine at different temperatures

This was clearly seen in the anodic branch, as the curves showed non-linearity over the complete applied potential range, especially at higher overpotentials, thereby, disobeying Tafel's law. Since the net rate of the iron dissolution on the anode is equal to the net rate of oxidants reduction on the cathode, it was possible to determine the corrosion rate by extrapolating only cathodic polarization curve to the zero overvoltage. Based on the calculations presented in Table 4.3, highest dissolution rates were observed at 100 °C. Considering the presence of only traces of oxygen in the latter conditions due to its decreased solubility, one would assume metal electrode exhibits lowest rates. However, in

the presence of other oxidants, such as hydrogen and iron ions, the electrode dissolution proceeds.⁷⁷ Moreover, formation of soluble corrosion products is favored due to the oxygen absence,¹¹⁸ resulting in an uncovered electrode surface and thus, larger corrosion rates. Interestingly, the lowest dissolution rates were observed at 175 °C. Such finding opposes to many researchers, who found a continuous growth in corrosion rate of low-alloyed steel with temperature increase, as for instance Luo and Su.¹⁷⁴ The reason for this contradiction could be in the chromium presence in alloy 1.7218. Temperature increase caused most probably higher diffusion rates of chromium from the metal matrix toward the surface,¹⁷⁵ thereby stimulating the formation of chromium (III) oxide and its incorporation into the corrosion layer, considering a higher oxygen supply due to the pressure increase. As a result more compact and stable corrosion layer formed on the surface, reducing the corrosion rate and thus, corroborating the results obtained by EIS.

Table 4.3 Electrochemical data for 1.7218 obtained by Tafel extrapolation method in the artificial SBY geothermal brine at different temperatures

T [°C]	B _a [mV/dec]	B _c [mV/dec]	j _{corr} [mA/cm ²]	E _{corr} [mV]	CR [mm/y]
70	55	399	0.0254	-614	0.29
100	62	317	0.0273	-593	0.32
175	38	201	0.0225	-553	0.26

4.3.2 Long-term exposure tests

Square coupons of low-alloyed steel 1.7218 were exposed to the artificial SBY geothermal brine up to 6 months. Temperature influence on the corrosion rates, calculated from the coupons weight loss according to Equation (3.3), are depicted in Figure 4.8. During the whole exposure time the corrosion rates were appreciably lower at 175 °C compared to the rates at lower temperature. The maximum rate was reached at 100 °C, followed by the similar values at 70 °C, clearly corroborating the results obtained by short-term electrochemical tests.

Surface analysis of the coupons exposed for 6 months at 100 °C revealed the presence of two layers on the metal surface; the red-orange loosely bound outer layer, presumably hematite, and grey-black adherent inner layer, possibly magnetite (Figure 4.9: A) as suggested by Groysman.⁷⁷ Cross section showed the metal surface corroded uniformly, with no preferential sites for localized attack. Furthermore, the overall film thickness was determined to vary between 32 μm and 58 μm (Figure 4.10: A). At 175 °C one adherent layer

was formed on the metal surface. Considering the grey-black color, it was presumably a stable magnetite layer⁷⁷ (Figure 4.10: B). Determined from the cross section analysis, the surface was attacked uniformly and the formed layer's thickness ranged between 4 μm and 24 μm (Figure 4.10: B).

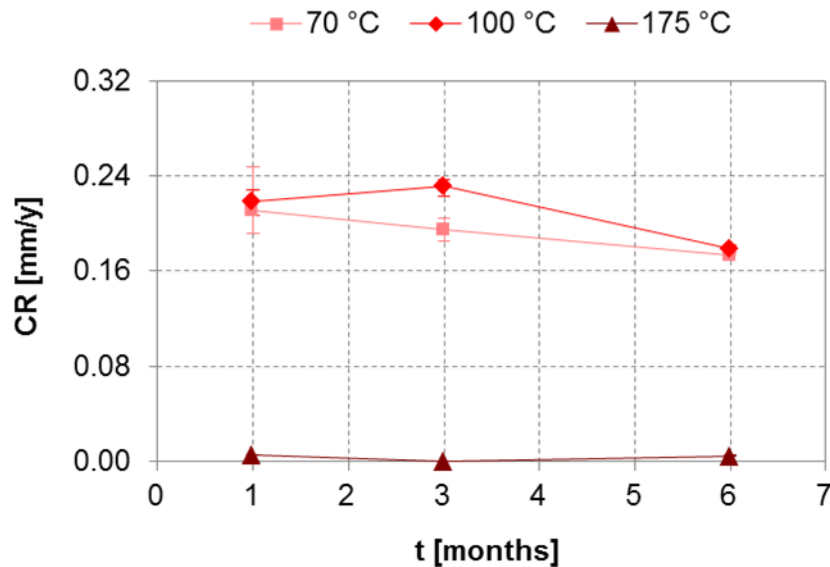


Figure 4.8 Corrosion rates of 1.7218 steel after exposure in the artificial SBY geothermal brine at different temperatures

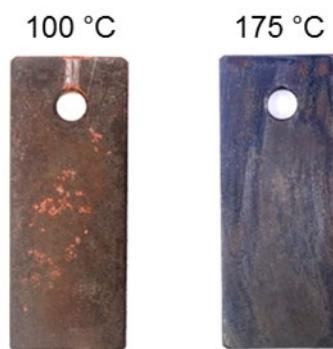


Figure 4.9 Appearance of 1.7218 coupons after 6 months of exposure in the artificial SBY geothermal brine at 100 °C and 175 °C, respectively

The observed findings showed that the corrosion film formed on the metal surface at 100 °C was thicker compared to the one formed at 175 °C. However, considering the lower corrosion rate in the latter conditions, the layer formed at 100 °C was presumably less compact, i.e. more porous. Hence, more diffusion paths through the film were present, providing an easier transfer of oxidants toward the metal surface, resulting in higher dissolution rates. The reason for such behavior could be attributed to the synergistic effect of oxygen and chromium content in the solution, and physical characteristics of the system.

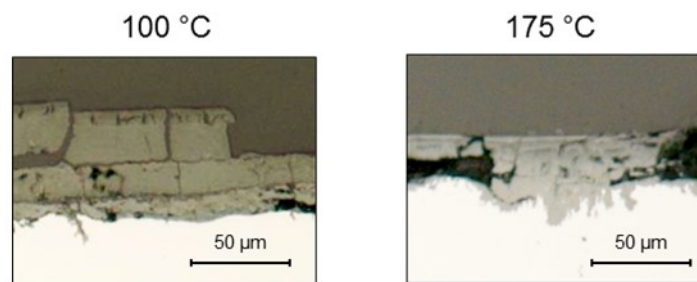


Figure 4.10 Cross section of 1.7218 coupons after 6 months of exposure in the artificial SBY geothermal brine at 100 °C and 175 °C, respectively

At 100 °C the oxygen solubility in the solution decreases, resulting in the formation of unstable, more soluble corrosion products and consequently, a porous corrosion layer. On the other hand, increasing the temperature of the closed system to 175 °C the pressure rises. This results in a higher oxygen partial pressure over the brine, leading to the increased oxygen solubility. Also, with the temperature increase diffusion of chromium from the metal matrix is accelerated, resulting in the formation of stable chromium (III) oxide, incorporated in the corrosion layer. Moreover, the medium dielectric constant decreases with temperature increase, as proven by different authors,^{101,102} leading to the formation of stable ferric compounds on the metal surface and lower conductivity of the solution, and having as a consequence lower corrosion rates at 175 °C.

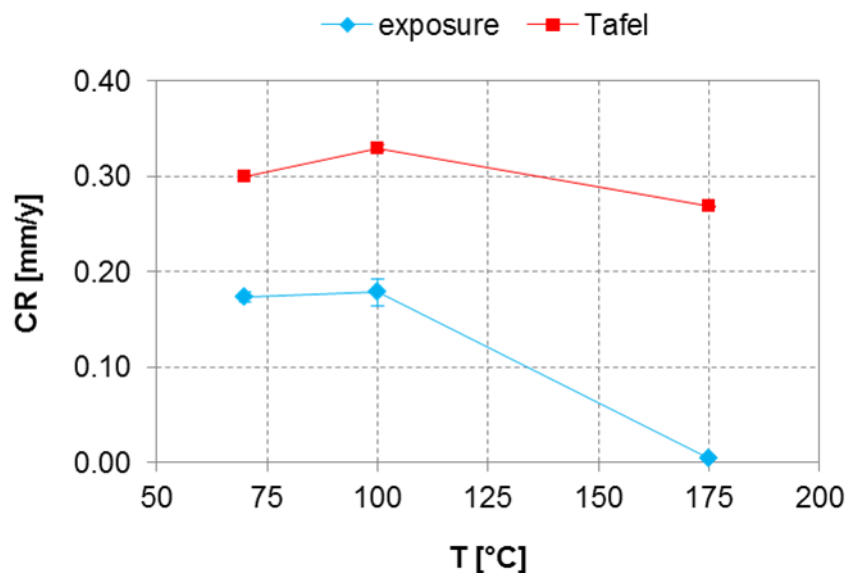


Figure 4.11 Comparison of the corrosion rates obtained by the weight loss method after 6-month exposure test and Tafel extrapolation method

In Figure 4.11 the comparison of the corrosion rates, calculated according to the coupons weight loss during 6 months of exposure, with the ones obtained by Tafel extrapolation method is presented. The same trend in the behavior of the rates was

apparent; slight increase in corrosion rate from 70 °C to 100 °C, followed by the significant reduction at 175 °C. However, a discrepancy between the results obtained with different methods was clearly visible, becoming substantial as the temperature rose to 175 °C. Poorqasemi *et al.*¹⁷⁶ explained this behavior with the fact that an adherent corrosion product film formed on the metal surface with time, decreasing the corrosion rate. Since Tafel extrapolation method was performed within the first two days of metal exposure, the layer was not as evolved as during the subsequent 6 months of exposure, resulting in higher corrosion rates compared to the weight loss tests. Nevertheless, both methods suggested the formation of an adherent corrosion layer on the metal surface at 175 °C, having the highest resistance compared to the layers formed at lower temperatures.

4.4 Influence of acidity on corrosion performance

The influence of the solution acidity on the behavior of low-alloyed steel grade 1.7218 was investigated at 175 °C in the artificial geothermal brine pH 2 (LHD-23) and pH 4 (SBY), respectively.

4.4.1 Short-term electrochemical methods

4.4.1.1 Open circuit potential monitoring

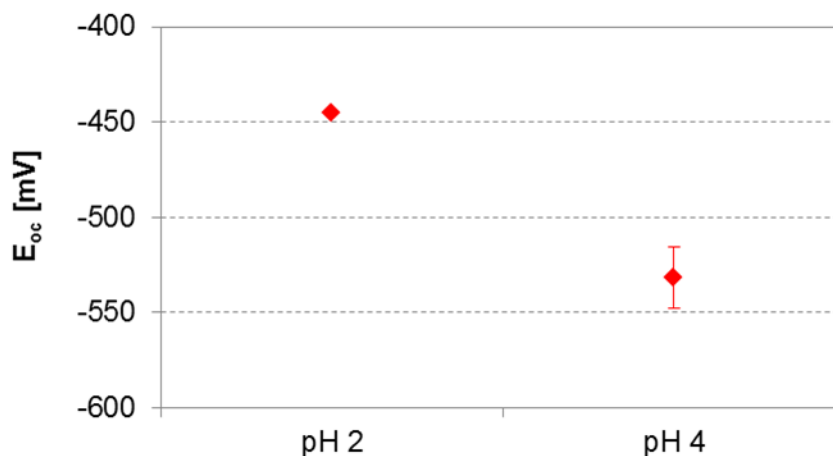


Figure 4.12 Open circuit potentials for 1.7218 after 20 h of immersion at 175 °C in the artificial geothermal brine pH 2 (LHD-23) and pH 4 (SBY), respectively

After 20 h of immersion in the investigated solutions open circuit potentials (E_{oc}) of 1.7218 were determined. The obtained results are shown in Figure 4.12. Increasing the solution acidity open circuit potential increased, suggesting lower surface activity in the solution pH 2. Such observation was in contradictions with the expected. Nevertheless, it could be explained by the assumption that upon the electrode immersion in the more acidic

solution the dissolution rate was higher. However, due to the buildup of the corrosion products on the surface, corrosion rate was reduced, resulting in a less active surface. In order to support the given explanation, additional tests were conducted.

4.4.1.2 Electrode/solution interface characterization

Electrochemical impedance spectroscopy (EIS) was used to characterize the electrode/solution interface, formed on the surface of 1.7218 steel in the solutions with different acidity. The obtained impedance spectra are depicted in Figure 4.13. Nyquist representation of the impedance data (Figure 4.13: A and B) revealed a substantial difference in the impedance of the obtained spectra in the solutions with different acidity. Two depressed overlapping semi-circles were resolved in both cases, with a better differentiation of the time constants in the more acidic brine. The reduction of the solution resistance with the pH decrease was clearly visible from the Nyquist and Bode modulus plots (Figure 4.13: A and C), indicating an increased conductivity of the solution due to the higher content of migrating ions. This could eventually lead to higher dissolution rates of the metal electrode. Substantially lower diameter of the semi-circle obtained in the more acidic conditions was apparent compared to the loop obtained at higher pH. This resulted in a significant reduction in the impedance, as can be seen from the Bode modulus plot in the low-frequency (LF) domain (Figure 4.13: C).

Based on the visual interpretation, the impedance data were fitted on the equivalent electrical circuit model shown in Figure 3.1: B. The corresponding results are given in Table 4.4. The electrode/solution interface behavior as a leaking capacitor was supported with α values being < 1 . Furthermore, a much lower α in the solution pH 2 implied to a rougher surface compared to the solution pH 4. True capacitance values (C) calculated according to the Equation (3.1), were not within the range characteristic for a double layer capacitance, irrespective of the solution acidity. Hence, the corresponding resistances R_1 and R_2 were not linked to the charge transfer resistances, but to the resistances of the corrosion layers formed on the electrode surface. Consequently, one could assume a corrosion film consisting of two layers with different physical characteristics formed. In both solutions the outer layer exhibited lower resistance R_1 and capacitance C_1 , compared to the corresponding values of the inner layer, suggesting its lower thickness. Consequently, the rate limiting step of the overall corrosion reaction was the transfer of ions to and from the electrode surface through the thick, but porous inner layer formed during the metal dissolution.

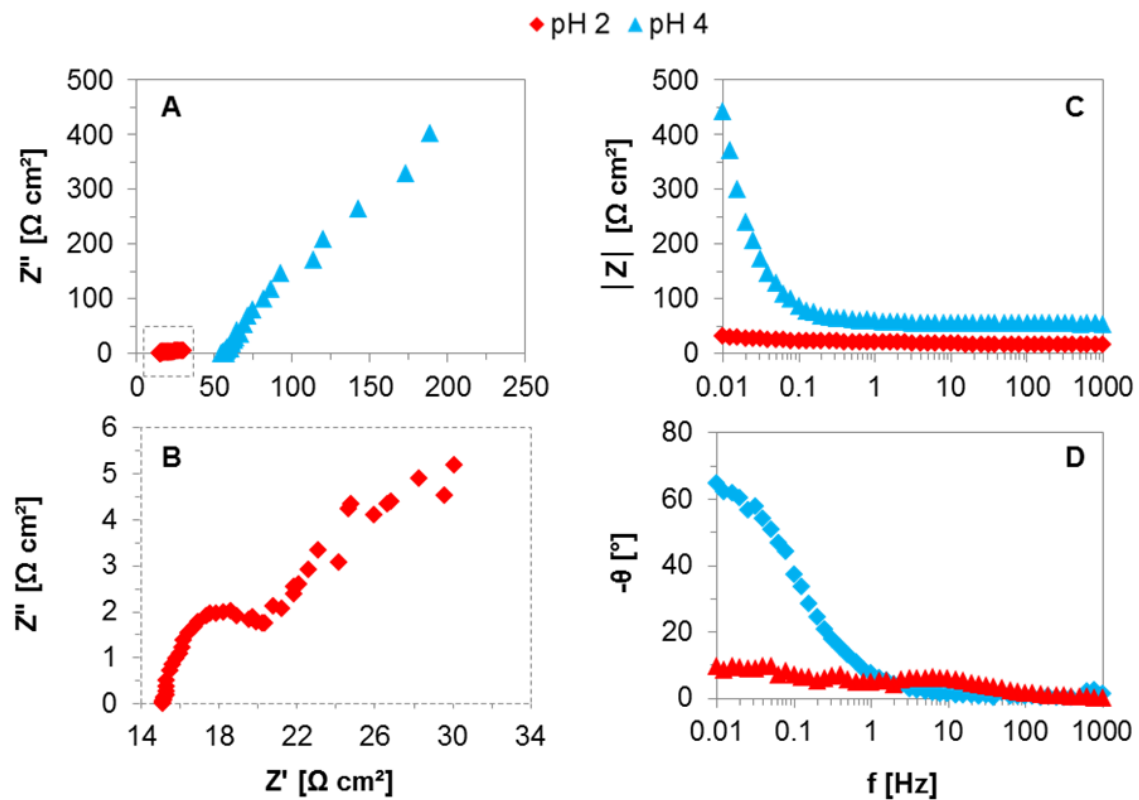


Figure 4.13 Typical impedance spectra for 1.7218 at 175 °C under E_{oc} conditions in the artificial geothermal brine pH 2 (LHD-23) and pH 4 (SBY), respectively

Table 4.4 Electrochemical data obtained by EIS for 1.7218 at 175 °C under E_{oc} conditions in the artificial geothermal brine pH 2 (LHD-23) and pH 4 (SBY), respectively

pH	R_s [Ω]	R_1 [$\Omega \text{ cm}^2$]	Q_1 [$\text{mS s}^{\alpha_1}/\text{cm}^2$]	α_1	C_1 [mF/cm^2]	R_2 [$\Omega \text{ cm}^2$]	Q_2 [$\text{mS s}^{\alpha_2}/\text{cm}^2$]	α_2	C_2 [mF/cm^2]
2	2	6	13	0.745	6	16	309	0.672	668
4	7	28	20	0.880	19	2,278	8	0.908	10

Comparing the characteristics of the inner layers formed on the electrode surface in the solutions with different acidity, one can assume a much thicker, i.e. stable, corrosion layer was formed in the less acidic solution. Due to the extreme acidic conditions in the solution pH 2, the formed corrosion products were unstable, and thus, dissolved in the solution. This could be an additional reason why the solution resistance R_s was lower in pH 2 conditions, beside the high hydrogen content. Furthermore, substantially lower resistance (> 2 orders of magnitude) and higher capacitance (> 1 order of magnitude) were perceived in the solution pH 2. Such findings suggested the formation of a much thinner, more porous and less stable corrosion layer, providing less protection to the electrode surface compared to the layer formed at pH 4. Consequently, increasing the solution acidity, i.e. lowering the pH,

higher dissolution rates of the metal electrode are expected. To support this assumption, additional testing methods were performed.

4.4.1.3 Study of corrosion reaction kinetics and mechanisms

Typical cathodic and anodic polarization curves for 1.7218 recorded at 175 °C in the artificial geothermal brine pH 2 (LHD-23) and pH 4 (SBY), respectively, are depicted in Figure 4.14. The electrochemical data determined from the curves are shown in Table 4.5. The polarization curves were shifted appreciably toward higher corrosion current densities as the pH decreased from 4 to 2. The reason for such behavior could be ascribed to the increase in the concentration of hydrogen ions, which were the main species driving the cathodic reduction reaction in the low pH conditions (Equation (2.10)). Examining the

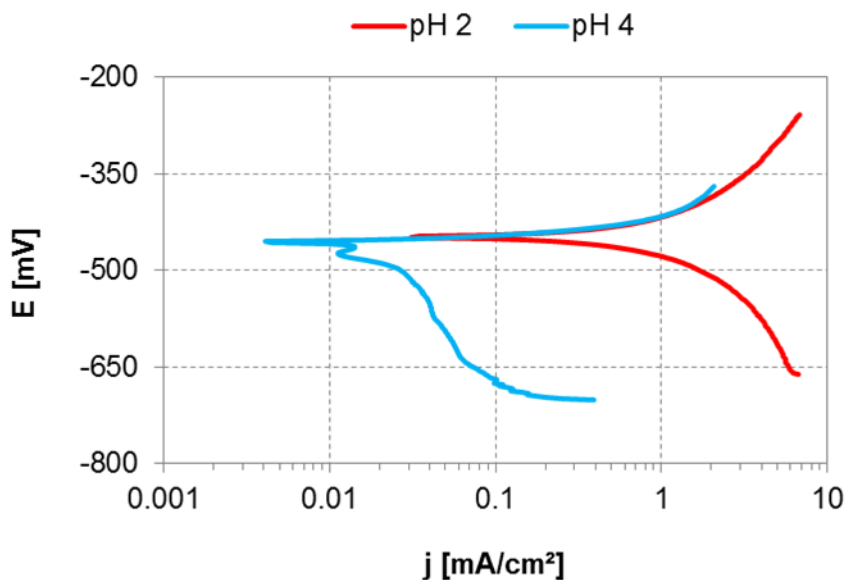


Figure 4.14 Typical cathodic and anodic polarization curves of 1.7218 in the artificial geothermal brine pH 2 (LHD-23) and pH 4 (SBY), respectively

cathodic and anodic polarization curves in the low pH brine, a non-linearity was observed in both branches. The deviations from Tafel behavior could be attributed to the buildup of dissolved metal cations near the electrode surface and/or formed hydrogen bubbles as the corrosion rate increased, which eventually blocked the electrode surface and hindered the oxidants transport to the electrode. As a result, both anodic and cathodic reactions were under the concentration (mass transport) rather than the activation (charge transfer) control, suggested also by the high Tafel slopes (B_a and B_c) shown in Table 4.5. Such findings corroborated the assumption of the more positive E_{oc} in the lower pH brine. However, absence of the linearity region on the Tafel plot could lead to an imprecise extrapolation of the polarization curves and erroneous corrosion rates. Whether the calculated corrosion rate

of more than 15 mm/y in the brine pH 2 (Table 4.5) represented reasonable result or was overestimated, forthcoming long-term exposure test revealed. Nevertheless, higher corrosion rates in the more acidic conditions confirmed the assumption made based on the EIS results.

Table 4.5 Electrochemical data of 1.7218 in the artificial SBY and LHD-23 geothermal brines at 175 °C obtained by Tafel extrapolation method

pH	B_a [mV/dec]	B_c [mV/dec]	J_{corr} [mA/cm ²]	E_{corr} [mV]	CR [mm/y]
2	257	264	1.3500	-449	15.62
4	38	201	0.0225	-553	0.26

4.4.2 Long-term exposure tests

Low-alloyed steel 1.7218 coupons were exposed for different time periods at 175 °C to the artificial brine pH 2 and pH 4, respectively. The influence of the brine acidity on the corrosion rate, calculated according to Equation (3.3), is depicted in Figure 4.15. Metal dissolution rate increased up to 2 orders of magnitude with the solution pH decrease. This was in accordance with literature,⁷⁷ which highlights a strong dependence of the corrosion rate on the solution acidity below pH 4. The anodic dissolution of the metal was effectively facilitated by the abundance of hydrogen ions present in the LHD-23 solution, which generated large cathodic currents. Reduction in the corrosion rates with time was observed during the exposure tests. This occurred presumably due to the accumulation of cations and/or hydrogen near the metal surface, resulting in a hindered transfer of oxidants toward the metal surface. Hence, cathodic and, consequently, anodic currents were reduced. This was also noticed with Tafel extrapolation method, where the signs of the mass transport control were clearly visible, even after only 2 days of metal immersion in the more acidic solution. However, the substantial difference in the calculated corrosion rates obtained by Tafel extrapolation and exposure tests (Table 4.5, Figure 4.15) could be attributed to the evolved corrosion layer during the long-term exposure tests, resulting in reduced corrosion rates.

Surface analysis of the coupons exposed in the solutions with different acidity revealed a clear difference in the composition of the corrosion layer formed on the surface (Figure 4.16). In the less acidic solution a grey-black layer, presumably magnetite⁷⁷ was formed. Increasing the solution acidity, an adherent greenish layer was present on the surface. This could be a stable ferrous hydroxide resulting from a previously formed ferrous sulphate (Equation (2.7)) due to the increased sulphate concentration present in the LHD-23 solution.

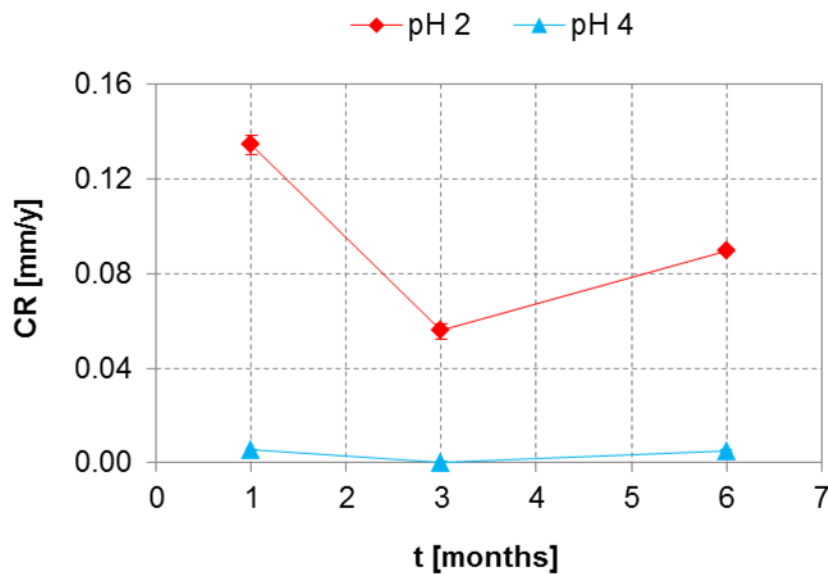


Figure 4.15 Corrosion rates of 1.7218 after exposure at 175 °C in artificial geothermal brine pH 2 and pH 4, respectively

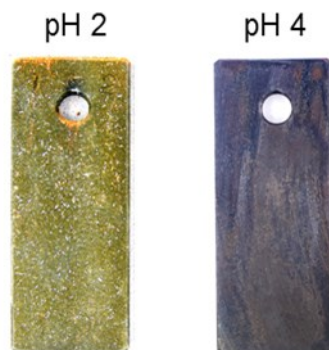


Figure 4.16 Appearance of 1.7218 coupons after 6 months of exposure at 175 °C in the artificial geothermal brine pH 2 (LHD-23) and pH 4 (SBY), respectively

Cross section of the exposed coupons (Figure 4.17) revealed that the corrosion attack occurred uniformly over the entire coupon surface, with no preferential local sites, irrespective of the exposed conditions. The thickness of the formed layer varied between 42 μm and 84 μm in the more acidic brine, which was up to 20 times greater than the thickness of the layer formed in the less acidic conditions (4 μm - 24 μm). Considering that the corrosion rates were much higher in the more acidic solution, one could assume that the layer formed in the latter conditions was less compact, supporting conclusions made based on the EIS. Consequently, the existence of a larger amount of diffusion paths through the surface layer enabled an easier transport of the oxidizing species from the bulk solution toward the bare metal, resulting in the higher metal dissolution rates.

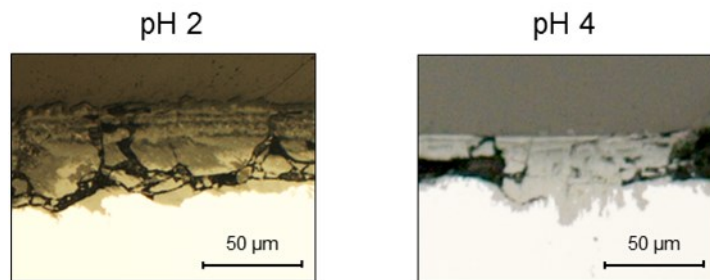


Figure 4.17 Cross section of 1.7218 coupons after 6 months of exposure at 175 °C in the artificial geothermal brine pH 2 (LHD-23) and pH 4 (SBY), respectively

4.5 Influence of salt concentration on corrosion performance

The effect of the increased salt concentration on the corrosion behavior of 1.7218 was investigated at 175 °C in the artificial geothermal brines containing 20 mg/L (LHD-05) and 1,500 mg/L (SBY) chlorides.

4.5.1 Short-term electrochemical methods

4.5.1.1 Open circuit potential monitoring

Open circuit potentials (E_{oc}) of 1.7218 electrodes after 20 h of immersion in the artificial geothermal brine containing 20 mg/L (LHD-05) and 1,500 mg/L (SBY) chlorides are shown in Figure 4.18. Increasing the salt concentration in the solution, E_{oc} is shifted in the cathodic direction. Possible explanation for such behavior could be the “salting out” phenomenon;¹⁷⁷⁻¹⁷⁹ due to the presence of more ionic species in the SBY brine, the affinity of

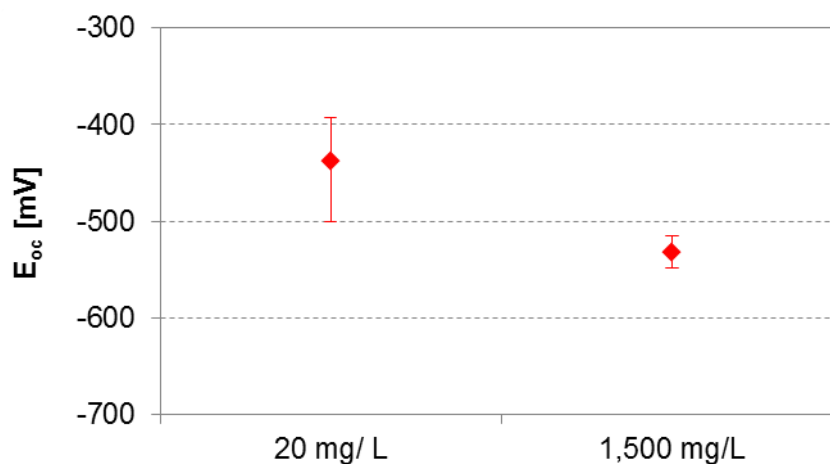


Figure 4.18 Open circuit potentials of 1.7218 after 20 h of immersion at 175 °C in the artificial geothermal brine containing 20 mg/L (LHD-05) and 1,500 mg/L (SBY) chlorides

the non-polar oxygen molecules to the polar water is reduced, resulting in a decreased oxygen solubility in the solution. Since only in the presence of sufficient oxygen concentration adherent ferric compounds could form on the surface, in the brine containing higher chloride concentration mostly soluble corrosion products form. Therefore, the surface tends to be more active than in the brine containing lower amount of salt. Furthermore, chlorides form soluble, unstable complexes with iron, hygroscopic in nature, and that way enhance the surface electrolyte formation. As a consequence corrosion attack is further stimulated and the metal surface exhibits more active potentials.

4.5.1.2 Electrode/solution interface characterization

To study the influence of salt concentration on the electrode/solution interface, electrochemical impedance spectroscopy (EIS) was performed under E_{oc} conditions in the artificial geothermal brine containing 20 mg/L (LHD-05) and 1,500 mg/L (SBY) chlorides, respectively. The obtained impedance spectra are presented in Figure 4.19. Nyquist representation of the impedance data (Figure 4.19: A) revealed a high amount of perturbations in the low-frequency (LF) domain of the spectrum recorded in the brine containing less chloride. Such phenomena could be explained by the synergistic effect of the low brine conductivity ($\kappa < 200 \mu\text{S}/\text{cm}^2$), unstable electrode surface due to the active dissolution, and the surrounding artifacts that induced the electrical field and thus, the observed noise. It was, therefore, impossible to obtain a clear system response in the LF domain in the less concentrated solution. Due to this fact, employing a model that would describe the electrochemical interface did not make much sense and it was, therefore, in this case neglected. Only visual evaluation and comparison of the obtained spectra in the investigated conditions are given in the further text.

Increasing the chloride content, solution resistance decreased from approximately 45Ω to 7Ω (Figure 4.19: A). This was clearly understandable, due to the fact that with the addition of soluble salts to a solution, the salts tend to dissolve into ions and hence, increase the solution conductivity. This could have as a consequence higher corrosion rates of the immersed metal. A non-ideal capacitive behavior of the metal/solution interface in the less concentrated conditions was observed. Such behavior was ascribed to the surface heterogeneity, which causes the frequency distribution of the capacitance and impedance across it. Therefore, the interface behaved like a leaking capacitor. According to the Bode phase angle plot (Figure 4.19: C), the surface of the electrode, exposed to the brine containing higher chloride concentration, seemed to be smoother and hence, did not cause such time constant distributions. Applying lower frequency perturbation signal to the examined systems, a much smoother slope of the Bode modulus impedance curve was

noticed in the solution containing 20 mg/L chlorides (Figure 4.19: B). Such finding proposed a lower impedance of the interface and thus, higher dissolution rates of the metal electrode in the latter conditions, corroborating the assumption made according to the E_{oc} recordings.

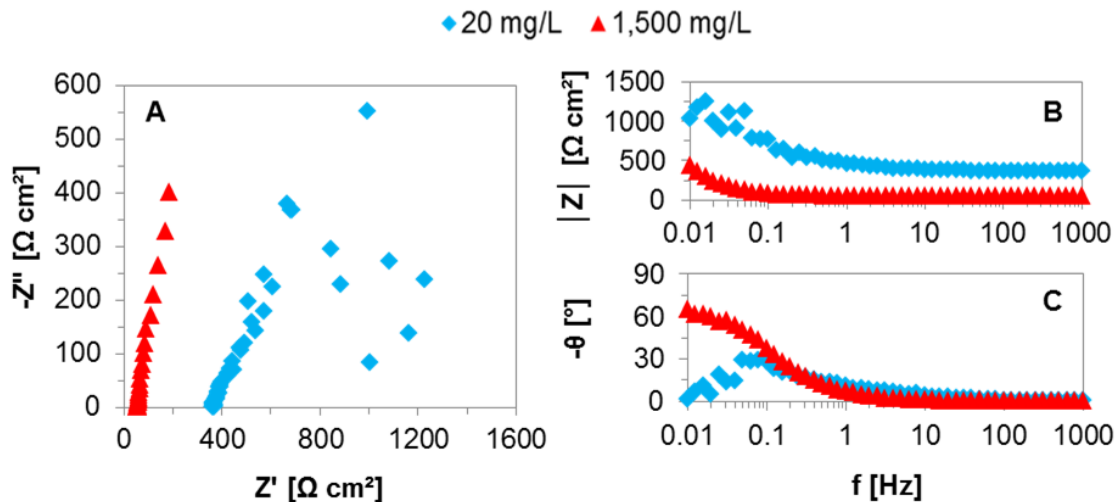


Figure 4.19 Typical impedance spectra for 1.7218 at 175 °C under E_{oc} conditions in the artificial geothermal brine containing 20 mg/L (LHD-05) and 1,500 mg/L (SBY) chlorides

4.5.1.3 Study of corrosion reaction kinetics and mechanisms

Typical cathodic and anodic polarization curves for 1.7218 recorded at 175 °C in the artificial geothermal brine containing 20 mg/L (LHD-05) and 1,500 mg/L (SBY) chlorides, respectively, are presented in Figure 4.20. The electrochemical data determined from the curves are shown in Table 4.6. Increasing the chloride concentration polarization curves shifted toward more active potentials, but lower current densities. Cathodic branch exhibited linearity in a short potential region and thus, not behaving completely according to Tafel's law. Nevertheless, the slope of the extrapolated linear region was rather high (Table 4.6), indicating mass transport control of the oxidants toward the electrode surface. In the solution containing less chloride, cathodic Tafel slope was lower, suggesting faster cathodic reaction. Considering the conditions in which the curves were generated (aerated conditions, pH 4, negative E_{oc}), cathodic reaction was in both conditions predominantly an oxygen reduction (Equation (2.2)). The difference in the cathodic behavior in the investigated conditions could be attributed to the difference in oxygen concentration. In the solution containing more chlorides (and other ionic species), oxygen concentration was lower, resulting in the deficiency of the oxygen on the electrode surface, needed to drive the cathodic reaction. Consequently, the anodic reaction rate was expected to be lower in SBY brine. However, according to the extremely flattened anodic curve, i.e. low anodic Tafel slope, significantly high(er) electrode anodic rate was observed. Such behavior could be ascribed to the

presence of other oxidizing species, such as hydrogen and iron ions, generated from the electrode dissolution, that were reduced on the cathode and stimulated the anodic reaction. Moreover, the so-formed corrosion products were not as stable as ferric oxides formed in the presence of sufficient oxygen content. As a result, loosely adhered and soluble corrosion products formed on the electrode surface, exposing the surface to the corrosive environment.

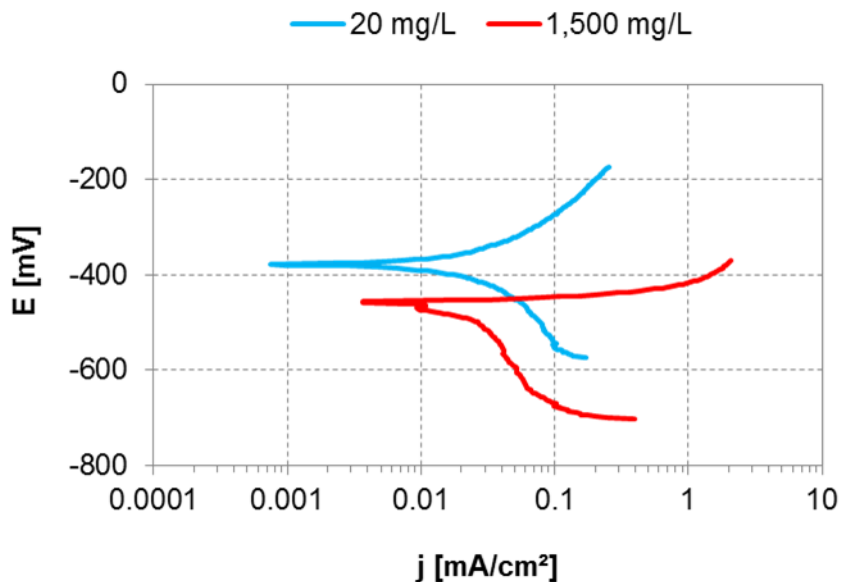


Figure 4.20 Typical cathodic and anodic polarization curves of 1.7218 at 175 °C in the artificial geothermal brine containing 20 mg/L (LHD-05) and 1,500 mg/L (SBY) chlorides

Table 4.6 Electrochemical data of 1.7218 determined from the polarization curves at 175 °C in the artificial geothermal brine containing 20 mg/L (LHD-05) and 1,500 mg/L (SBY) chlorides

$c(\text{Cl}^-)$ [mg/L]	B_a [mV/dec]	B_c [mV/dec]	j_{corr} [mA/cm ²]	E_{corr} [mV]	CR [mm/y]
20	113	126	0.0274	-379	0.32
1,500	38	201	0.0225	-553	0.26

On the other hand, in the brine with less chloride, higher anodic Tafel slope was observed, suggesting a buildup of metal cations on the electrode surface, causing a concentration effect. This could be attributed to the sufficient oxygen concentration, resulting in the formation of stable ferric oxide corrosion layer, causing a reduction in the anodic current. However, the overall reaction rate suggested lower electrode dissolution rate in the brine containing more chlorides, supporting the observations made by EIS and pointing out to the cathodic reaction as a rate limiting step in the overall corrosion reaction.

4.5.2 Long-term exposure tests

Low-alloyed steel 1.7218 coupons were exposed for different time periods at 175 °C to the artificial brine containing 20 mg/L (LHD-05) and 1,500 mg/L (SBY) chlorides. The influence of the solution concentration on the corrosion rate, calculated according to Equation (3.3), is presented in Figure 4.21. Weight loss tests revealed lower corrosion rates in the more concentrated solution through the whole exposure time, which was in agreement with the results obtained by short-term electrochemical methods. The rates were up to almost one order of magnitude lower, compared to the ones in the solution containing less salt. Presumably, the main reason for such observation was the higher oxygen content in the less concentrated solution that drove the cathodic reaction and thus, accelerated the anodic dissolution rates. During the exposure time, an inconsistency in the corrosion rate was noticed. After 3 months of exposure, the rate decreased to half in both conditions, whilst with further exposure the rate increased to the values similar after the first month of exposure. This could be linked to the corrosion products build up and falling off from the surface, due to the coupons vertical position in the vessel, resulting in metal surface exposure to the corrosive solution.

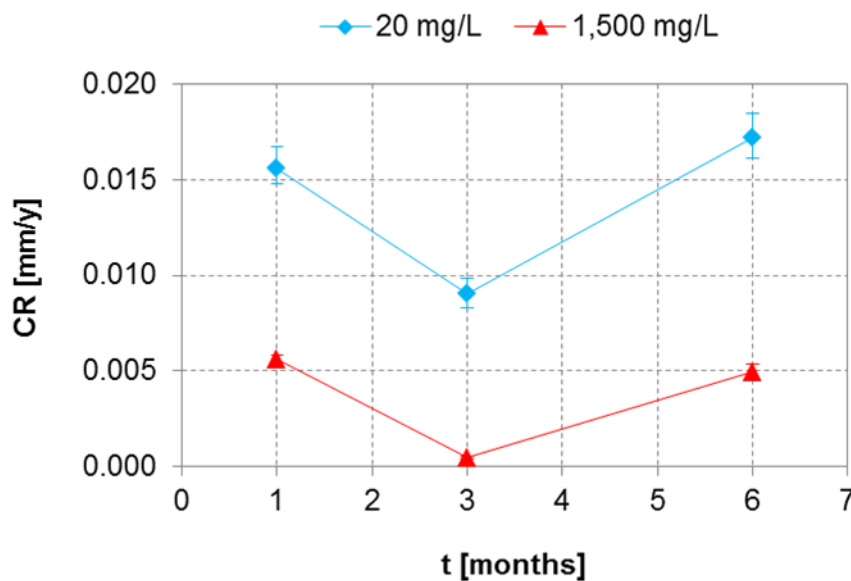


Figure 4.21 Corrosion rates of 1.7218 after exposure at 175 °C in the artificial geothermal brine containing 20 mg/L (LHD-05) and 1,500 mg/L (SBY) chlorides, respectively

Surface analysis of the exposed coupons revealed the difference in the corrosion layers formed on the metal surface after 6 months of exposure (Figure 4.22). In the more concentrated solution, one adherent grey-black layer, presumably magnetite was formed. On the surface of the coupons exposed in the less concentrated solution two layers were observed; a loosely bound orange outer layer, presumably hematite, and adherent grey-

black inner layer, possibly magnetite. Cross section of the coupons revealed in both cases uniform corrosion attack over the entire surface, without the preferential sites for localized attack (Figure 4.23). The film thickness ranged between 12 μm and 20 μm in the less concentrated solution, and between 4 μm and 20 μm in the more concentrated solution. Accordingly, corrosion films formed on the coupon surface during the 6 months of exposure at 175 °C in the artificial geothermal brines containing different salt concentration have similar thickness. However, considering the difference in the corrosion rate, the film formed in the less concentrated conditions was apparently more porous, resulting in the presence of more diffusion paths. That way, oxidizing species migrated easily toward the metal surface, resulting in higher cathodic reaction rate and, consequently, faster metal dissolution.

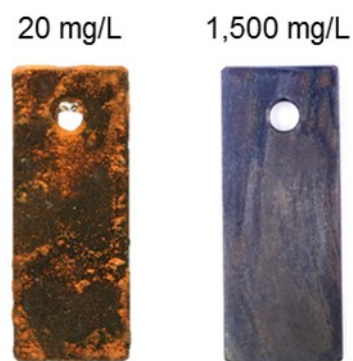


Figure 4.22 Appearance of 1.7218 coupons after 6 months of exposure at 175 °C in the artificial geothermal brine containing 20 mg/L (LHD-05) and 1,500 mg/L (SBY) chlorides

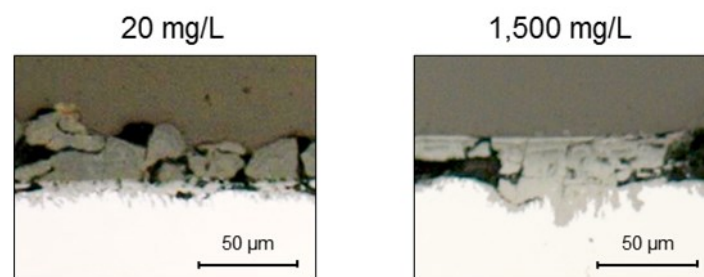


Figure 4.23 Cross section of 1.7218 coupons after 6 months of exposure at 175 °C in the artificial geothermal brine containing 20 mg/L (LHD-05) and 1,500 mg/L (SBY) chlorides

4.6 Investigation of crevice corrosion susceptibility

The susceptibility to crevice corrosion of 1.7218 was investigated using a rubber pad, imbedded on the electrode, to simulate an occluded area (Figure 3.7: B). The results of potentiodynamic polarization in the conditions with and without the simulated crevice were compared and shown in Figure 4.24 and Table 4.7. Similar shapes of the anodic and

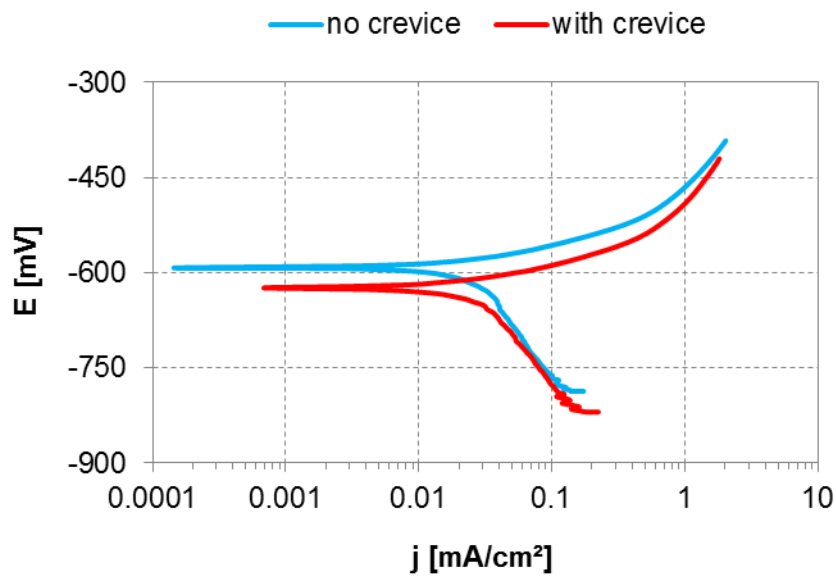


Figure 4.24 Typical cathodic and anodic polarization curves of 1.7218 with and without the crevice simulation in the artificial SBY geothermal brine at 100 °C

Table 4.7 Electrochemical data of 1.7218 determined from the polarization curves in the artificial SBY geothermal brine at 100 °C with and without the crevice simulation, respectively

	B_a [mV/dec]	B_c [mV/dec]	j_{corr} [mA/cm ²]	E_{corr} [mV]	CR [mm/y]
no crevice	62	317	0.0273	-593	0.32
with crevice	60	270	0.0270	-625	0.31

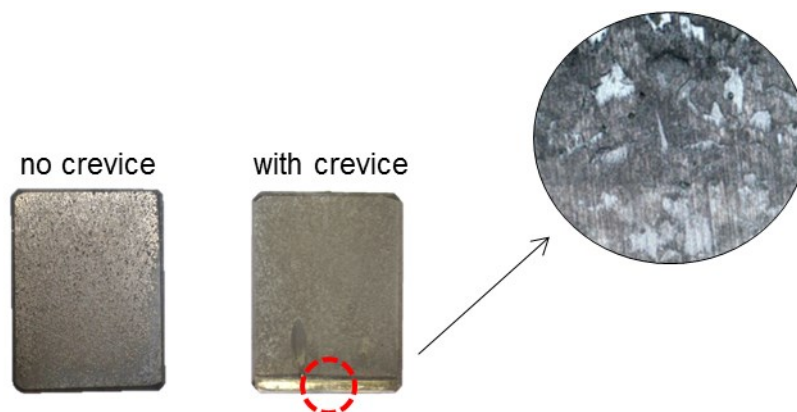


Figure 4.25 Appearance of 1.7218 electrode after the cyclic polarization in the artificial SBY geothermal brine at 100 °C with and without the crevice simulation, respectively

cathodic polarization curves in the system with and without the crevice suggested no difference in the mechanism of the corresponding reactions. Furthermore, the curves almost overlap each other, resulting in the similar corrosion rates. However, from the electrodes' appearance, depicted in Figure 4.25, narrow and shallow pits were present on the

electrode's surface where the crevice was simulated. Even though the pitting corrosion was a not common phenomenon on a low-alloyed steel surface due to the absence of a passive layer, it seems that the conditions present in the occluded area were favorable for a localized attack. Presumably, a stable iron (III) oxide and/or hydroxide layer formed on the surface while there was still enough oxygen present in the occluded area. Due to its heterogeneity and presence of active sites, imperfections, defects, etc., anions responsible for pitting corrosion adsorbed and initiated the formation of pits.

4.7 Investigation of stress corrosion cracking susceptibility

Susceptibility of low-alloyed steel 1.7218 to stress corrosion cracking (SCC) could not have been investigated using U-bend specimens (Figure 3.7: C) because the coupons cracked already during the bending. The stress produced on the coupons surface just before the crack, calculated with ANSYS Workbench Mechanical computer software, clearly exceeded the tensile strength of the material (Figure 4.26: A), causing a crack on the tension stretched surface to occur (Figure 4.26: B). Such behavior indicated to the hardness of the material, presumably due to the relatively high carbon content (> 0.2 wt%), causing it to break without significant deformation. Consequently, the material could be considered susceptible to mechanical cracking once the stress level exceeds the tensile strength of the material, even without any significant note of previous deformation. Susceptibility to stress corrosion cracking is, however, possible in case the preconditions for crack initiation are fulfilled; a mechanical factor (two-axis tension) and chemical (existence of aggressive ions in the solution that cause localized corrosion).

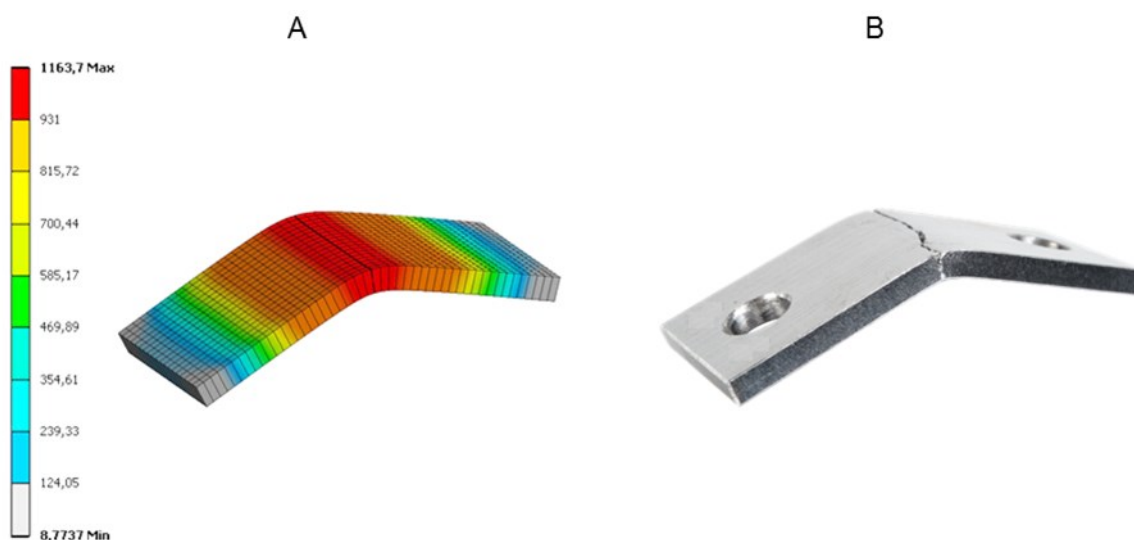


Figure 4.26 Calculated tensile stress in 1.7218 U-bend coupon just before the break point (A) and appearance of the broken coupon (B)

Chapter 5

Corrosion Resistance of Stainless Steel 1.4404

5.1 Introduction

In this chapter dependence of corrosion resistance of stainless steel grade 1.4404 on various factors was evaluated, as well as the alloy's susceptibility to crevice corrosion and stress corrosion cracking. The results were obtained by means of potentiostatic (electrochemical impedance spectroscopy) and potentiodynamic (cyclic polarization) electrochemical methods, and long-term exposure tests (up to 6 months). Tafel extrapolation method did not provide much sense in determining and predicting the corrosion rates of the alloy, due to the alloy's passive behavior observed in the investigated conditions.

5.2 Passive film growth

Passive films on stainless steels, containing mostly chromium (III) oxide, are formed instantaneously in the conditions where even only traces of oxygen are present. It is, therefore, assumed that prior to the immersion of the metal sample in the investigated conditions, the passive layer was already formed. The surface behavior of 1.4404 steel after the immersion in the artificial SBY geothermal brine was investigated by means for electrochemical methods and exposure tests at 100 °C as a function of time.

5.2.1 Short-term electrochemical methods

5.2.1.1 Open circuit potential monitoring

The change in the open circuit potentials (E_{oc}) of stainless steel 1.4404 during the 10 days of immersion in the artificial SBY geothermal brine at 100 °C is shown in Figure 5.1. Despite the initial drop of the potentials, the E_{oc} shifted toward anodic direction with time, indicating an ennoblement of the metal surface due to the, presumably, growth of the passive layer. However, interpretation of E_{oc} can sometimes be misleading. An increase of the E_{oc} could lead to the reduction of the passive range as well, and sooner onset of pitting corrosion. Therefore, additional methods were performed in order to establish the passivity range of the alloy and determine the critical potentials.

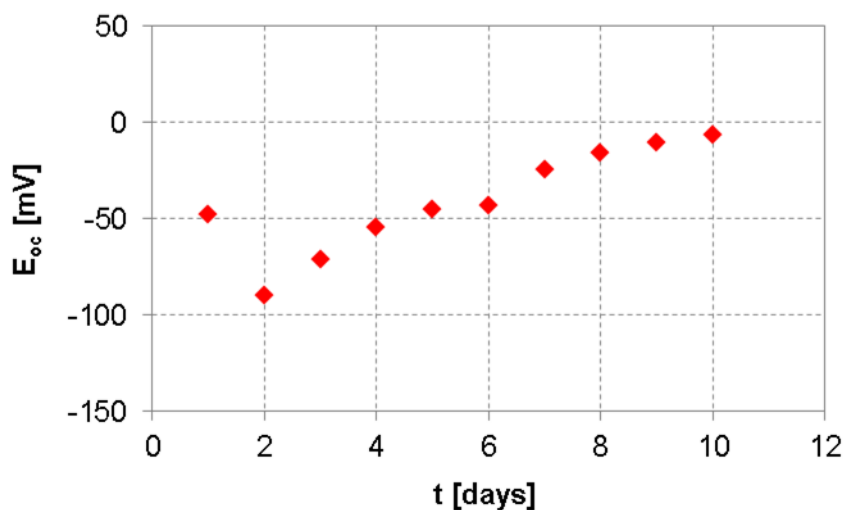


Figure 5.1 Monitoring of open circuit potential of 1.4404 steel in the artificial SBY geothermal brine at 100 °C during a 10-day immersion test

5.2.1.2 Electrode/solution interface characterization

Electrode/solution interface on the surface of 1.4404 steel was investigated using electrochemical impedance spectroscopy (EIS) during a 10-day period. Typical impedance spectra obtained throughout that time period are depicted in Figure 5.2. Nyquist spectra (Figure 5.2: A) resembled one distorted semi-circle irrespective of the immersion time, implying to the occurrence of one physical process on the metal/solution interface. The diameter of the semi-circle increased with time, what is a clear indication of the impedance increase. Such behavior was better perceived in the Bode modulus plot (Figure 5.2: B) in the low frequency (LF) domain.

According to the aforementioned observations, the investigated interface was modeled with an electrical equivalent model presented in Figure 3.1: A. The corresponding

data are given in Table 4.1. The results of the fit confirmed a non-ideal capacitive behavior of the interface. True capacitance values (C) calculated applying the Equation (3.1), were within the range characteristic for the double layer capacitance for each of the obtained spectra,

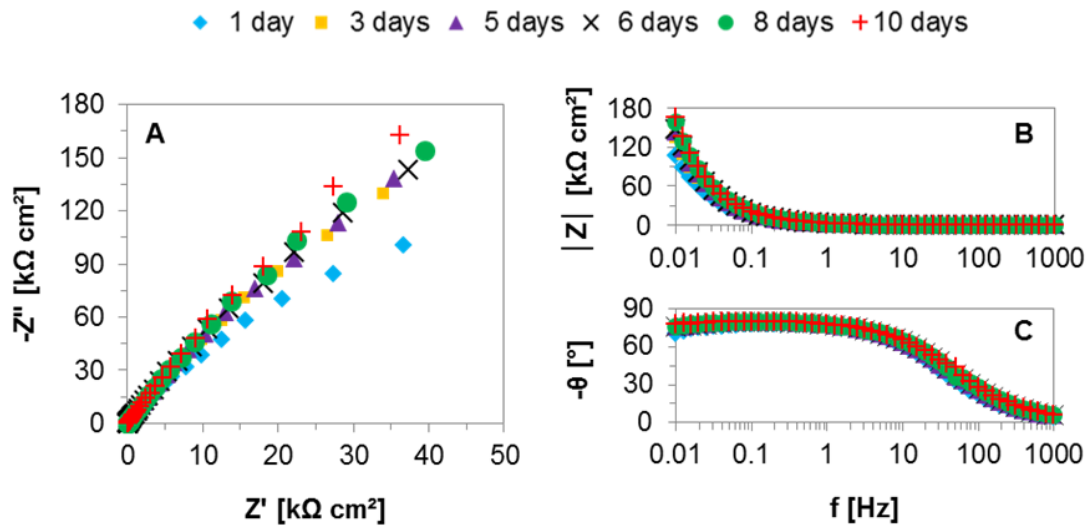


Figure 5.2 Typical impedance spectra for 1.4404 in the artificial SBY geothermal brine at 100 °C under E_{oc} conditions as a function of immersion time

Table 5.1 Electrochemical data obtained by EIS for 1.4404 during a 10-day immersion test in the artificial SBY geothermal brine at 100 °C under E_{oc} conditions

t [days]	R_s [Ω]	R [kΩ cm ²]	Q [μS s ^α /cm ²]	α	C [μF/cm ²]
1	10	844	102	0.872	51
2	10	2,005	92	0.875	46
3	10	3,369	87	0.876	43
4	10	4,609	84	0.876	42
5	10	3,942	81	0.877	40
6	10	4,374	78	0.876	38
7	10	4,489	75	0.877	37
8	10	6,817	74	0.876	36
9	10	12,112	72	0.876	35
10	10	n/a	71	0.876	34

proving that the observed phenomena was linked to the charge transfer. Consequently, resistance R was the charge transfer resistance, directly associated with the single kinetically controlled electrochemical reaction. Hence, it was possible to conclude that within the first 10 days of exposure the metal electrode exhibited direct increase in the resistance to the oxidation, i.e. corrosion reaction, presumably due to the formation of a passive layer on the

electrode surface. However, due to its extremely thin nature (in order of several nm), the passive film had a very short relaxation time. Hence, it was not observed experimentally in the applied frequency range.

5.2.1.3 Determination of critical potentials

In order to locate the change in the position of critical potentials, cyclic polarization was performed after 1 and 10 days of immersion. The recorded curves are presented in Figure 5.3, while the determined electrochemical data in Table 5.2. Similar width of the passive range was observed due to the shift of both E_{oc} and E_{pit} in the anodic direction. The ennoblement of E_{pit} implied to a delayed onset of pitting corrosion, which could be attributed in this case to an improvement of the protective characteristics of the passive layer formed on the electrode surface during 10 days of exposure. Furthermore, slightly lower passive current density was perceived after 10 days, contributing to the assumption of the formation of a more compact, thermodynamically stable passive layer.

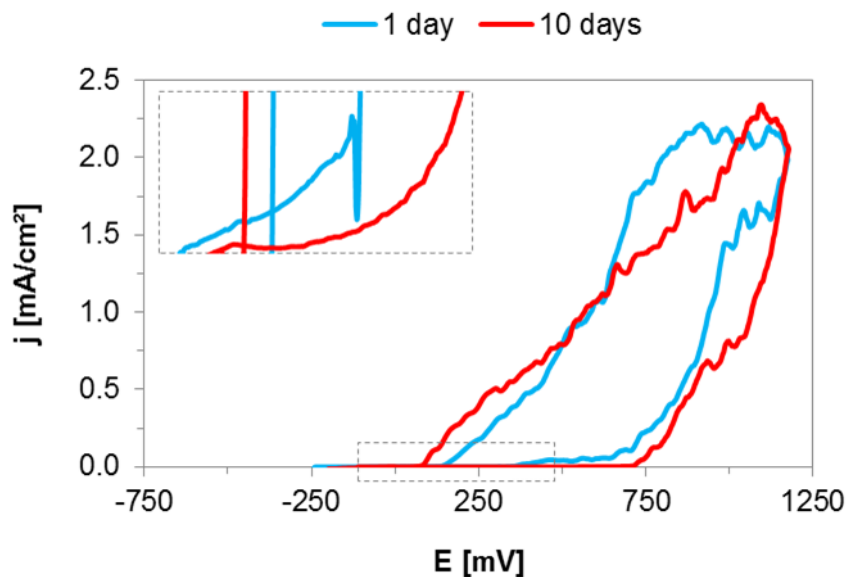


Figure 5.3 Typical cyclic polarization curves of 1.4404 after 1 and 10 days of immersion in the artificial SBY geothermal brine at 100 °C

Table 5.2 Electrochemical data of 1.4404 determined from the cyclic polarization curves after 1 and 10 days of immersion in the artificial SBY geothermal brine at 100 °C

t [days]	E_{oc} [mV]		E_{rep} [mV]			E_{pit} [mV]	
1	-50	-47	109	129	673	685	
10	-25	-11	98	107	774	762	

5.2.2 Long-term exposure tests

Long-term exposure tests were performed on 1.4404 coupons for 6 months in the artificial SBY geothermal brine at 100 °C. The appearance of the coupon is presented in Figure 5.4. The specimens retained a lustrous surface during the 6 months of exposure, exhibiting extremely low weight loss (< 0.0001 g) and showing, thus, an excellent resistance to uniform corrosion and the stability of the passive layer. Determination of the passive layer structure, as well as its thickness, was attempted by XRD. However, the surface analysis revealed only the bulk metal composition, indicating that the passive layer was thinner than ca. 10 nm. Furthermore, no signs of localized corrosion were observed on the coupons, only some microscopic impurities. These could, eventually, with further exposure time, present active sites for chloride adsorption and become the initiation sites for pitting corrosion.



Figure 5.4 Appearance of 1.4404 coupon after 6 months of exposure in the artificial SBY geothermal brine at 100 °C

5.3 Influence of temperature on corrosion performance

Temperature effect on the corrosion behavior of stainless steel 1.4404 was investigated in the artificial SBY geothermal brine at 70 °C, 100 °C and 175 °C.

5.3.1 Short-term electrochemical methods

5.3.1.1 Open circuit potential monitoring

After 20 h of immersion in the artificial SBY geothermal brine open circuit potentials (E_{oc}) of 1.4404 electrode surface were determined. The corresponding results are depicted in Figure 5.5. Increasing the temperature E_{oc} were consistently displaced in the cathodic direction. Such behavior suggests more active surface, resulting in a higher passive layer dissolution rates.

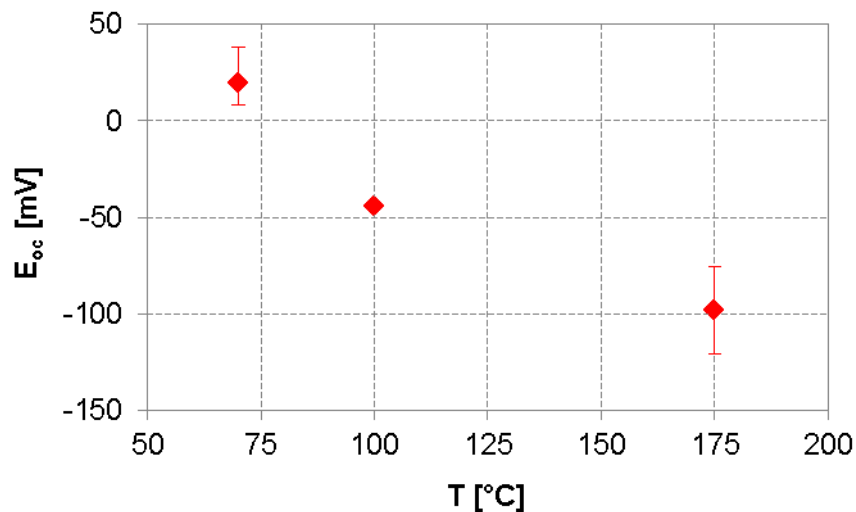


Figure 5.5 Open circuit potentials of 1.4404 steel in the artificial SBY geothermal brine at different temperatures

5.3.1.2 Electrode/solution interface characterization

Temperature influence on the electrode/solution interface, formed on 1.4404 steel surface under E_{oc} conditions, was studied by means of electrochemical impedance spectroscopy (EIS). The obtained spectra are presented in Figure 5.6. Nyquist representation of the impedance data (Figure 5.6: A) revealed the presence of one depressed capacitive semi-circle for each of the recorded spectra. Such observation pointed out to the existence of one relaxation time, i.e. one process occurring on the electrode surface (e.g. charge transfer, diffusion, adsorption, etc.). As the temperature increased, the diameter of the semi-circles decreased (Figure 5.6: A), which was a clear indication of the interface resistance reduction. Such behavior was better perceived in the Bode modulus plot in the low-frequency (LF) domain (Figure 5.6: B). Considering the shape of the impedance spectra, an increased depression of the semi-circles with temperature was apparent (Figure 5.6: A). This was also supported with the Bode phase angle plot (Figure 5.6: C), where the phase angle deviation from 90° (characteristic for an ideal capacitor) clearly increased with the temperature.

According to the visual observations, the studied interface was modeled using the equivalent electrical circuit model presented in Figure 3.1: A. The results of the fit are shown in Table 5.3. Considering that α values were always < 1 , deviation from an ideal capacitive behavior was confirmed. Furthermore, with temperature rise α values decreased, meaning; the surface roughness increased. True capacitance values (C) calculated according to the Equation (3.1), were within the range characteristic for a double layer capacitance, proving that the observed phenomena was linked to the charge transfer. Consequently, the resistance R was the charge transfer resistance, describing an

electrochemical reaction under the activation control. Considering its continuous decrease, one can conclude that with temperature increase from 70 °C to 175 °C the resistance to metal oxidation, i.e. corrosion, was reduced.

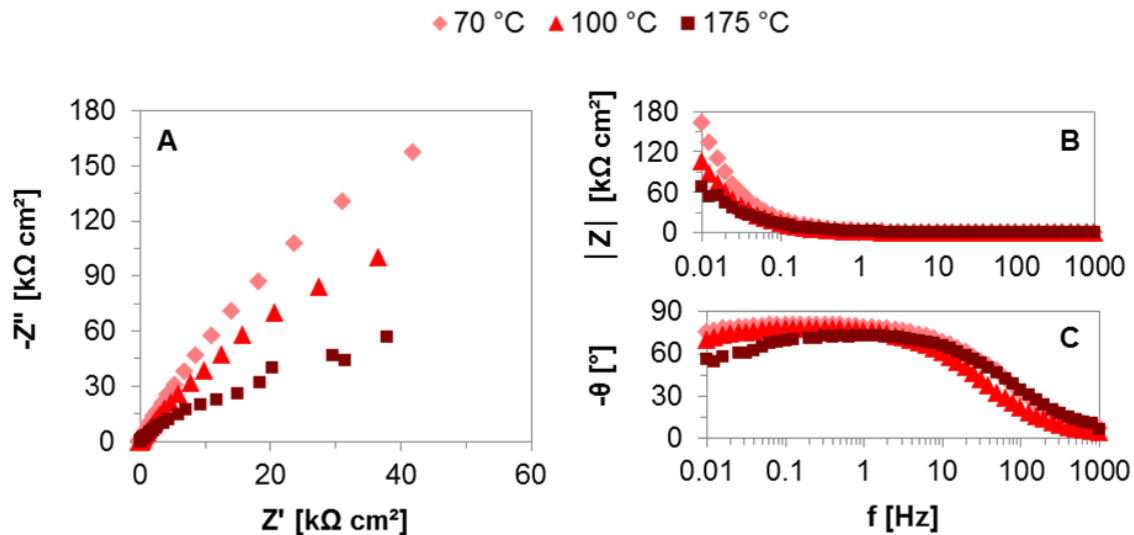


Figure 5.6 Typical impedance spectra for 1.4404 steel in the artificial SBY geothermal brine at different temperatures under E_{oc} conditions

Table 5.3 Electrochemical data obtained by EIS for 1.4404 in the artificial SBY geothermal brine under E_{oc} conditions at different temperatures

T [°C]	R_s [Ω]	R [kΩ cm ²]	Q [mS s ^α /cm ²]	α	C [μF/cm ²]
70	7	1,589	$7 \cdot 10^{-2}$	0.893	37
100	10	859	$1 \cdot 10^{-4}$	0.871	51
175	6	171	$1 \cdot 10^{-4}$	0.820	36

5.3.1.3 Determination of critical potentials and pits characterization

Typical cyclic polarization curves obtained for 1.4404 in the artificial SBY geothermal brine at the investigated temperatures is shown in Figure 5.7. The electrochemical data determined from the curves are presented in Table 5.4. Alloy 1.4404 exhibited passive behavior at all investigated temperatures. The passive currents were highest at 175 °C, which is in agreement with the Arrhenius law; an increase in the temperature will increase the kinetics of a reaction. In accordance, higher dissolution rates of the passive layer formed on the surface were expected. The widest passive range was observed at 100 °C indicated by the most positive pitting potentials. Such observation could be linked to the evolution of a passive layer with temperature increase from 70 °C to 100 °C due to the higher diffusion rates of chromium from the bulk metal toward the surface¹⁷⁵ and

the formation of protective chromium (III) layer. Increasing the temperature up to 175 °C, the curve shifted to more active direction, implying to a stronger temperature effect on the chloride chemisorption on the metal surface causing an easier passive film breakdown, rather than the layer improvement. The substantially narrower passive range showed the electrodes susceptibility to pitting corrosion already at potentials very close to E_{oc} . Considering that the E_{oc} were located between the repassivation and pitting potentials, metastable pitting was possible to occur. Moreover, this also suggested the alloy's poor capability to repassivate in normal stagnant service conditions.

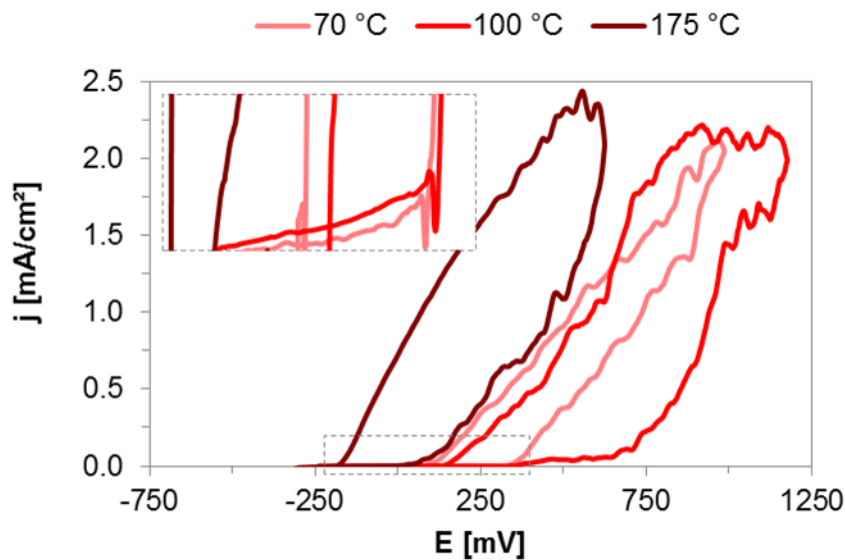


Figure 5.7 Typical cyclic polarization curves of 1.4404 in the artificial SBY geothermal brine at different temperatures

Table 5.4 Electrochemical data of 1.4404 determined from the cyclic polarization curves in the artificial SBY geothermal brine at different temperatures

T [°C]	E_{oc} [mV]		E_{rep} [mV]		E_{pit} [mV]	
70	5	39	124	155	369	415
100	-50	-47	109	129	673	685
175	-120	-72	-165	-146	134	337

On the backward scan of each of the recorded curves, a lagging of the current densities with potential was apparent, commonly known as hysteresis. Such observation is a sign of surface perturbation due to the anodic polarization. Consequently, one can conclude a much milder surface distortion at 70 °C compared to the higher temperatures, which was supported by the surface analysis of the electrodes after the anodic polarization (Figure 5.8 and Figure 5.9).

Surface analysis of the polarized electrodes revealed the presence of the surface discoloration. This phenomenon commonly occurs on stainless steels due to the passive film destabilization. It is linked to the formation of various types of ferric oxides and/or hydroxides of different thickness and color, which interfere with each other and cause surface discoloration.^{180,181} Due to the increased dissolution rates of the passive film with temperature, surface discoloration was mostly pronounced at 175 °C.

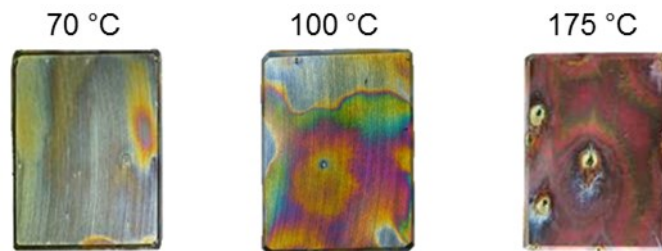


Figure 5.8 Appearance of 1.4404 electrodes after cyclic polarization in the artificial SBY geothermal brine at different temperatures

Beside the surface discoloration, pitting corrosion was present on the electrodes surface in all investigated conditions as well. The highest amount of pits was observed at 70 °C (Table 5.2, Figure 5.4), whilst the lowest at 100 °C. Furthermore, the deepest pits were formed in the latter conditions. Such findings could be linked to the evolution and improvement in thickness and crystallinity of the passive layer with temperature, leading to fewer imperfections present in its structure and thus, lower amount of formed pits at higher temperatures. Moreover, the oxygen solubility in the solution is significantly reduced at 100 °C, resulting in a decreased capability of a passive layer self-repair and thus, more concentrated localized attack. The highest pits width-to-depth ratio was observed at 175 °C (Figure 5.4), suggesting preferential dissolution of pits walls over the bottoms with temperature increase. Presumably, the passive layer improvement with temperature and

Table 5.5 Characterization of the pits observed on 1.4404 electrode surface in the artificial SBY geothermal brine at different temperatures

T [°C]	no. of pits / cm ²	width [μm]			depth [μm]		
70	3	257	±	117	234	±	38
100	1	367	±	177	280	±	104
175	1	381	±	278	143	±	40

sufficient oxygen concentration in the solution counterbalanced the higher adsorption and diffusion rates of the aggressive anions on the active sites. Hence, faster repassivation of the attacked sites occurred, resulting in a smaller pit depth.

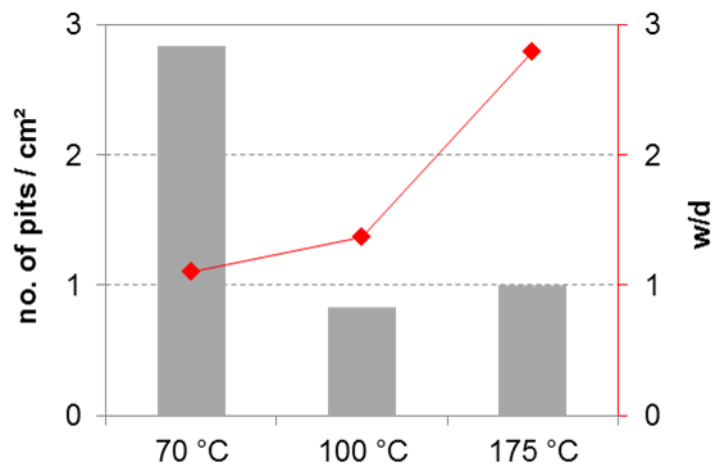


Figure 5.9 Amount and average width-to-depth ratio of the pits observed on 1.4404 after cyclic polarization in the artificial SBY geothermal brine at different temperatures

5.3.2 Long-term exposure tests

Square coupons of stainless steel 1.4404 were exposed to the artificial SBY geothermal brine for 1, 3 and 6 months at 100 °C and 175 °C. Due to the extremely low coupons' weight loss (< 0.0001 g) during the whole exposure time, the uniform corrosion rate was considered to be < 0.06 $\mu\text{m}/\text{y}$ at both investigated temperatures. Such finding proved a thermodynamically stable passive layer formation, resulting in excellent resistance of 1.4404 steel to uniform corrosion.

Surface analysis of the exposed coupons using an optical microscope revealed hardly any signs of corrosion attack (Figure 5.10 and Figure 5.11). The coupons surface remained lustrous at both investigated temperatures, suggesting the formation of an extremely thin and protective passive layer. However, light deposits were found on the surface at 175 °C, which could eventually, with further exposure time, result in a passive film breakdown. An indication of the crevice corrosion was present at the place of coupon fixation at 175 °C. Nevertheless, during the 6 months of exposure alloy 1.4404 exhibited an excellent uniform and pitting corrosion resistance.

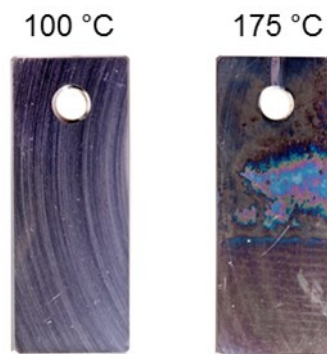


Figure 5.10 Appearance of 1.4404 coupons after 6 months of exposure in the artificial SBY geothermal brine at 100 °C and 175 °C, respectively

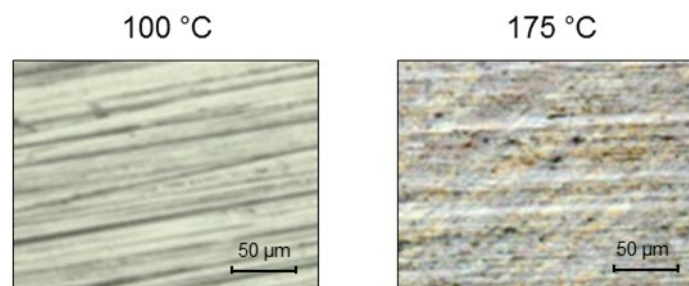


Figure 5.11 Surface of 1.4404 coupons after 6 months of exposure in the artificial SBY geothermal brine at 100 °C and 175 °C, respectively

5.4 Influence of acidity on corrosion performance

Influence of the solution acidity on the behavior of 1.4404 was investigated at 175 °C in the artificial geothermal brine pH 2 (LHD-23) and pH 4 (SBY), respectively.

5.4.1 Short-term electrochemical methods

5.4.1.1 Open circuit potential monitoring

After 20 h of immersion in the artificial geothermal brines open circuit potentials (E_{oc}) of 1.4404 were determined. The obtained results are shown in Figure 5.12. Slightly more positive E_{oc} were observed in the pH 2 conditions, suggesting lower surface activity. Additional testing methods were performed in order to study the alloy's performance in more detail.

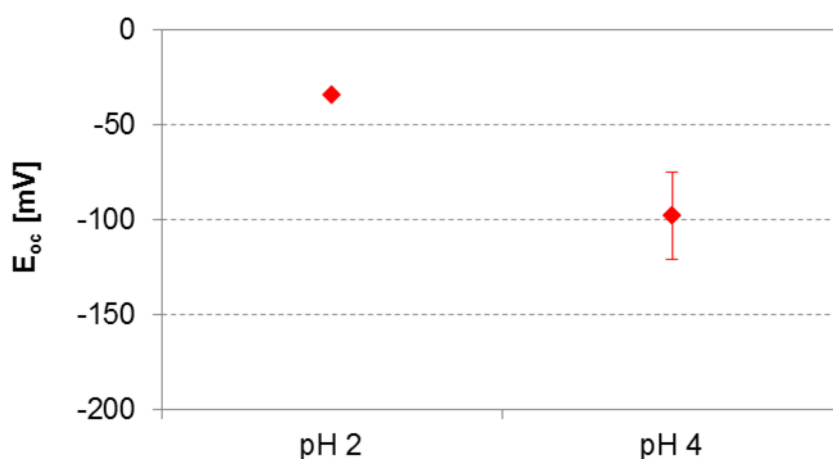


Figure 5.12 Open circuit potentials for 1.4404 after 20 h of immersion at 175 °C in the artificial geothermal brine pH 2 (LHD-23) and pH 4 (SBY), respectively

5.4.1.2 Electrode/solution interface characterization

Electrode/solution interface, evolved in the solutions of different acidity on 1.4404 steel surface, was characterized using electrochemical impedance spectroscopy (EIS). The obtained impedance spectra are depicted in Figure 5.13. Nyquist representation of the impedance data (Figure 5.13: A and B) revealed a substantial difference in the metal/solution interface behavior in the conditions with different acidity. In the less acidic solution only one depressed semi-circle was present in the applied frequency range, suggesting an occurrence of one process on the electrochemical electrode/solution interface (e.g. charge transfer, diffusion, adsorption, etc.). On the other hand, in the more acidic solution two time constants were clearly resolved in the obtained impedance spectrum, indicating the existence of two processes on the electrode surface. In both high- (HF) and low-frequency (LF) domains the semi-circles exhibited a non-ideal capacitive behavior (Figure 5.13: D). Due to their overlapping (at approximately 1 Hz) it was assumed that the processes occurred simultaneously. Increasing the solution acidity, the reduction in the resistance was noticeable from the zoomed-in portion of the Nyquist plot (Figure 5.13: B) and HF region of the Bode modulus plot (Figure 5.13: C). Such behavior was completely understandable considering an increase in the hydrogen ion concentration and thus, the solution conductivity. Furthermore, a substantial reduction in the interface impedance was clearly seen from the diameters of the semi-circles (Figure 5.13: A) and LF region of the Bode modulus plot (Figure 5.13: C). It was, therefore, expected that the dissolution rates of the passive layer and/or electrode surface would be significantly higher in the solution pH 2.

Taking into consideration the visual observations, the obtained impedance spectra in the solution pH 2 and pH 4 were modelled using the equivalent electrical circuits

presented in Figure 3.1: B and A, respectively. The corresponding data are shown in Table 5.6. A non-ideal capacitive behavior was confirmed considering α values were < 1 . Lower α in the solution pH 2 implied to a rougher surface compared to the solution pH 4. Such finding was the main cause for the heterogeneous distribution of the time constants and it supported the CPE behavior. Furthermore, greater surface heterogeneity in pH 2 solution resulted in higher true capacitance values (C) calculated according to Equation (3.1) from the corresponding Q , compared to the capacitance in the less acidic conditions. The layer formed on the electrode surface in the solution pH 4 could have been linked to a double layer capacitance due to its value being within the double layer characteristic range.

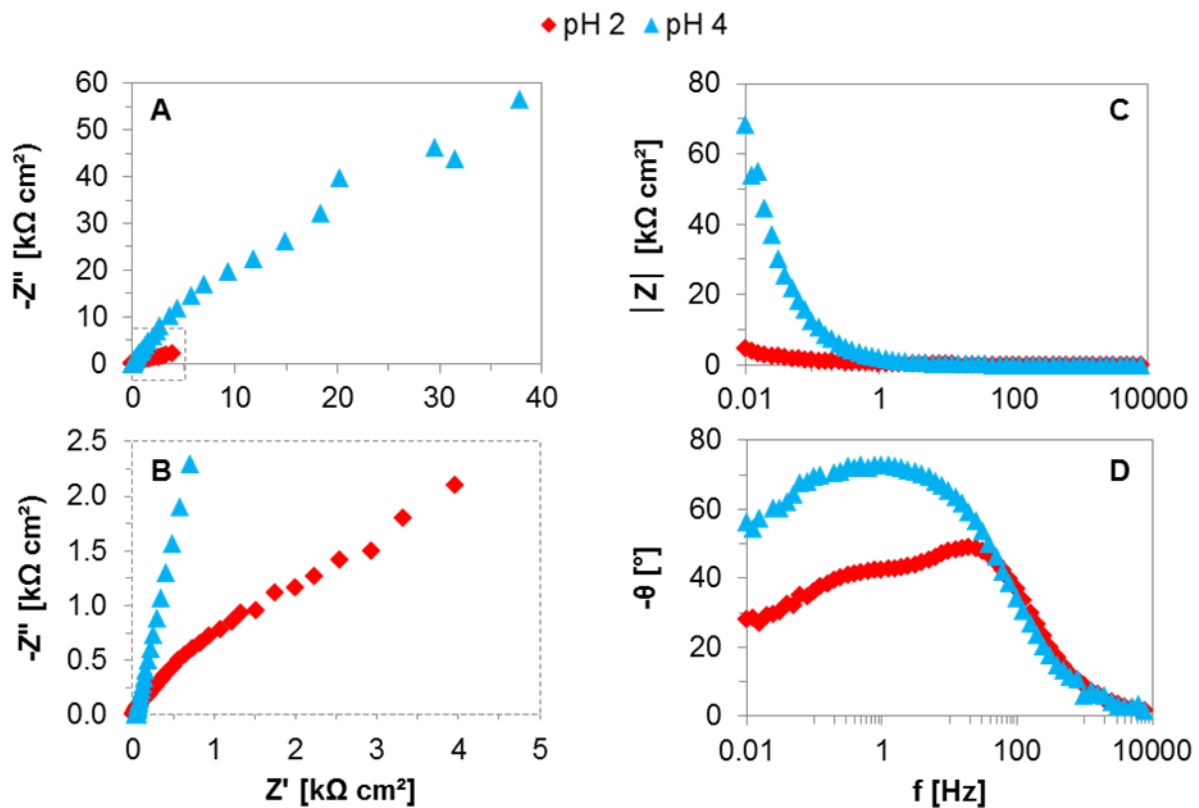


Figure 5.13 Typical impedance spectra for 1.4404 at 175 °C under E_{oc} conditions in the artificial geothermal brine pH 2 (LHD-23) and pH 4 (SBY), respectively

Consequently, the phenomenon that occurred on the electrode/solution interface could be attributed to the charge transfer, and the corresponding resistance R_1 to the charge transfer resistance, directly associated with a single kinetically controlled electrochemical reaction. On contrary, the capacitances of the layers formed in the more acidic conditions couldn't be linked to the double layer and it was, therefore, impossible to compare the corrosion behavior of the material in the investigated conditions. However, it was perceived that the corrosion film formed on the surface of the electrode exposed in the more acidic conditions consisted of two different layers; the thicker, porous inner layer and the thinner, outer layer. Such

observation could be attributed to the higher dissolution rates of the electrode surface in the latter conditions, causing the corrosion product film on the electrode to grow and, consequently, greater relaxation times that contributed to the experimental detection of the layers.

Table 5.6 Electrochemical data obtained by EIS for 1.4404 at 175 °C under E_{oc} conditions in the artificial geothermal brine pH 2 (LHD 23) and pH 4 (SBY), respectively

pH	R_s [Ω]	R_1 [$k\Omega\text{ cm}^2$]	Q_1 [$mS\text{ s}^{\alpha_1}/\text{cm}^2$]	α_1	C_1 [$\mu F/\text{cm}^2$]	R_2 [$k\Omega\text{ cm}^2$]	Q_2 [$mS\text{ s}^{\alpha_2}/\text{cm}^2$]	α_2	C_2 [$\mu F/\text{cm}^2$]
2	2.8	0.1	1.1	0.712	242	1.8	7.0	0.677	2,960
4	5.7	171.3	0.1	0.820	36	-	-	-	-

5.4.1.3 Determination of critical potentials and pits characterization

Typical cyclic polarization curves for 1.4404 recorded at 175 °C in the artificial geothermal brine pH 2 (LHD-23) and pH 4 (SBY), respectively, are depicted in Figure 5.14. The electrochemical data determined from the curves are shown in Table 5.7. Increasing the solution acidity, the surface of the examined electrodes exhibited an active-passive transition in the applied potential range. Since the corresponding E_{oc} were more positive than the potential at which this behavior was observed (approximately -220 mV), the metal was considered passive in normal conditions. Polarizing the surface further in the anodic direction, the passive layer formed instantly, indicated by the current sudden drop to appreciably low values. The current stagnated over a wide passive range, until the pitting potential were reached. Comparing the passive current densities, higher values were observed in the more acidic solution, implying to the higher passive layer dissolution rates. This was caused most probably due to the abundance of hydrogen ion, which is the main oxidizer in high acidic conditions that drives the cathodic reaction and thereby, stimulates the anodic dissolution of the electrode surface.

The pitting potentials shifted in the anodic direction as the solution acidity increased. Such observation is in contradiction with a numerous literature that deals with this topic,^{42,43,182-184} which states that hydrogen decreases the stability of passive films, increases the number of active sites and thus, promotes pitting initiation and accelerates pitting growth. The controversial effect could be ascribed to the increased concentration of the sulphates present in the LHD-23 solution. Increasing the sulphate-to-chloride ratio, a competitive adsorption of the two aggressive anions on active sites occurs, as suggested by different authors.¹⁸⁵⁻¹⁸⁷ Since the sulphate anions are bigger than the chlorides, their diffusion rate through the passive film is slower and are, therefore, considered less aggressive. Once they adsorb on active sites of an electrode surface, their inhibitive effect on pitting corrosion

prevails, despite the corrosion rate enhancement. Due to the blocked ingress of the more aggressive chloride ions, the pit formation is delayed. However, once the pitting corrosion onsets, the growth rate of the pits and/or their amount is much higher than in the solution containing less sulphate, as suggested by the higher slope of the polarization curve on the forward scan.

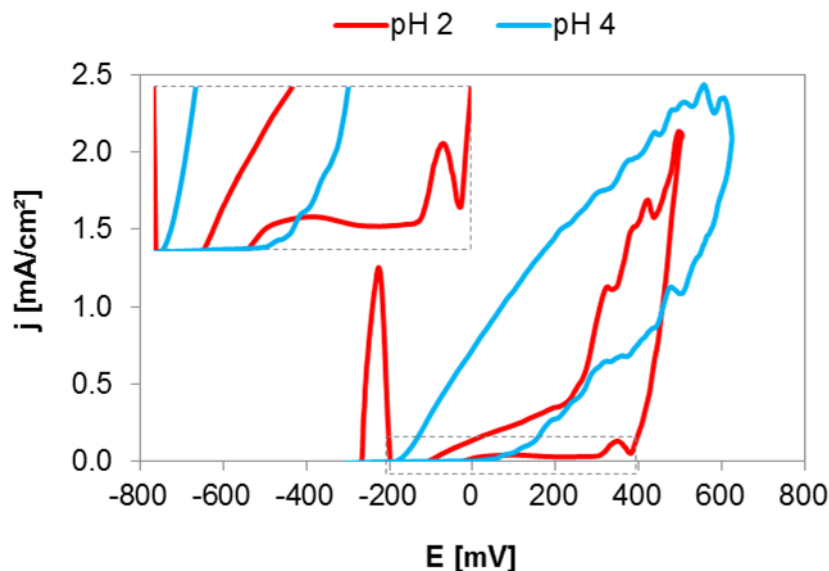


Figure 5.14 Typical cyclic polarization curve of 1.4404 at 175 °C in the solution pH 2 (LHD-23) and pH 4 (SBY), respectively

Table 5.7 Electrochemical data of 1.4404 determined from the cyclic polarization at 175 °C in the solution pH 2 (LHD-23) and pH 4 (SBY), respectively

pH	E_{oc} [mV]		E_{rep} [mV]			E_{pit} [mV]	
2	-48	-43	-45	23	301	390	
4	-120	-72	-165	-146	134	337	

Reversing the scan in the cathodic direction, negative hysteresis in both conditions was apparent. It was more pronounced in the solution with higher pH, resulting in the slower “healing” of the disturbed surface, i.e. slower repassivation of the attacked sites. Although such behavior controverted the expected, it was assumed that the reason laid in the width-to-depth ratio of the pits observed on the electrode surface. This observation is addressed in the further text below.

Different appearance was observed on the electrodes surface after the cyclic polarization tests (Figure 5.15). In the less acidic conditions, an appreciable surface discoloration and several pits were present. On the other hand, in the more acidic solution

the lustrous surface was still persistent, but with a greater amount of pits on the electrode surface. Due to the lower pH and hence, higher dissolution rates, ferric compounds were not stable in the latter conditions. Since they are assumed to be the main reason for causing such phenomenon to occur, surface discoloration in the more acidic solution was not observed. However, according to the amount and size of the pits on the surface, shown in Table 5.5, pitting corrosion was more pronounced. This was clear already from the cyclic polarization curves (Figure 5.10) in the curves slope difference once the pitting potential was reached. In both conditions the pits were visible to the naked eye, indicating rather wide and deep pits. Their number and size increased with an increase in the solution acidity (Table 5.5), confirming again more severe pitting corrosion in the solution with lower pH.

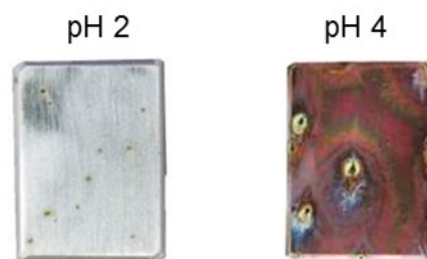


Figure 5.15 Appearance of 1.4404 electrodes after the cyclic polarization test at 175 °C in the solution pH 2 (LHD-23) and pH 4 (SBY), respectively

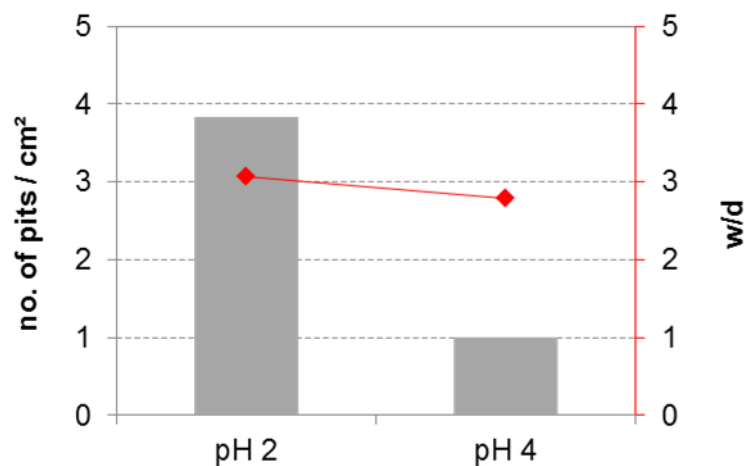


Figure 5.16 Amount and average width-to-depth ratio of the pits observed on 1.4404 after cyclic polarization in the solution pH 2 (LHD-23) and pH 4 (SBY) at 175 °C, respectively

Considering the pits width-to-depth ratio increase with the solution pH decrease, shown in Figure 5.11, it seemed that the increase in the solution acidity promoted the increase in the pit width over the pit depth. This could be a reasonable explanation of the slower surface repassivation in the solution with lower acidity, indicated by the wider negative

hysteresis; reversing the potential in the cathodic direction, the passive film tended to recover on the electrode surface, as well as inside the pits, but only in the presence of oxygen. Since the pits formed in the brine pH 4 were narrower, oxygen diffusion inside the pits was impaired and the passive film reformation was slowed down.

Table 5.8 Characterization of the pits observed on 1.4404 electrode surface after the cyclic polarization test in the solution pH 2 (LHD-23) and pH 4 (SBY) at 175 °C, respectively

pH	no. of pits / cm ²	width [μm]	depth [μm]
2	4	437 ± 292	158 ± 88
4	1	381 ± 278	143 ± 40

5.4.2 Long-term exposure tests

Stainless steel 1.4404 coupons were exposed for different time periods at 175 °C to the artificial brine pH 2 and pH 4, respectively. In the less acidic conditions, the mass loss of the coupons was immeasurable using an analytical scale precision 10⁻⁴ g, meaning the corrosion rates were < 0.06 μm/y. This could be attributed to the formed chromium (III) passive layer that provided an excellent resistance to uniform corrosion. However, in the more acidic solution, the passive film disruption was clearly evident (Figure 5.18: A), suggesting high metal dissolution rates. The calculated corrosion rate reached 0.3 mm/y during the first month of exposure (Figure 5.17). With the subsequent exposure time, the rate was reduced, presumably due to the formation of an adherent, tenacious corrosion layer.

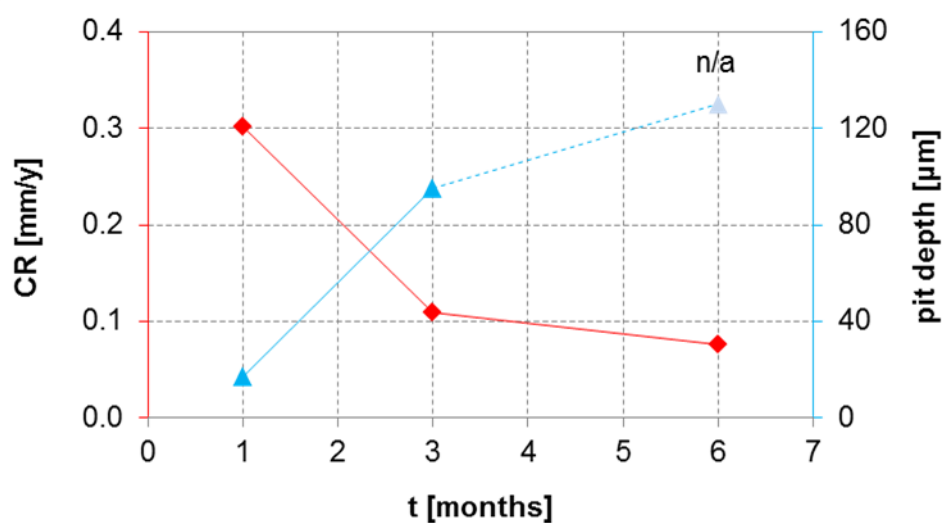


Figure 5.17 Calculated corrosion rates and measured pits depth of 1.4404 after exposure in the artificial geothermal brine pH 2 (LHD-23) at 175 °C

Analyzing the surface of the coupons after 6 months of exposure, no signs of corrosion attack were noticed on the coupons surface exposed in the less acidic conditions using an optical microscope (Figure 5.18: B). However, in the solution pH 2 the surface was severely disturbed after 6 months of exposure, indicated by the grain boundaries visibility (Figure 5.18: A and Figure 5.19: A). Numerous pits, observed on the surface after 6 months of exposure, indicated to the passive layer breakdown and alloy's susceptibility to pitting corrosion. However, cross section analysis showed no signs of pits propagation into the metal matrix (Figure 5.19: B), meaning only shallow pitting occurred on the material surface. Due to the high density of the formed shallow pits, it was hard to distinguish general metal dissolution from the localized attack, implying to an extremely intensive corrosion. It was interesting to note that the depth of the formed pits increased with exposure time, despite the reduction of the corrosion rate (Figure 5.17). Such finding clearly corroborates already known fact; weight loss method is not a reliable method in determining the corrosion rate of the materials subject to localized corrosion. Nevertheless, the solution pH 2 clearly caused higher uniform dissolution rates, confirming significantly lower resistance of the passive layer formed on the surface in the latter conditions, obtained by EIS.

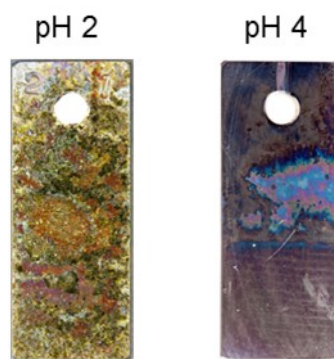


Figure 5.18 Appearance of 1.4404 coupons after 6 months of exposure in the artificial geothermal brine pH 2 (LHD-23) and pH 4 (SBY), respectively

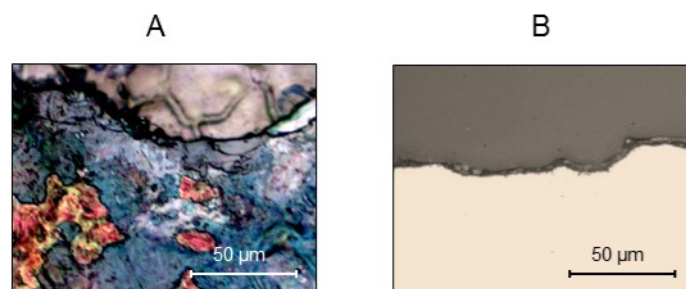


Figure 5.19 Surface (A) and cross section (B) of 1.4404 coupons after 6 months of exposure in the artificial geothermal brine pH 2 (LHD-23)

5.5 Influence of salt concentration on corrosion performance

Effect of an increased salt concentration on the corrosion behavior of stainless steel 1.4404 was investigated at 175 °C in the artificial geothermal brine containing 20 mg/L (LHD-05) and 1,500 mg/L (SBY) chlorides.

5.5.1 Short-term electrochemical methods

5.5.1.1 Open circuit potential monitoring

Open circuit potentials (E_{oc}) of 1.4404 electrodes after 20 h of immersion in the artificial geothermal brine containing 20 mg/L (LHD-05) and 1,500 mg/L (SBY) chlorides, respectively, are shown in Figure 5.20. Significant displacement of E_{oc} in the cathodic direction was apparent in the solution with higher chloride concentration. This suggested more active surface and therefore, higher corrosion rates. In order to obtain more detailed insight into the corrosion behavior of 1.4404 alloy, additional electrochemical tests were performed.

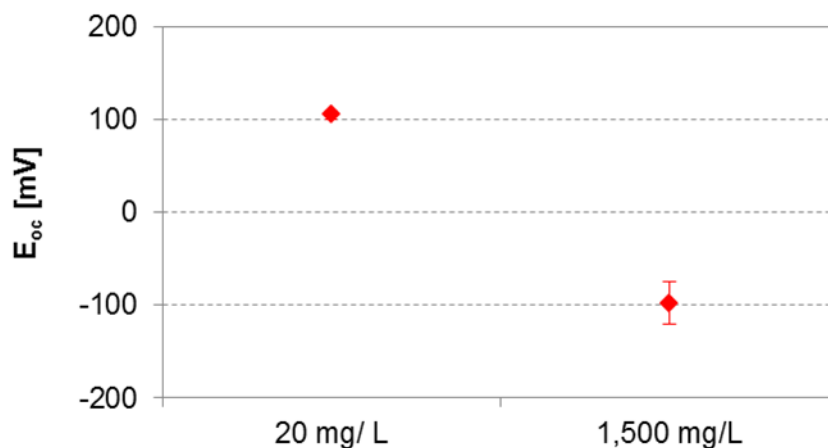


Figure 5.20 Open circuit potentials of 1.4404 after 20 h of immersion at 175 °C in the artificial geothermal brine containing 20 mg/L (LHD-05) and 1,500 mg/L (SBY) chlorides

5.5.1.2 Electrode/solution interface characterization

Characterization of the electrode/solution interface of 1.4404 surface in the solution with different salt concentration was performed by means of electrochemical impedance spectroscopy (EIS). The obtained spectra are depicted in Figure 5.21. Nyquist representation of the impedance data (Figure 5.21: A) showed one distorted semi-circle over the majority of the applied frequency range irrespective of the solution concentration. However, zooming in the portion of the spectra at high-frequency (HF) domain, a second time constant was revealed in the solution containing less chloride (Figure 5.21: B). The first

semi-circle was overlapped by the second one that gave rise already at approximately 2 Hz. This suggested a simultaneous occurrence of two processes on the electrode/solution interface (e.g. charge transfer, diffusion, adsorption, etc.), first one having a very short relaxation time. Increasing the chloride concentration, solution resistance was significantly reduced (Figure 5.21: A, B and C). Such behavior was reasonable considering that with an increased salt concentration more ions are present in the brine, resulting in a more conductive, i.e. less resistive solution. However, the system's impedance tended to increase with the chlorides content, suggested by the increase in the semi-circle diameter (Figure 5.21: A). Such observation was better perceived in the LF domain of the Bode modulus plot (Figure 5.21: C) that showed an improvement in the impedance of the interface exposed to the solution containing 1,500 mg/L chlorides.

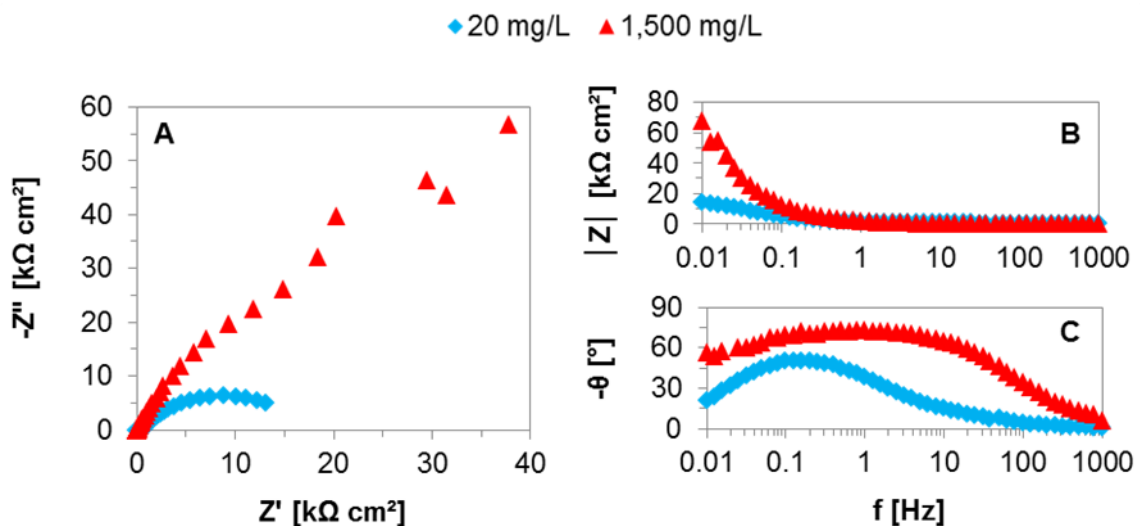


Figure 5.21 Typical impedance spectra for 1.4404 at 175 °C under E_{oc} conditions in the artificial geothermal brine containing 20 mg/L (LHD-05) and 1,500 mg/L (SBY) chlorides

According to the observed, interface of the systems exposed to the solution containing 20 mg/L and 1,500 mg/L chloride was modelled using the equivalent electrical circuits presented in Figure 3.1: B and A, respectively. The fit results are shown in Table 5.9. As suggested by α values < 1 , the corresponding interfaces behaved as non-ideal, i.e. leaking capacitors. Calculated according to Equation (3.1), true capacitance values (C) were in all cases within the range characteristic for a double layer capacitance, proving that the phenomena that occurred on the electrode/solution interface could be linked to the charge transfer. However, one of the two layers, presumably the outer one, present on the electrode surface exposed in the less concentrated solution was a passive layer. In the more concentrated solution the passive layer was probably not as evolved and its relaxation time was, therefore, too short to be detected. Nevertheless, the charge transfer resistance R_1 of

the double layer was higher in the more concentrated solution, indicating lower electrode dissolution rates in the current conditions. This clearly corroborates the results obtained by cyclic polarization method and could be attributed to the lower oxygen content. Owing the fact that the oxygen was the main oxidant in the investigated conditions that drove the cathodic reduction reaction, its lower content undoubtedly impeded the metal electrode general dissolution rate.

Table 5.9 Electrochemical data obtained by EIS for 1.4404 at 175 °C under E_{oc} in the artificial geothermal brine containing 20 mg/L (LHD-05) and 1,500 mg/L (SBY) chlorides

$c(\text{Cl}^-)$ [mg/L]	R_s [Ω]	R_1 [$k\Omega \text{ cm}^2$]	Q_1 [$\text{mS s}^{\alpha_1}/\text{cm}^2$]	α_1	C_1 [$\mu\text{F}/\text{cm}^2$]	R_2 [$k\Omega \text{ cm}^2$]	Q_2 [$\text{mS s}^{\alpha_2}/\text{cm}^2$]	α_2	C_2 [$\mu\text{F}/\text{cm}^2$]
20	67	0.5	0.12	0.794	50	17	0.16	0.785	81
1,500	6	171.3	0.11	0.820	36	-	-	-	-

5.5.1.3 Determination of critical potentials and pits characterization

Typical cyclic polarization curves obtained for 1.4404 in the artificial geothermal brine containing 20 mg/L (LHD-05) and 1,500 mg/L (SBY) chlorides, respectively, are presented in Figure 5.22. The electrochemical data determined from the curves are shown in Table 5.10. Anodically polarizing the electrodes, passive behavior in both conditions was apparent. Lower passive currents were observed in the solution containing more chlorides, indicating to the lower dissolution rates of the passive layer and/or electrode surface. This could be explained with the effect of “salting out”;¹⁷⁷⁻¹⁷⁹ due to the presence of more ionic species in the SBY solution, the affinity of the non-polar oxygen molecules to the polar water was decreased, resulting in decreased oxygen solubility in the solution. Since the oxygen reduction was one of the main cathodic reactions in the investigated conditions, lower oxygen content led to lower cathodic reaction rates and hence, the anodic dissolution rates in the solution containing 1,500 mg/L chlorides were reduced.

On the forward scan of the polarization curve in the less concentrated solution a small current hump was observed at the potential approximately 350 mV. First, it was assumed to occur due to the surface disruption and formation of a metastable pit, but the relatively large length of the hump and its presence always at the same potential, implied to the certain chemical reaction. After examining the redox potentials of the species present in the metal composition and the brine, oxidation of ferrous to ferric ion seemed the most reasonable explanation for the observed effect.

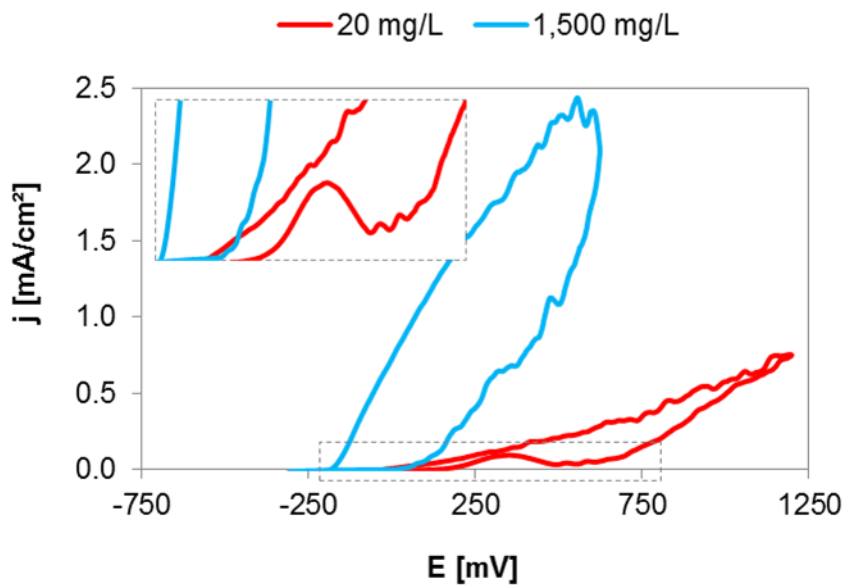


Figure 5.22 Typical cyclic polarization curve of 1.4404 at 175 °C in the artificial geothermal brine containing 20 mg/L (LHD-05) and 1,500 mg/L (SBY) chlorides, respectively

Table 5.10 Electrochemical data of 1.4404 determined from cyclic polarization at 175 °C in the solution containing 20 mg/L (LHD-05) and 1,500 mg/L (SBY) chlorides

$c(\text{Cl}^-)$ [mg/L]	E_{oc} [mV]		E_{rep} [mV]			E_{pit} [mV]	
20	100	– 111	152	– 364	706	– 749	
1,500	-120	– -72	-165	– -146	134	– 337	

The electrode surface was passive over a larger potential range in the solution containing less chloride. The reason were nobler E_{pit} , resulting in a delayed onset of the pitting corrosion. The amount and/or growth of the pits were certainly more pronounced in the solution with higher chloride concentration. This could be concluded by the steeper polarization curve once the E_{pit} were reached, and the wider negative hysteresis observed on the backward scan. All of these facts implied to a more substantial disturbance of the electrode surface in the solution containing higher chloride content. Accordingly, one can conclude that the higher amount of chlorides in the SBY artificial brine was responsible for the earlier onset of the pitting corrosion and more substantial surface disturbance. Proposed mechanism could be the following: higher chloride concentration in the solution led to an increased chloride adsorption on the active sites. Subsequently, diffusion rates through the passive film were increased, resulting in an earlier passive film breakdown.

In the solution with higher chloride content the E_{rep} were more negative than the observed E_{oc} . This implied to the possibility of metastable pits formation even during the

normal stagnant service conditions. Furthermore, once the stable pit growth was initiated, poor repassivation ability of the surface is expected. Conversely, in the brine containing 20 mg/L chlorides, the E_{rep} were more positive than the corresponding E_{oc} , resulting in a sooner capability of the passive film self-repassivation after the breakdown, caused during the anodic polarization.

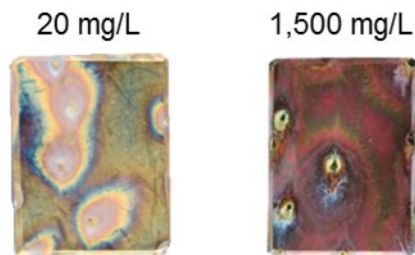


Figure 5.23 Appearance of 1.4404 electrodes after the cyclic polarization test at 175 °C in the artificial geothermal brine containing 20 mg/L (LHD-05) and 1,500 mg/L (SBY) chlorides

Surface discoloration was present on 1.4404 electrodes in both investigated conditions. It was more pronounced in the solution containing higher chloride concentration, presumably due to the higher current densities during the polarization scan. Characterizing the pits formed on electrodes surface in the investigated conditions (Table 5.11), wider and deeper pits were observed in the solution containing higher chloride concentration. This clearly corroborated the formerly made conclusions based on the hysteresis of the polarization curves on the backward scan, about the severity of the electrode surface disruption. However, the amount of pits was lower in the solution containing more chloride (Figure 5.24). Such finding suggested concentrated localized attack, presumably due to the greater chloride driving force to the inside of the formed pit than to the adsorption on new active sites. Furthermore, an increase in the pit width-to-depth ratio with chloride concentration (Figure 5.24) implied to the preferential dissolution of the pits walls over the pits bottoms. A reasonable explanation could be the impaired chloride diffusion toward the pit bottom due to the stagnant conditions in which the experiments were conducted and narrow geometric characteristic of the pits.

On the backward scan of the cyclic polarization curves, the difference between E_{pit} and E_{rep} in both conditions was similar. It could be attributed, again, to the pits geometric characteristics. Lower pit width-to-depth ratio in the solution containing 20 mg/L chlorides (Figure 5.24) suggested narrower pits and thus, difficulties in the repassivation of the attacked sites due to the hindered oxygen transport toward the pit bottom. Consequently, the repassivation was delayed.

Table 5.11 Characterization of the pits observed on 1.4404 electrode surface after the cyclic polarization test at 175 °C in the artificial geothermal brine containing 20 mg/L (LHD-05) and 1,500 mg/L (SBY) chlorides, respectively

c(Cl ⁻) [mg/L]	no. of pits / cm ²	width [μm]		Depth [μm]	
20	1	181	± 81	119	± 53
1,500	1	381	± 278	143	± 40

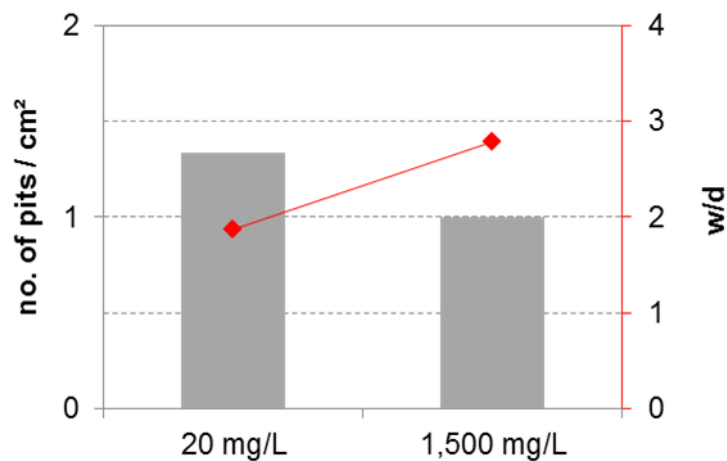


Figure 5.24 Average amount and width-to-depth ratio of the pits observed on 1.4404 electrodes after cyclic polarization at 175 °C in artificial geothermal brine containing 20 mg/L (LHD-05) and 1,500 mg/L (SBY) chlorides, respectively

5.6 Investigation of crevice corrosion susceptibility

The crevice corrosion susceptibility of stainless steel 1.4404 was investigated at 100 °C in the artificial SBY geothermal brine using a rubber pad imbedded on the electrode (Figure 3.7: B). The results obtained by cyclic polarization in the conditions with and without the simulated crevice were compared and shown in Figure 5.25 and Table 5.12. An obvious shift of the polarization curve in the active (cathodic) direction in the system with the crevice simulation was seen, resulting in the more active E_{pit} and E_{rep} , compared to the system without the crevice. Accordingly, an earlier onset of the localized corrosion was expected, which is in accordance with the results of several different authors.^{35,188,189} Furthermore, passive current densities on the forward scan increased in the latter conditions, implying to the higher dissolution rates of the metal surface. However, narrower negative hysteresis contradicts the expected more severe surface disturbance. This could be attributed to the fact that the improvised crevice former (the rubber pad) was completely covering a small part of the electrode surface that way reducing the area exposed to the SBY solution and/or the

area adjacent to the crevice acted as a cathodic site. This can also be seen from the electrode surface appearance shown in Figure 5.26; the surface exhibited no signs of corrosion attack on the lower third of the electrode (not including the lower edge). Consequently, the current density on the backward scan ceased faster in the system with the crevice simulation. However, the complete repassivation was achieved at lower potentials, indicated by the more negative E_{rep} . Such behavior could be linked to the hindered oxygen diffusion to the crevice, needed for the repassivation of the occluded active site.¹⁹⁰⁻¹⁹²

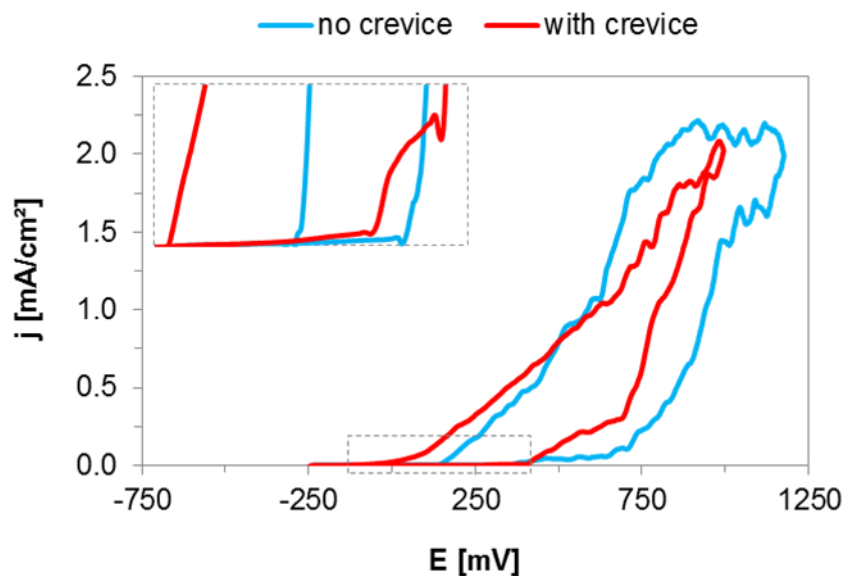


Figure 5.25 Typical cyclic polarization curve of 1.4404 in the artificial SBY geothermal brine at 100 °C with and without the crevice simulation, respectively

Table 5.12 Electrochemical data of 1.4404 determined from the cyclic polarization in the artificial SBY geothermal brine at 100 °C with and without the crevice simulation

	E_{oc} [mV]		E_{rep} [mV]			E_{pit} [mV]	
no crevice	-50	-47	109	129	673	685	
with crevice	-51	30	90	98	474	572	

The electrodes' appearance after the cyclic polarization scans, shown in Figure 5.26, revealed serious general and pitting corrosion on the lower edge of the electrode where the crevice was simulated. Due to the similarity of the corrosion attack with the corrosion occurred on the alloy exposed to the solution pH 2 (Figure 5.18), it is supposed that critical acidification occurred inside the occluded area. It is believed that such attack starts due to the oxygen depletion inside the occluded area caused by the narrow crevice geometry. This was supported by the absence of surface discoloration in the crevice, which is generally

associated to the formation of ferric oxides and/or hydroxides.^{180,181} However, oxygen reduction continued on the surfaces external to the crevice, balancing the metal dissolution within the crevice and that way causing metal cations accumulation in the occluded area. Consequently, the aggressive anionic species (e.g. chlorides, sulphates, etc.) diffused in the crevice to maintain the electrical neutrality, and caused an initiation of pitting corrosion. Moreover, the unstable corrosion products, formed in the crevice, hydrolyzed and, that way, formed critical acidic conditions that were favorable for general dissolution.^{35,188-193} Accordingly, alloy 1.4404 was susceptible to crevice corrosion in the artificial SBY geothermal brine under stagnant conditions at 100 °C.

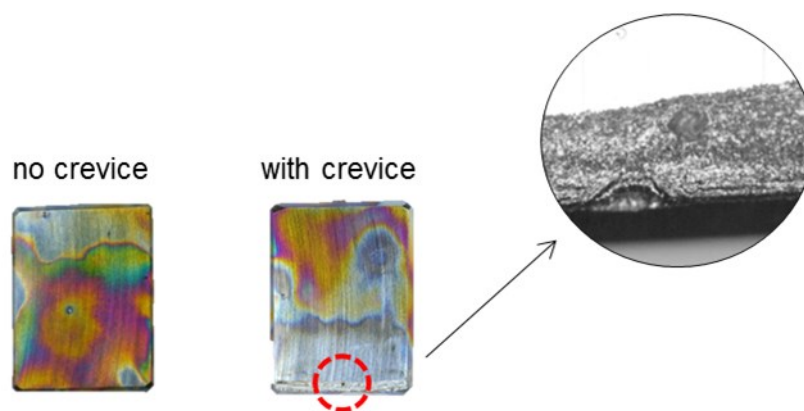


Figure 5.26 Appearance of 1.4404 electrode after the cyclic polarization in the artificial SBY geothermal brine at 100 °C with and without the crevice simulation, respectively

5.7 Investigation of stress corrosion cracking susceptibility

The susceptibility of stainless steel 1.4404 to stress corrosion cracking (SCC) was performed on U-bend coupons (Figure 3.7: C) at 175 °C by means of exposure tests for 6 months. Considering the pitting corrosion as the main precursor for SCC, the tests were conducted in the artificial LHD-23 geothermal brine, since during the 6 months of exposure only in the latter conditions pits were observed on the flat coupons.

According to the stress vs. temperature diagram calculated for the temperature range 20 °C to 175 °C, presented in Figure 5.28, the surface of the stressed coupons was approximately linearly relaxed with temperature increase. Reaching the experimental temperature of 175 °C, the stress present on the tension stretched surface of the coupon was relieved up to more than 40 % of the initial stress value (Figure 5.28). Such behavior implied to the reduced susceptibility to SCC with temperature increase. However, elevating the temperature, diffusion of aggressive species, responsible for pitting corrosion, increases in the same direction. Furthermore, the higher the temperature, the higher the crack

propagation rate of the formerly initiated cracks.¹⁹⁴⁻¹⁹⁷ Since the existence of the pits on the surface is the main precursor for SCC, it is possible to conclude that the rate determining step for SCC to occur is the formation of pits and availability of aggressive ions inside the crack tip.

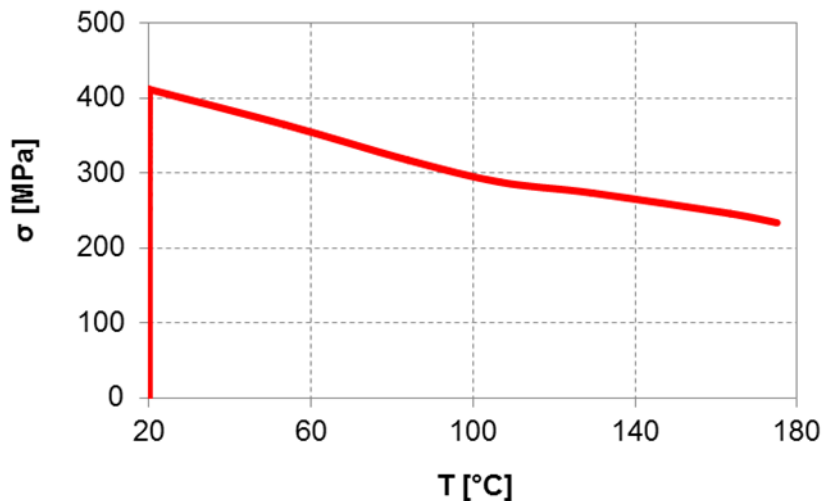


Figure 5.27 Surface relaxation of 1.4404 coupons with temperature application

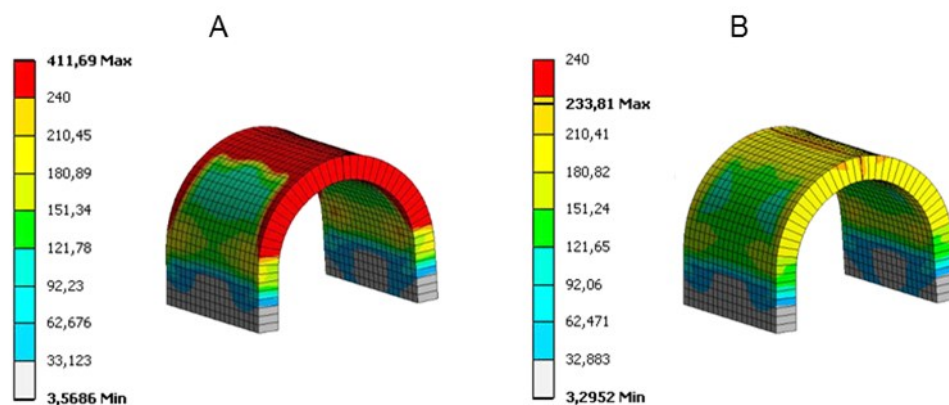


Figure 5.28 Calculated tensile stress on the surface of 1.4404 U-bend coupon at 20 °C (A) and 175 °C (B), respectively

After 6 months of exposure of the plastically deformed coupons, no cracks were observed on the coupons surface (Figure 5.29). As it was expected, pitting corrosion onset, but none of the pits acted as crack initiation sites, shown in the cross section analysis of the exposed U-bend coupons in Figure 5.29. However, it is not excluded that during the subsequent exposure time the cracks wouldn't be developed from the previously formed pits. Furthermore, in case the pitting corrosion onsets already at lower temperatures, a higher possibility for crack initiation exists due to the higher stress present in the material.⁹⁷

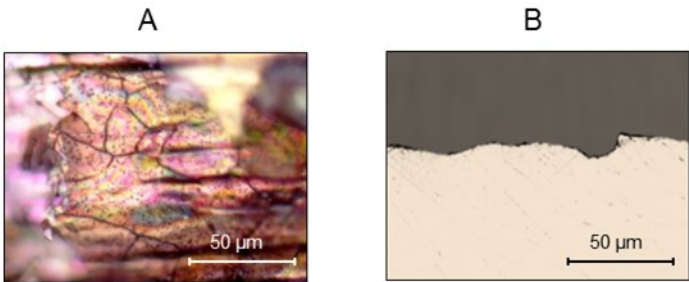


Figure 5.29 Surface (A) and cross section (B) of U-bend 1.4404 steel coupons after 6 months of exposure at 175 °C in the artificial LHD-23 geothermal brine

Chapter 6

Corrosion Resistance of High-alloyed Stainless Steel 1.4562

6.1 Introduction

In this chapter corrosion behavior of high-alloyed stainless steel 1.4562 and its dependence on various factors was evaluated, as well as the alloy's susceptibility to crevice corrosion and stress corrosion cracking. The results were obtained by means of potentiostatic (electrochemical impedance spectroscopy) and potentiodynamic (cyclic polarization) electrochemical methods, and long-term exposure tests. Tafel extrapolation method did not provide much sense in determining and predicting the corrosion rate of the alloy, due to the alloy's passive behavior observed in the investigated conditions.

6.2 Passive film growth

Similar to the surface of 1.4404 steel, high-alloyed steel 1.4562 is passivated readily even in the presence of only traces of oxygen in the atmosphere. The behavior of the metal surface, as well as the characteristics of the metal/solution interface, during the 11-day immersion tests in the artificial SBY geothermal brine at 100 °C were investigated by means of electrochemical and exposure tests.

6.2.1 Short-term electrochemical methods

6.2.1.1 Open circuit potential monitoring

During 11 days of immersion, a substantial increase in the open circuit potential (E_{oc}) was noticed from Figure 6.1. The passive layer, formed on the surface, was presumably evolved during that time and that way, caused an ennoblement of the E_{oc} . However, as a consequence a risk of passive range narrowing existed, due to the rapprochement of the E_{oc} toward the critical pitting potential (E_{pit}). To confirm this assumption, additional tests were performed and shown in the following text.

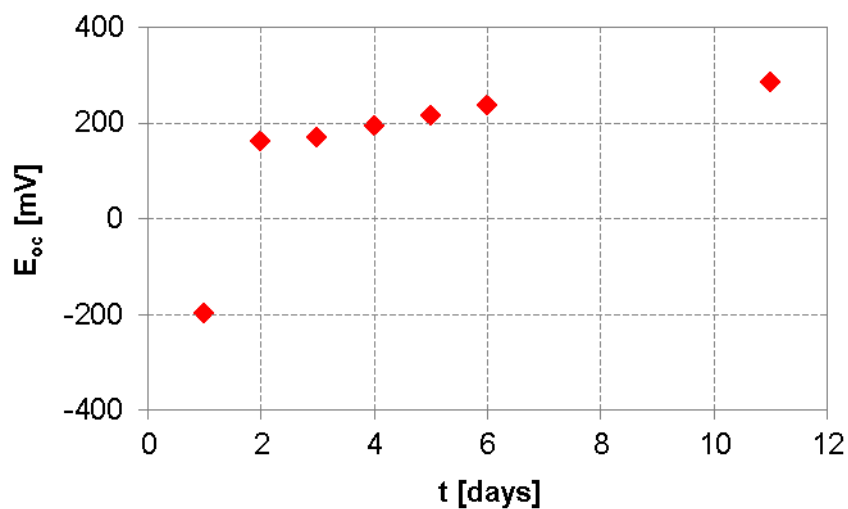


Figure 6.1 Monitoring of open circuit potential of 1.4562 steel in the artificial SBY geothermal brine at 100 °C during an 11-day immersion test

6.2.1.2 Electrode/solution interface characterization

Electrochemical impedance spectroscopy (EIS) was performed every 24 h during 11 days of electrode immersion in the investigated conditions to study the metal/solution interface behavior throughout that time. The obtained results are presented in Figure 6.2. One relaxation time was clearly resolved in each of the recorded spectra, implying to the occurrence of one physical process on the metal/solution interface. The semi-circles exhibited pure, however non-ideal capacitive behavior (Figure 6.2: A). Their diameter tended to increase with time, which was a clear indication of the interface impedance increase. Such behavior was better perceived in the Bode modulus plot in the low frequency (LF) domain (Figure 6.2: B).

Based on the aforementioned observations, the metal/solution interface was modeled using the equivalent electrical circuit shown in Figure 3.1: A. The results of the fit are presented in Table 6.1. According to the α values being < 1 , a non-ideal capacitive

behavior was confirmed. Calculating the true capacitance (C) from the Equation (3.1) for each of the recorded spectra, it was found that the observed phenomena were linked to the double layer. Accordingly, the corresponding resistance R was the charge transfer resistance, directly associated with the single kinetically controlled electrochemical reaction. It was, therefore, possible to conclude that during 11 days of exposure the affinity of the alloy to the oxidation significantly decreased. The crucial moment happened after the 2nd day of immersion, when the resistance increased for more than one order of magnitude. This was, presumably, caused by the evolution of the passive layer that hindered the diffusion of oxidizing species toward the bare metal surface. However, due to the thin nature of the passive film, it was not possible to detect it in the applied frequency range.

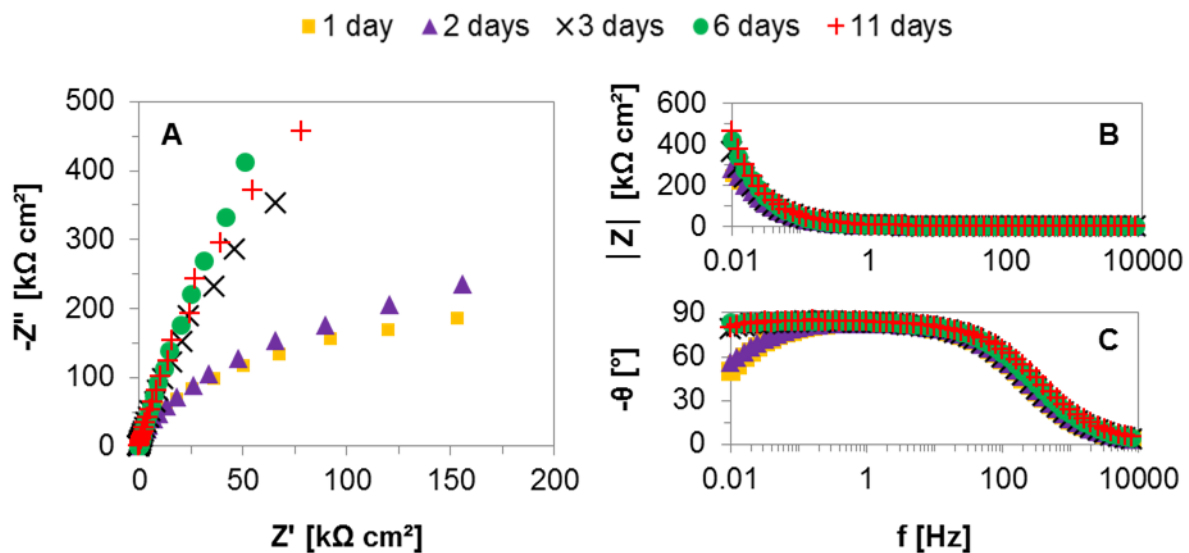


Figure 6.2 Typical impedance spectra for 1.4562 in the artificial SBY geothermal brine at 100 °C under E_{oc} conditions as a function of immersion time

Table 6.1 Electrochemical data obtained by EIS for 1.4562 during an 11-day immersion test in the artificial SBY geothermal brine at 100 °C under E_{oc} conditions

t [days]	R_s [Ω]	R [$k\Omega\text{ cm}^2$]	Q [$\mu\text{S s}^\alpha/\text{cm}^2$]	α	C [$\mu\text{F}/\text{cm}^2$]
1	4	452	41	0.919	23
2	4	611	39	0.920	22
3	4	10,643	37	0.923	21
4	3	n/a	35	0.924	20
5	3	n/a	34	0.925	19
6	3	n/a	32	0.925	18
11	3	38,929	29	0.925	16

6.2.1.3 Determination of critical potentials

To determine the shift of the potentials at which the localized corrosion initiated, cyclic polarization of the metal electrodes was performed after 1 and 11 days of exposure. The recorded curves are depicted in Figure 6.3. Similar values for the E_{pit} and E_{rep} were observed irrespective of the exposure time, indicating a reduction in the passivity range with time due to the ennoblement of the E_{oc} . Furthermore, slightly lower corrosion current density was observed after 11 days, implying to the passive layer evolution.

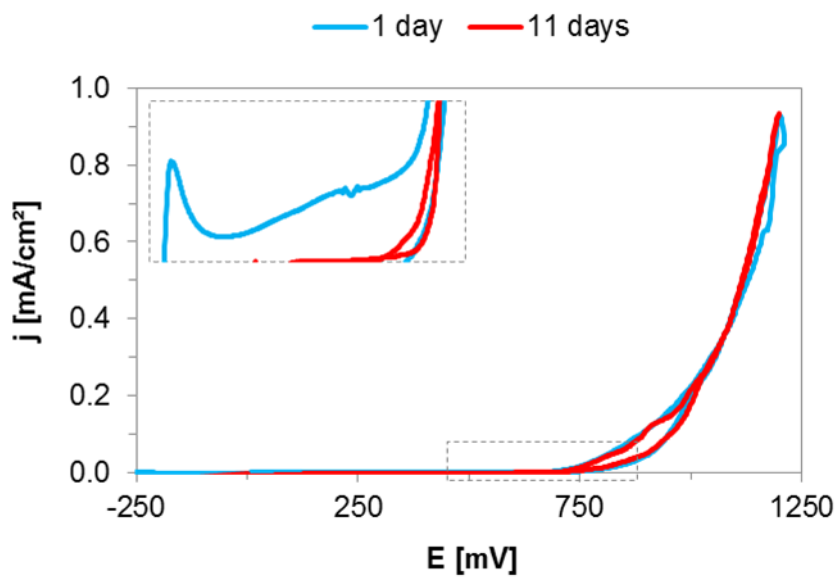


Figure 6.3 Typical cyclic polarization curves of 1.4562 after 1 and 11 days of immersion in the artificial SBY geothermal brine at 100 °C

Table 6.2 Electrochemical data of 1.4562 determined from the cyclic polarization curves after 1 and 11 days of immersion in the artificial SBY geothermal brine at 100 °C

t [days]	E_{oc} [mV]		E_{rep} [mV]		E_{pit} [mV]	
1	-220	-181	869	891	932	951
10	279	292	902	913	927	938

6.2.2 Long-term exposure tests

Exposure tests up to 6 months were performed on 1.4562 steel coupons in order to study the influence of the longer immersion time on the metal surface. No signs of corrosion attack, either uniform or localized, were visible on the coupons indicating an excellent stability and compactness of the passive layer (Figure 6.4). XRD analysis of the surface exposed for 6 months in the investigated conditions did not give any information on

the passive layer structure due to its very thin nature, as already suggested with the impedance spectroscopy. Accordingly, one can conclude that the layer was only a few nm thick, but yet compact enough to provide an excellent resistance to uniform and localized corrosion during the 6 months of exposure in the artificial SBY geothermal brine at 100 °C.



Figure 6.4 Appearance of 1.4562 coupon after 6 months of exposure in the artificial SBY geothermal brine at 100 °C

6.3 Influence of temperature on corrosion performance

Temperature effect on the corrosion behavior of high-alloyed stainless steel 1.4562 was investigated in the artificial SBY geothermal brine at 70 °C, 100 °C and 175 °C.

6.3.1 Short-term electrochemical methods

6.3.1.1 Open circuit potential monitoring

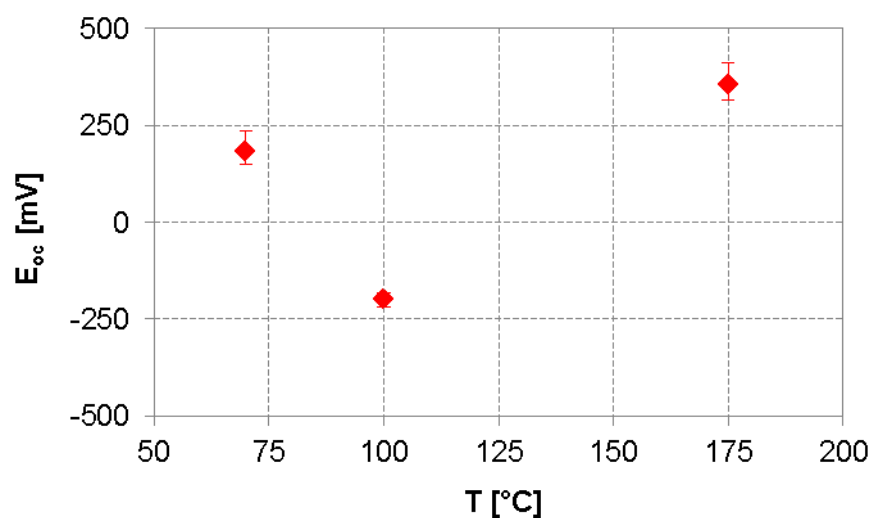


Figure 6.5 Open circuit potentials of 1.4562 steel in the artificial SBY geothermal brine at different temperatures

After 20 h of immersion in the artificial SBY geothermal brine open circuit potentials (E_{oc}) of 1.4562 were determined. The results are shown in Figure 6.5. Increasing the temperature to 100 °C the E_{oc} shifted in the cathodic direction, implying to the more active electrode surface. Further increase of the temperature to 175 °C led to the ennoblement of the E_{oc} , suggesting the formation of a passive layer with better protective characteristics. In order to obtain more detailed information about the corrosion behavior, additional tests were performed.

6.3.1.2 Electrode/solution interface characterization

Temperature influence on the electrode/solution interface was studied using electrochemical impedance spectroscopy (EIS). Typical impedance spectra recorded for 1.4562 in the artificial SBY geothermal brine under E_{oc} conditions at different temperatures are depicted in Figure 6.6. Nyquist representation of the impedance data (Figure 6.6: A) revealed the presence of one depressed capacitive semi-circle at 70 °C and 100 °C, characteristic for one process occurring on the electrode/solution interface (e.g. charge transfer, diffusion, adsorption, etc.). On the other hand, at 175 °C two time constants were resolved, which overlapped at approximately 100 mHz. This was a clear indication of the existence of two processes occurring simultaneously on the electrode surface. Additionally, both high- (HF) and low-frequency (LF) semi-circles were depressed and exhibited a non-ideal capacitive behavior. Increase in the temperature resulted in the reduction of the semi-circle diameter (Figure 6.6: A), apparent also in the LF domain of the Bode modulus plot (Figure 6.6: B). Furthermore, an increased deviation from an ideal capacitive behavior was noticed from the Bode phase angle plot (Figure 6.6: C). This clearly indicated the reduction in the corrosion resistance of the interface and increased roughness of the surface.

Considering the visual interpretation of the obtained spectra, the impedance data were modelled using the equivalent electrical circuits presented in Figure 3.1: A (70 °C, 100 °C) and B (175 °C). The results of the fit are shown in Table 6.3. A non-ideal capacitive behavior of the interface irrespective of the temperature was confirmed. Furthermore, with temperature rise α decreased, meaning; the time constant distribution increased. The true capacitance values (C) calculated according to Equation (3.1), were within the range characteristic for the double layer capacitance, proving that the phenomenon occurring on the electrode/solution interface could be linked to the charge transfer. Accordingly, resistance R_1 was charge transfer resistance, directly associated with the single kinetically controlled electrochemical reaction. It was, therefore, possible to compare the corrosion behavior of the electrodes at different temperatures and observe that with temperature increase, the resistance decreased significantly. This was a clear indication of an increased oxidation rate

of the metal electrode with temperature. Furthermore, increasing the temperature, the passive layer, formed on the surface, evolved and became thicker, as suggested by its longer relaxation time and thus, visibility during the frequency scan. Even though its resistance R_2 contributed to the overall resistance of the system and lowered the migration rate of the ionic species to and from the electrode surface, the affinity of the alloy to the charge transfer at 175 °C was still rather high, as suggested by the low resistance of the double layer.

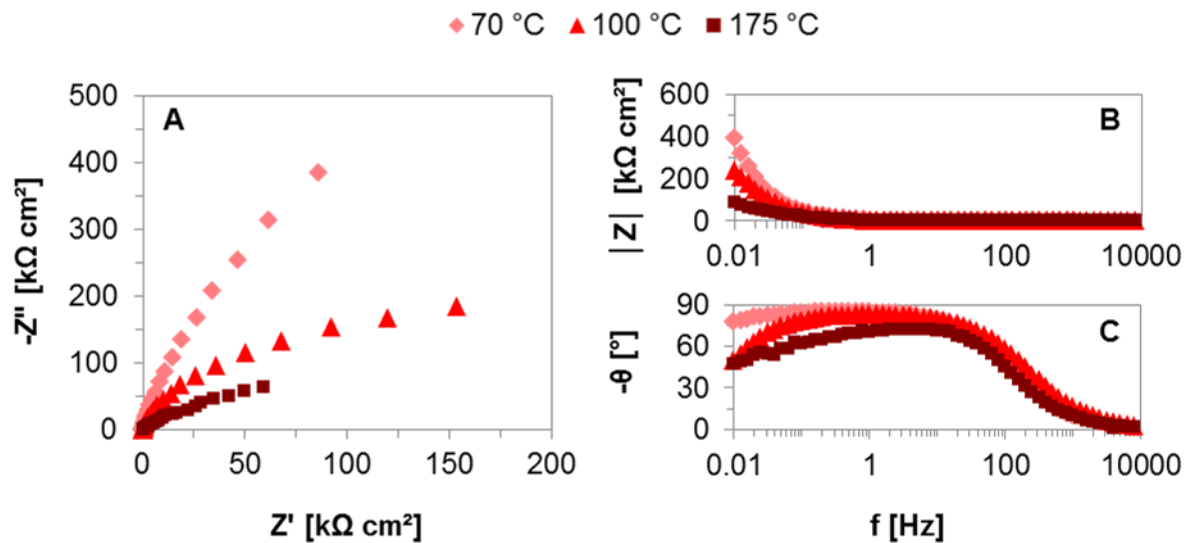


Figure 6.6 Typical impedance spectra for 1.4562 steel in the artificial SBY geothermal brine at different temperatures under E_{oc} conditions

Table 6.3 Electrochemical data obtained by EIS for 1.4562 in the artificial SBY geothermal brine under E_{oc} conditions at different temperatures

T [°C]	R_s [Ω]	R_1 [kΩ cm ²]	Q_1 [mS s ^α /cm ²]	α_1	C_1 [μF/cm ²]	R_2 [kΩ cm ²]	Q_2 [mS s ^α /cm ²]	α_2	C_2 [μF/cm ²]
70	7	3,094	0.034	0.941	23	-	-	-	-
100	4	452	0.041	0.919	23	-	-	-	-
175	7	10	0.050	0.878	22	358	0.028	0.516	0.1

6.3.1.3 Determination of critical potentials and pits characterization

Typical cyclic polarization curves obtained for 1.4562 in the artificial SBY geothermal brine at the investigated temperatures is shown in Figure 6.7. The electrochemical data determined from the curves are presented in Table 6.4.

At 70 °C and 100 °C the surface of the electrodes exhibited passive behavior over an extensive potential range of more than 800 mV. This implied to an excellent resistance to uniform and pitting corrosion. Polarization curve at 175 °C was significantly

shifted toward active potentials, indicating a substantial reduction in the passive range. This resulted in an increased susceptibility of the alloy to pitting corrosion. E_{pit} were slightly reduced as the temperature increased from 70 °C to 100 °C. This could be ascribed to the temperature effect on chlorides behavior - the main ionic species considered responsible for pitting corrosion in the investigated conditions. Increasing the temperature, the chlorides diffusion rate and chemisorption on active sites increased, resulting in an earlier onset of the current density due to the passive film breakdown. For the same reason, pitting corrosion at 175 °C initiated at even lower potentials. Once the E_{pit} were reached, curves had relatively similar slopes at all investigated temperatures. However, the highest current on the forward scan was reached at 175 °C, suggesting the highest amount of pits and/or the propagation depth inside the bare electrode occurred at the latter temperature. In addition, an excessive hysteresis in the same conditions implied to the very slow repassivation of the attacked local sites. This could be ascribed to the amount of the surface disruption; the more disrupted the surface, the harder to repassivate it. That is why the repassivation currents ceased rather quickly at lower temperatures, resulting in very noble E_{pit} . E_{oc} in the latter case was more negative than the E_{rep} , meaning that in normal stagnant service conditions the surface of 1.4562 would be completely passivated, without the possibility of metastable pitting to occur. Therefore, excellent repassivation capability could be assigned to alloy 1.4562 at 70 °C and 100 °C. However, at 175 °C E_{oc} were located between E_{rep} and E_{pit} , suggesting very poor repassivation capability at normal stagnant service conditions and the possibility of metastable pitting occurrence.

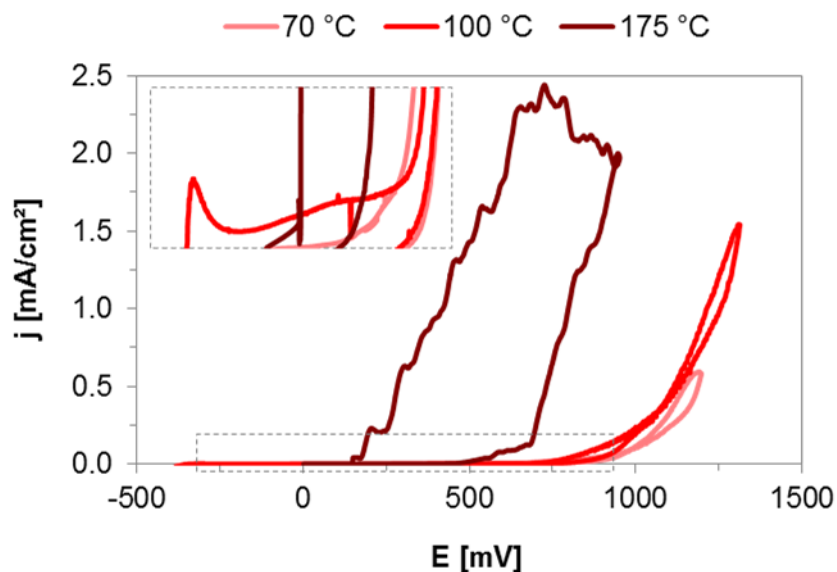


Figure 6.7 Typical cyclic polarization curves of 1.4562 in the artificial SBY geothermal brine at different temperatures

Table 6.4 Electrochemical data of 1.4562 determined from the cyclic polarization curves in the artificial SBY geothermal brine at different temperatures

T [°C]	E_{oc} [mV]		E_{rep} [mV]		E_{pit} [mV]	
70	147	– 235	932	– 1042	957	– 1055
100	-220	– -181	869	– 891	932	– 951
175	314	– 415	182	– 271	523	– 656

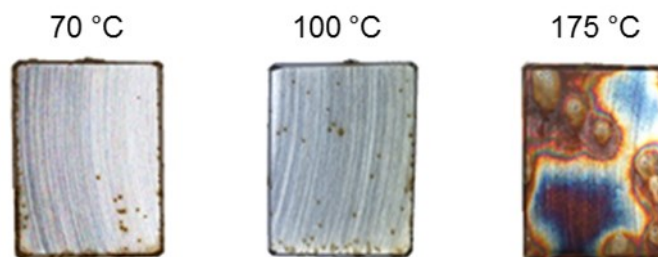


Figure 6.8 Appearance of 1.4562 electrode surface after anodic polarization in artificial SBY geothermal brine at different temperatures

Despite the narrowness of the hysteresis observed on the cyclic polarization scan, pitting corrosion on the electrodes surfaces at 70 °C and 100 °C was appreciable as shown in Figure 6.8 and Table 6.5. The electrodes surface remained lustrous, suggesting only preferential local sites were attacked by the corrosive medium. With a temperature increase to 100 °C, the amount of the formed pits increased (Figure 6.9), as well as the pits width and depth (Table 6.5). This could be assigned to the higher adsorption and diffusion rates of the aggressive species, mainly chlorides, toward the active sites and through the passive layer, respectively, resulting in a more severe attack of the bare electrode surface. Considering an increase in the pit width-to-depth ratio with the temperature rise from 70 °C to 100 °C (Figure 6.9), one can conclude that the pits walls were dissolved preferentially over the bottoms. The reason for such behavior could be the impaired chlorides diffusion inside the pits, due to the stagnant conditions in which the experiments were conducted and narrow geometric characteristic of the pits.

With further temperature increase to 175 °C, an appreciable surface discoloration was perceived on the electrode surface (Figure 6.8). This behavior was noticed on 1.4404 alloy in the same conditions. It is usually attributed to the formation of stable ferric compounds, different thickness and colors, which interfere with each other.^{180,181} The reason why such effect was not observed at lower temperatures, could be due to the higher passive film dissolution rates (compared to 70 °C) and oxygen presence (compared to 100 °C), which

makes it possible for these compounds to form. Beside the surface discoloration, pit clusters were observed on the electrode surface at 175 °C. Their size was much larger compared to the pits at lower temperature, but the width-to-depth ratio was lower (Figure 6.9). It seems that the chlorides ingress inside the pits was significantly promoted with the temperature increase to 175 °C, resulting in a substantial increase in the pits depth (Table 6.5).

Table 6.5 Characterization of the pits observed on 1.4562 electrode surface after cyclic polarization in the artificial SBY geothermal brine at different temperatures

T [°C]	no. of pits / cm ²	width [μm]	depth [μm]
70	4	45 ± 20	22 ± 9
100	15	70 ± 30	26 ± 22
175	2	393 ± 193	234 ± 136

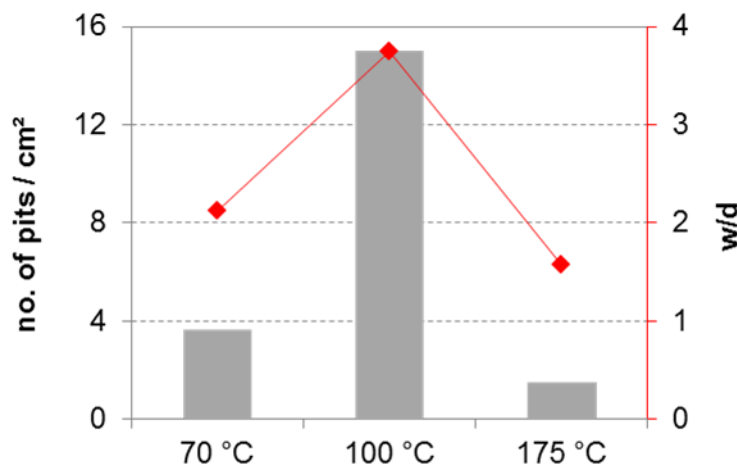


Figure 6.9 Amount and average width-to-depth ratio of the pits observed on 1.4562 after cyclic polarization in the artificial SBY geothermal brine at different temperatures

6.3.2 Long-term exposure tests

Coupons of high-alloyed stainless steel grade 1.4562 were exposed to the artificial SBY geothermal brine for 1, 3 and 6 months at 100 °C and 175 °C. Weight loss method revealed extremely low mass loss during the whole exposure time (< 0.0001 g). Accordingly, the calculated corrosion rates were < 0.06 μm/y. Such finding proved an excellent resistance of alloy 1.4562 to uniform corrosion in the investigated conditions.



Figure 6.10 Appearance of 1.4562 coupons after 6 months of exposure in the artificial SBY geothermal brine at 100 °C and 175 °C, respectively

Surface analysis of the exposed coupons (Figure 6.10 and Figure 6.11) supported the calculations obtained by the weight loss test method. Hardly any signs of corrosion attack were visible on the surface with an optical microscope, implying to an excellent passive behavior during the 6 months of exposure in the investigated conditions. At 100 °C the coupons retained a lustrous surface. However, at 175 °C light deposits were observed on the coupon surface, suggesting that with further exposure time, the passive layer could experience a breakdown and the surface could become active.

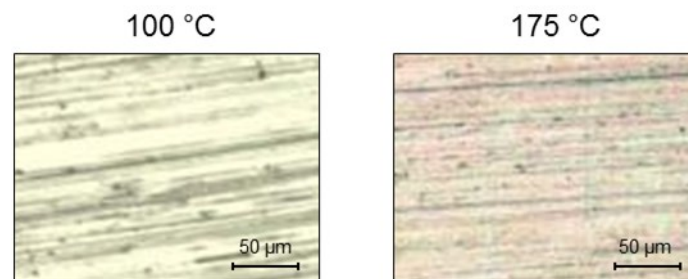


Figure 6.11 Surface of 1.4562 coupons after 6 months of exposure in the artificial SBY geothermal brine at 100 °C and 175 °C, respectively

6.4 Influence of acidity on corrosion performance

The influence of the solution acidity on the behavior of 1.4562 was investigated at 175 °C in the artificial geothermal brine pH 2 (LHD-23) and pH 4 (SBY), respectively.

6.4.1 Short-term electrochemical methods

6.4.1.1 Open circuit potential monitoring

After 20 h of immersion in the investigated solutions open circuit potentials (E_{oc}) of 1.4562 were determined. The obtained results are shown in Figure 6.12. Increasing the

solution acidity, the E_{oc} decreased substantially, suggesting an increased surface activity. Such observation could be attributed to the higher concentration of oxidizers in the LHD-23 solution, resulting in the higher passive film dissolution rates. In order to obtain more detailed information about the corrosion behavior and support the assumptions, additional electrochemical methods and exposure tests were performed.

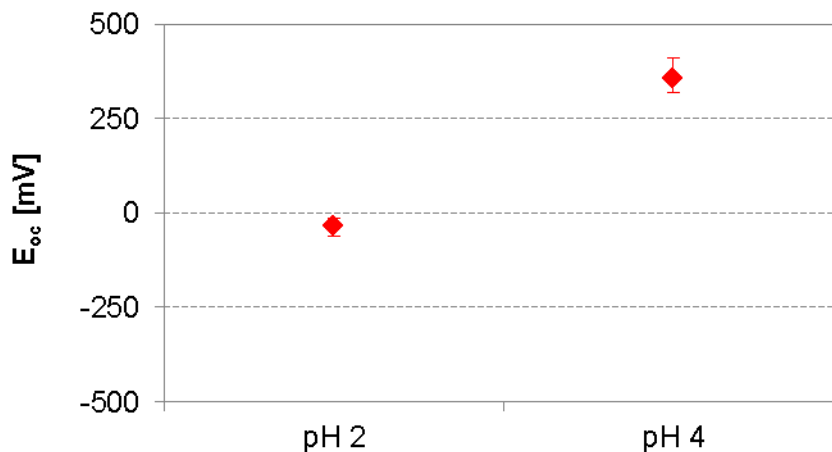


Figure 6.12 Open circuit potentials for 1.4562 after 20 h of immersion at 175 °C in the artificial geothermal brine pH 2 (LHD-23) and pH 4 (SBY), respectively

6.4.1.2 Electrode/solution interface characterization

Influence of the solution acidity on the electrode/solution interface, studied with electrochemical impedance spectroscopy (EIS), is depicted in Figure 6.13. Nyquist representation of the impedance data (Figure 6.13: A and B) revealed a substantial difference in the curves diameter, suggesting large difference in the systems impedance. Two depressed semi-circles were clearly resolved in the more acidic solution spectrum. In the solution with higher pH, time constant in the high-frequency (HF) domain was almost completely restrained by the occurrence of the second one in the low-frequency (LF) domain, indicating extremely short relaxation time of the corresponding physical process. In both cases the second time constant appeared at approximately 250 mHz. Reduction in the solution resistance was observed with the solution pH reduction (Figure 6.13: B and C), confirming an increase in the solution conductivity, most probably due to the higher hydrogen ion concentration. Furthermore, significantly smaller impedance curve diameter was apparent (Figure 6.13: A), suggesting reduction in the interface impedance in the more acidic brine. This observation was in agreement with the Bode modulus plot, showing decrease of the impedance in the LF domain (Figure 6.13: C).

According to the visual observations, the physical processes occurring on the electrode/solution interface in both conditions could be modeled with an electrical circuit

presented in Figure 3.1: B. The results of the fit are shown in Table 6.6. It was found that α values were lower in the more acidic conditions, implying to the greater time constant distribution at the surface exposed to the solution pH 2. Consequently, higher capacitance values (C) were expected, as proved from the calculations according to the Equation (3.1) from the corresponding Q . The outer layers, formed on the surface in different pH conditions,

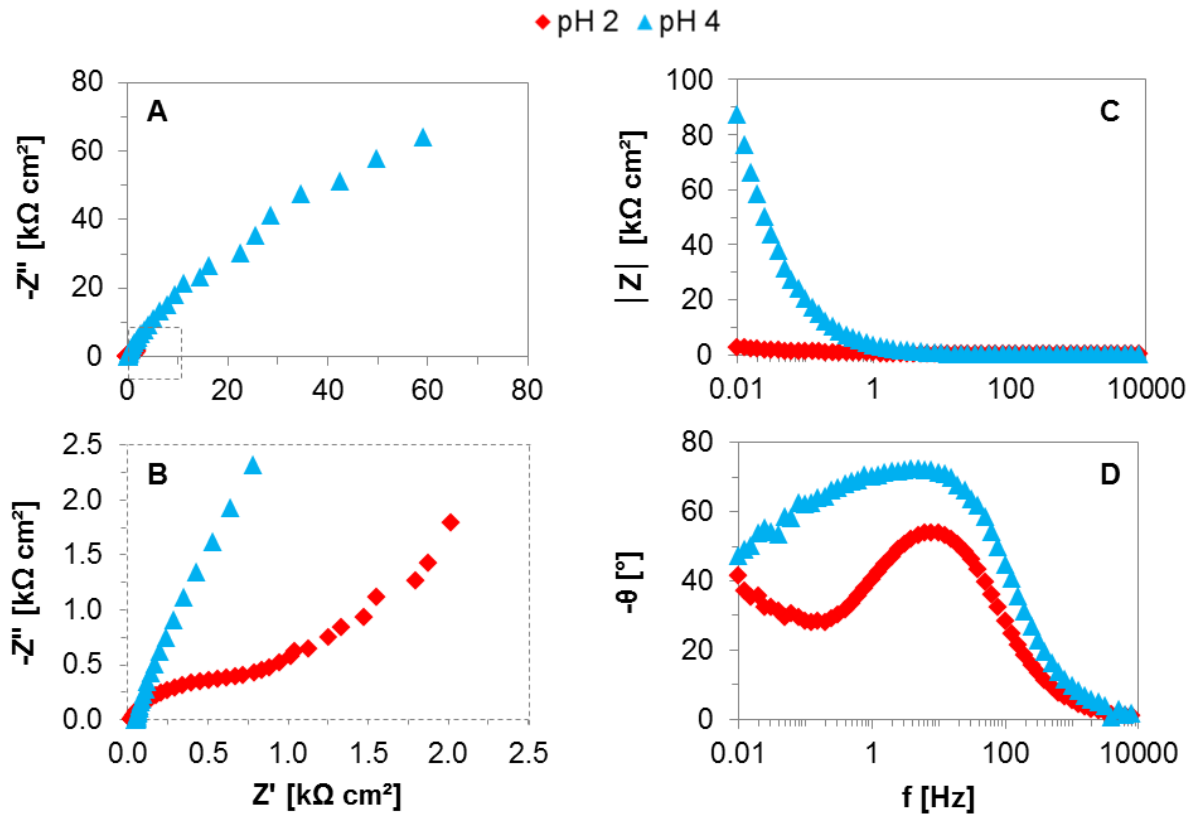


Figure 6.13 Typical impedance spectra for 1.4562 at 175 °C under E_{oc} conditions in the artificial geothermal brine pH 2 (LHD-23) and pH 4 (SBY), respectively

Table 6.6 Electrochemical data obtained by EIS for 1.4562 at 175 °C under E_{oc} conditions in the artificial geothermal brine pH 2 (LHD-23) and pH 4 (SBY), respectively

pH	R_s [Ω]	R_1 [$k\Omega\text{ cm}^2$]	Q_1 [$mS\text{ s}^\alpha/cm^2$]	α_1	C_1 [$\mu F/cm^2$]	R_2 [$k\Omega\text{ cm}^2$]	Q_2 [$mS\text{ s}^\alpha/cm^2$]	α_2	C_2 [$\mu F/cm^2$]
2	3	1	0.28	0.812	90	18	2.300	0.601	377.7
4	7	10	0.05	0.878	22	358	0.028	0.516	0.1

exhibited values characteristic for the double layer capacitance, proving that the phenomenon could be linked to the charge transfer inside the double layer. Accordingly, the outer layer resistances R_1 were directly associated to the resistances to the electrode oxidation. It was therefore, possible to conclude that with pH decrease, the metal dissolution

rate increased. Furthermore, in both conditions a passive layer evolved adjacent to the electrode surface. Its resistance R_2 was much higher and capacitance C_2 lower in the less acidic conditions, implying to the formation of a thicker and more compact, i.e. less porous, layer in the latter conditions.

6.4.1.3 Determination of critical potentials and pits characterization

Typical cyclic polarization curves for 1.4562 recorded at 175 °C in the artificial geothermal brine pH 2 (LHD-23) and pH 4 (SBY), respectively, are depicted in Figure 6.14. The electrochemical data determined from the curves are presented in Table 6.7. Increasing the solution acidity the electrode surface was passive over an appreciably wider potential range. This was mainly because of the shift of the E_{oc} in the negative direction as the solution pH was decreased. However, higher passive currents were noticed, resulting in higher dissolution rates of the passive layer. This was in agreement with the expected; higher concentration of the hydrogen ions, i.e. oxidants, led to the larger cathodic currents, which eventually resulted in higher anodic dissolution rates.

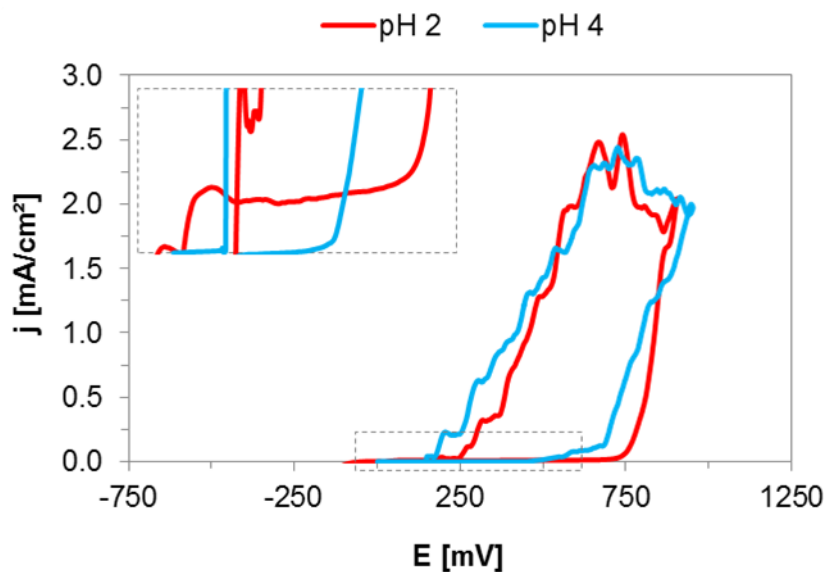


Figure 6.14 Typical cyclic polarization curve of 1.4562 at 175 °C in the artificial geothermal brine pH 2 (LHD-23) and pH 4 (SBY), respectively

The shape of the anodic polarization curves on the forward and backward scan was very much alike, implying to the similar level of surface disruption. Increasing the solution acidity, the curve shifted in the anodic direction, resulting in the nobler E_{pit} and E_{rep} . Such feature was noticed also for 1.4404 in the same conditions, and it could be most probably ascribed to the increased sulphate-to-chloride ratio.¹⁸⁵⁻¹⁸⁷ As already mentioned in the previous chapter, in such conditions the adsorption of the sulfates on active sites and

surface defects inhibits the ingress of more aggressive chloride anions. Consequently, the initiation of pitting corrosion was delayed, as noticed from the more positive E_{pit} .

The ability of 1.4562 to repassivate was significantly higher in the more acidic solution, despite the similar potentials at which the current ceased below the 0.1 mA/cm^2 . The main reason was the more active E_{oc} in the LHD-23 solution, which was more negative than the E_{rep} . Therefore, once the system was returned to its initial stage after the anodic polarization, all the propagated pits were repassivated. Controversially, in the solution pH 4, a very poor repassivation ability was observed, due to the more positive E_{oc} compared to the E_{rep} . Furthermore, in the normal stagnant service conditions metastable pitting corrosion could occur.

Table 6.7 Electrochemical data of 1.4562 determined from the cyclic polarization at $175 \text{ }^\circ\text{C}$ in the artificial geothermal brine pH 2 (LHD-23) and pH 4 (SBY), respectively

pH	E_{oc} [mV]		E_{rep} [mV]			E_{pit} [mV]	
	Start	End	Start	End	Start	End	
2	-60	-11	213	301	739	757	
4	314	415	182	271	523	656	

Surface analysis of the polarized electrode in the more acidic solution revealed the electrode surface remained lustrous after the cyclic polarization test. In the less acidic conditions surface discoloration was observed. Most reasonable explanation for not observing the surface discoloration in the more acidic solution could be due to the highly acidic conditions, unfavorable for the formation of ferric compounds, responsible for such effect.

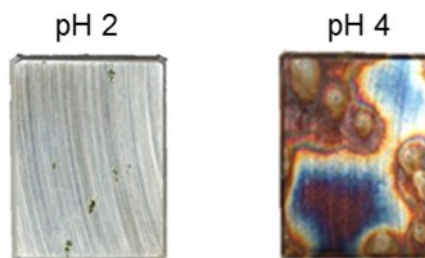


Figure 6.15 Appearance of 1.4562 electrode after the cyclic polarization test at $175 \text{ }^\circ\text{C}$ in the artificial geothermal brine pH 2 (LHD-23) and pH 4 (SBY), respectively

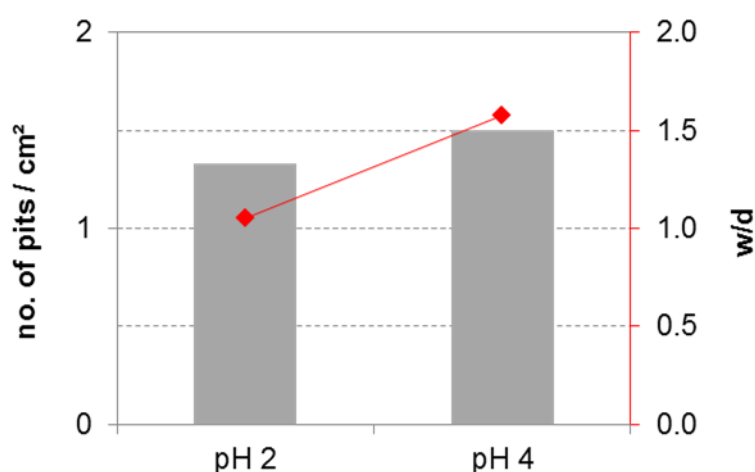


Figure 6.16 Amount and average width-to-depth ratio of the pits observed on 1.4562 after cyclic polarization in the solution pH 2 (LHD-23) and pH 4 (SBY) at 175 °C, respectively

Susceptibility to pit initiation due to the anodic polarization was observed in both conditions. However, more severe pitting corrosion was pronounced in the lower pH solution. This was obvious from the determined amount and size of the pits, shown in Table 6.8 and Figure 6.16. Narrower, but deeper pits were formed on the electrode surface in the more acidic conditions. Two possible explanations could be reasonable for such behavior. First; increased concentration of the sulphates in the LHD-23 brine presented higher concentration of aggressive ions, responsible for pitting corrosion. Second; depletion of the oxidants, i.e. hydrogen ions, inside the formed pits due to the difficulties in mass transfer, resulted in pits acting as an anode and the surrounding surface as a cathode. Since the concentration of oxidants in LHD-23 was much more abundant compared to SBY solution, cathodic reaction on the electrode surface was continuously ongoing, thereby stimulating the dissolution of the pit bottom. Decreased pit width-to-depth ratio as the solution acidity increased (Figure 6.16) corroborated the proposed explanations; pits bottoms were preferentially dissolved over the pits walls.

Table 6.8 Characterization of the pits observed on 1.4562 electrode surface after the cyclic polarization test in the solution pH 2 (LHD-23) and pH 4 (SBY) at 175 °C, respectively

pH	no. of pits / cm ²	width [μm]	depth [μm]
2	1	232 ± 132	254 ± 98
4	2	393 ± 193	234 ± 136

6.4.2 Long-term exposure tests

High-alloyed stainless steel 1.4562 coupons were exposed for different time periods at 175 °C to the artificial brine pH 2 and pH 4. According to the coupons weight loss (< 0.0001 g), the corrosion rates in the less acidic conditions were < 0.06 $\mu\text{m}/\text{y}$. Such behavior was ascribed to the formation of chromium (III) passive layer that provided excellent resistance to uniform corrosion. Surface analysis showed no evidence of localized attack during the 6 months of exposure (Figure 6.19: B). Similar behavior was noticeable in the more acidic solution, but only during the first month of exposure (Figure 6.17). Afterwards, the corrosion rate increased with time, suggesting increased passive layer dissolution rates.

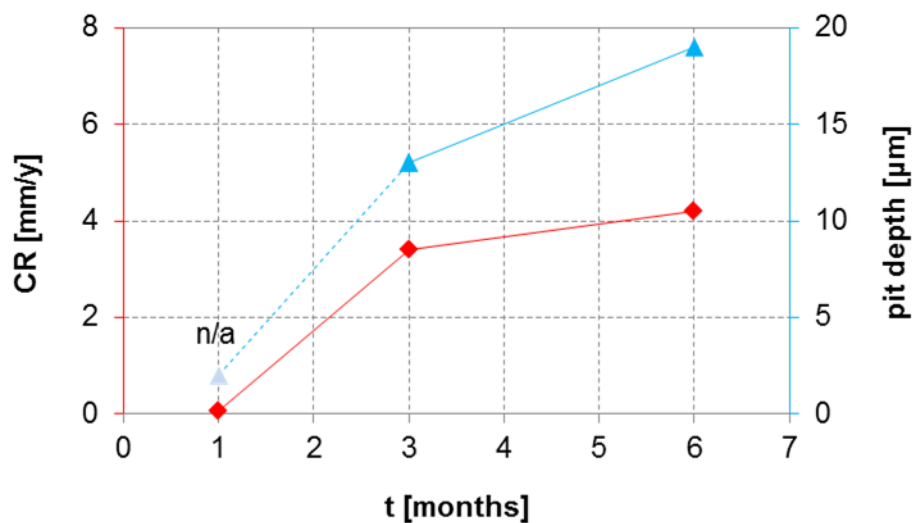


Figure 6.17 Calculated corrosion rates and measured pits depth of 1.4562 after exposure in the artificial geothermal brine pH 2 at 175 °C

Examining the coupons after the exposure tests, the alloy surface remained lustrous even after 6 months of exposure. However, an adherent greenish layer formed, which could be a stable ferrous hydroxide, $\text{Fe}(\text{OH})_2$,⁷⁷ resulting from a previously formed ferrous sulphate (Equation (2.7)) due to the increased sulphate concentration present in the LHD-23 solution. Closer inspection of the material surface revealed the presence of grain boundaries and numerous pits formed on the surface (Figure 6.19: A). However, cross section analysis revealed no signs of pits propagating into the metal structure (Figure 6.19: B), implying to the occurrence of shallow pitting corrosion. Nevertheless, increasing the exposure time, the pits depth increased (Figure 6.17). Considering the greater increase in the pit depth than the corrosion rate with time, once again the unreliability of the weight loss method in determining the rate of localized corrosion was proved. On contrary, it can provide misleading results, which could cause a failure of the system. Nevertheless, solution pH 2 clearly caused higher uniform dissolution rates, supporting the results obtained by EIS; the

significantly lower resistance of the passive layer formed on the surface exposed to the solution pH 2.

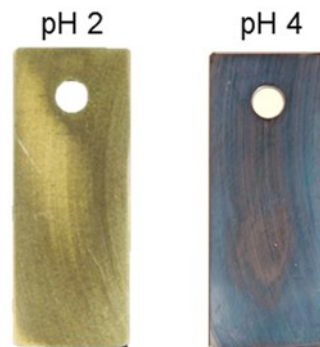


Figure 6.18 Appearance of 1.4562 coupons after 6 months of exposure in the artificial geothermal brine pH 2 (LHD-23) and pH 4 (SBY), respectively

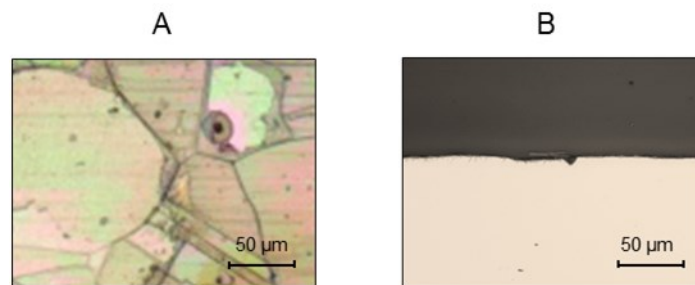


Figure 6.19 Surface (A) and cross section (B) of 1.4562 coupons after 6 months of exposure in the artificial geothermal brine pH 2 (LHD-23)

6.5 Influence of salt concentration on corrosion performance

The effect of an increased salt concentration on the corrosion behavior of 1.4562 was investigated at 175 °C in the artificial geothermal brine containing 20 mg/L (LHD-05) and 1,500 mg/L (SBY) chlorides, respectively.

6.5.1 Short-term electrochemical methods

6.5.1.1 Open circuit potential monitoring

Open circuit potentials (E_{oc}) of 1.4562 electrodes after 20 h of immersion in the solution containing 20 mg/L (LHD-05) and 1,500 mg/L (SBY) chlorides, respectively, are shown in Figure 6.20. More active E_{oc} were noticed in the brine containing less chloride. This could be linked to the higher oxygen concentration present in the LHD-05 solution, due to the less salt, which drove the cathodic reaction. Consequently, the anodic oxidation of the electrode was stimulated, resulting in the more active surface.

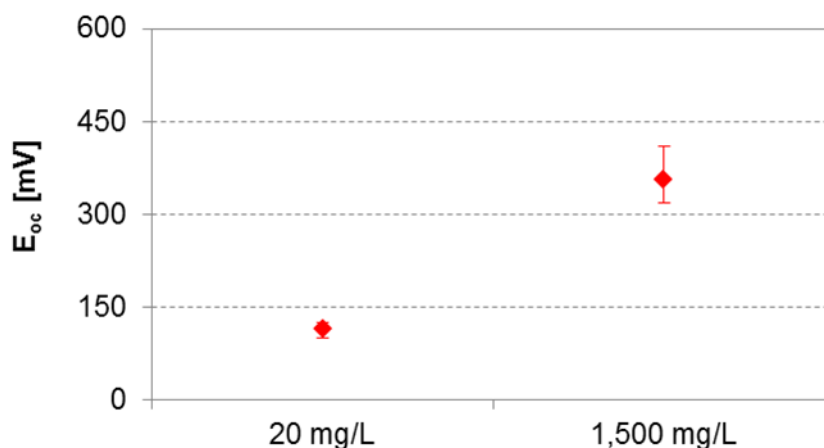


Figure 6.20 Open circuit potentials of 1.4562 after 20 h of immersion at 175 °C in the artificial geothermal brine containing 20 mg/L (LHD-05) and 1,500 mg/L (SBY) chlorides

6.5.1.2 Electrode/solution interface characterization

Behavior of the electrode/solution interface in the solution with different salt content was characterized using electrochemical impedance spectroscopy (EIS). Typical impedance spectra recorded for 1.4562 under E_{oc} conditions at 175 °C in the artificial geothermal brine containing 20 mg/L (LHD-05) and 1,500 mg/L (SBY) chlorides, respectively, are presented in Figure 6.21. Bode modulus representation of the impedance data revealed one relaxation time in the spectrum recorded in the solution with less chloride (Figure 6.21: B), suggesting an occurrence of one process on the electrode/solution interface (e.g. charge transfer, diffusion, adsorption, etc.). A non-ideal capacitive behavior of the interface was clearly seen (Figure 6.21: A and C), which, in addition, implied to the surface heterogeneity. The reduction in the solution resistance was noticeable from the Bode modulus plot (Figure 6.21: B) in the high-frequency (HF) domain as the solution concentration increased. Such behavior was attributed to the increased ionic species in the solution with the addition of soluble salts, which resulted in increased solution conductivity, i.e. decreased resistivity. However, from the low-frequency (LF) domain of the modulus plot the resistance of the interface seemed to increase with the solution concentration. This could be attributed to the formation of a more protective layer on the electrode surface and/or, generally, lower dissolution rates due to the less corrosive environment owing to the lower oxygen concentration.

According to the visual observation, the equivalent electrical circuits, presented in Figure 3.1: A and B, were used to fit the impedance data obtained in the solutions containing 20 mg/L and 1,500 mg/L chlorides, respectively. The results of the fit are given in Table 6.9. It was found that α values were always < 1 , confirming the CPE behavior and the

heterogeneous time constant distribution. Higher capacitance values (C) in the less concentrated solution were calculated according to Equation (3.1) from the corresponding Q .

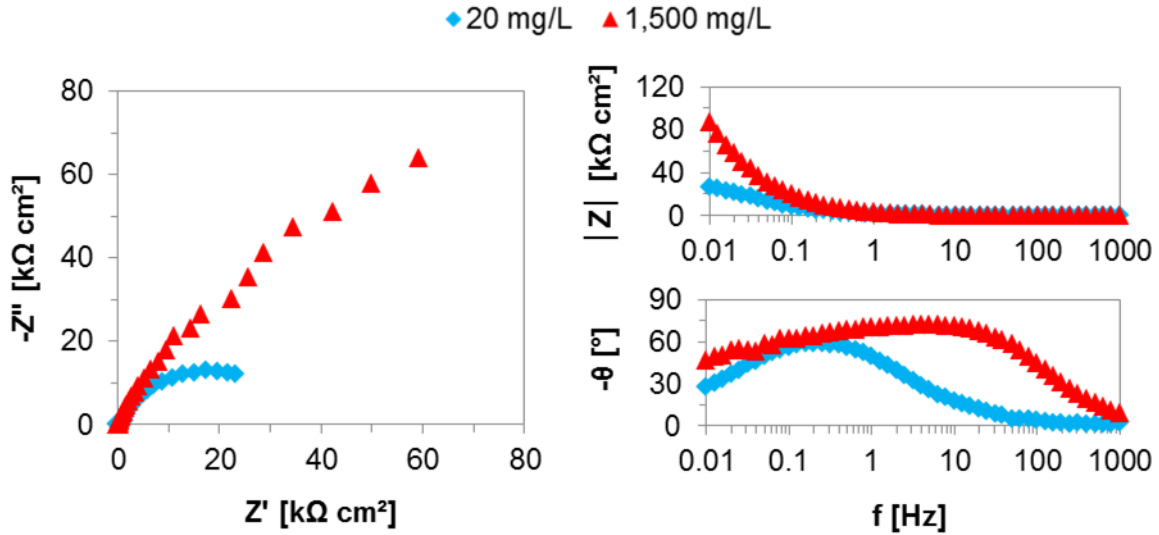


Figure 6.21 Typical impedance spectra for 1.4562 at 175 °C under E_{oc} conditions in the artificial geothermal brine containing 20 mg/L (LHD-05) and 1,500 mg/L (SBY) chlorides

Table 6.9 Electrochemical data obtained by EIS for 1.4562 at 175 °C under E_{oc} in the artificial geothermal brine containing 20 mg/L (LHD-05) and 1,500 mg/L (SBY) chlorides

$c(\text{Cl}^-)$ [mg/L]	R_s [Ω]	R_1 [kΩ cm ²]	Q_1 [mS s ^α /cm ²]	α_1	C_1 [μF/cm ²]	R_2 [kΩ cm ²]	Q_2 [mS s ^α /cm ²]	α_2	C_2 [μF/cm ²]
20	76	37	0.16	0.784	84	-	-	-	-
1,500	7	10	0.05	0.878	22	358	0.028	0.516	0.1

In the solution containing 20 mg/L chlorides only one layer was detected during the frequency scan and it could be linked to the double layer. The resistance associated to that capacitance was probably the resistance to the charge transfer across the double layer. Since the outer layer, formed in the solution with 1,500 mg/L chlorides, showed similar characteristics, it was possible to directly compare the corrosion behavior of the material in the solutions with different salt content. Accordingly, due to the higher R_1 in the less concentrated conditions, lower charge transfer rate was expected. However, in addition to the double layer, in the solution containing 1,500 mg/L chlorides a thick and compact passive layer was evolved. Its resistance R_2 was up to one order of magnitude higher than the resistance R_1 of the double layer formed in the less concentrated conditions. This could lead to the conclusion that the rate limiting step in the electrode dissolution in the solution containing more salts was the diffusion of ionic species through the inner layer.

Consequently, the electrode dissolution rate could be lower in the latter conditions despite the lower charge transfer resistance. In order to determine the corrosion rates in both conditions and support the aforementioned assumption, exposure tests were performed. Their results are shown in the further text below.

6.5.1.3 Determination of critical potentials and pits characterization

Typical cyclic polarization curves obtained for 1.4562 at 175 °C in the artificial geothermal brine containing 20 mg/L (LHD-05) and 1,500 mg/L (SBY) chlorides, respectively, are presented in Figure 6.22. The electrochemical data determined from the curves are shown in Table 6.10. Shift of the E_{oc} in the more active and the E_{pit} to the nobler direction resulted in wider passive range in the solution containing less chloride. However, passive current was much larger indicating higher dissolution rate of the surface layer. This could be ascribed to the higher oxygen concentration present in the LHD-05 solution, leading to an increase of the cathodic and thus, anodic dissolution rate, corroborated by the more active E_{oc} . In contribution to this speaks an observed hump in the current density on the forward scan of the anodic polarization curve, at approximately 350 mV. Such feature was observed in the same conditions on the surface of 1.4404. It was most probably caused by the oxidation of ferrous (Fe^{2+}) to ferric ions (Fe^{3+}) (Equation (2.5)).

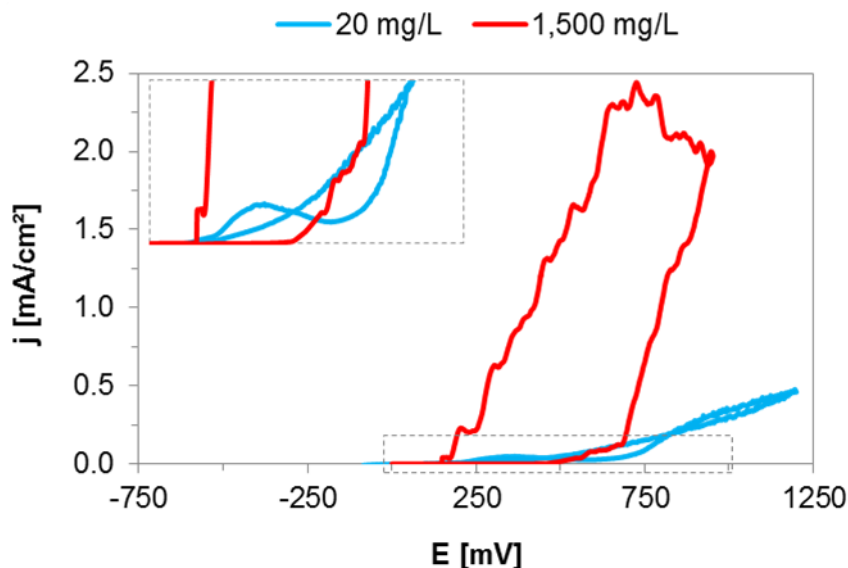


Figure 6.22 Typical cyclic polarization curves of 1.4562 at 175 °C in the artificial geothermal brine containing 20 mg/L (LHD-05) and 1,500 mg/L (SBY) chlorides, respectively

A very mild slope of the current density increase extending until the transpassive region was observed on the polarization curve recorded in the solution containing 20 mg/L chlorides. Extremely narrow negative hysteresis and the small difference between the E_{rep}

and E_{pit} indicated to the quick repassivation of the slightly perturbed surface. Therefore, 1.4562 was considered to have excellent repassivation capability in LHD-05 at 175 °C. On the other hand, the electrode surface in the solution containing more chlorides was susceptible to pitting corrosion already at the potentials 200 mV more positive than the corresponding E_{oc} . This was indicated by the relatively steep curve slope on the forward scan. The reason was the more profound attack on the active sites and surface defects by the higher chloride concentration. Chlorides adsorbed onto the sites, penetrated through the passive film and attacked the bare electrode surface. Therefore, the large and wide negative hysteresis observed on the backward scan in the solution containing 1,500 mg/L chlorides implied to the significant surface disruption due to the pits formation. Repassivation ability was thus, in the latter conditions, significantly reduced, indicated by the more negative E_{rep} than the corresponding E_{oc} . Moreover, such observation implied also to the possibility of metastable pitting to occur in normal stagnant service conditions.

Table 6.10 Electrochemical data of 1.4562 determined from cyclic polarization at 175 °C in the solution containing 20 mg/L (LHD-05) and 1,500 mg/L (SBY) chlorides

$c(\text{Cl}^-)$ [mg/L]	E_{oc} [mV]		E_{rep} [mV]		E_{pit} [mV]	
20	94	– 114	616	– 640	743	– 758
1,500	314	– 415	182	– 271	523	– 656

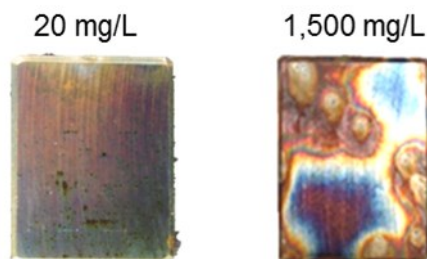


Figure 6.23 Appearance of 1.4562 electrodes after the cyclic polarization test at 175 °C in the artificial geothermal brine containing 20 mg/L (LHD-05) and 1,500 mg/L (SBY) chlorides

Surface discoloration was apparent in both conditions on the electrodes surface (Figure 6.23). It had a more uniform and smoother distribution in the solution containing less chloride, indicating the lower presence of the preferentially dissolved local sites. This was also supported by the fact that no pits were found on the surface, only some light deposits (Figure 6.24). On contrary, pitting corrosion in the solution with higher chloride content was obviously initiated. Significant surface discoloration and substantial amount and size of the

pits speak in contribution, once again proving a profound effect of the chlorides on the initiation of pitting corrosion.

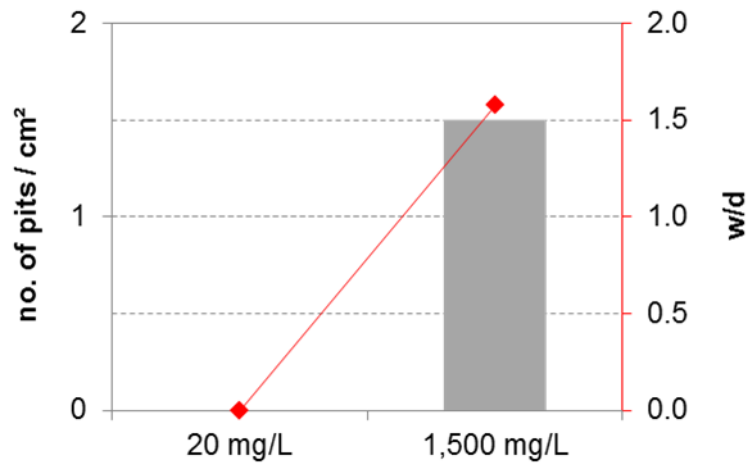


Figure 6.24 Average amount and width-to-depth ratio of the pits observed on 1.4562 electrodes after cyclic polarization at 175 °C in artificial geothermal brine containing 20 mg/L (LHD-05) and 1,500 mg/L (SBY) chlorides, respectively

Table 6.11 Characterization of the pits observed on 1.4562 electrode surface after the cyclic polarization test at 175 °C in the artificial geothermal brine containing 20 mg/L (LHD-05) and 1,500 mg/L (SBY) chlorides, respectively

c(Cl ⁻) [mg/L]	no. of pits / cm ²	width [μm]		depth [μm]	
20	0	0	± 0	0	± 0
1,500	2	393	± 193	234	± 136

6.6 Investigation of crevice corrosion susceptibility

The susceptibility to crevice corrosion of alloy 1.4562 was investigated at 100 °C in the artificial SBY geothermal brine using a rubber pad (Figure 3.7: B). The results of cyclic polarization in the conditions with and without the simulated crevice were compared and presented in Figure 6.25 and Table 6.12.

Irrespective of the crevice presence, extremely stable surface passivity, extending over a wide potential range, was observed from the cyclic polarization curves. Slightly higher passive current densities were seen on the electrode containing simulated crevice. Such observation suggested higher uniform dissolution rates compared to the system without the crevice as shown in the Figure 6.26. Furthermore, the E_{pit} shifted to the more active values, implying to an earlier initiation of localized corrosion, which is in

agreement with the results of several different authors.^{35,188,189} Reversing the polarization scan in the cathodic direction, extremely narrow negative hysteresis was apparent, suggesting slight surface disruption due to the anodic polarization. Accordingly, the surface showed an excellent repassivation capability of the perturbed sites.

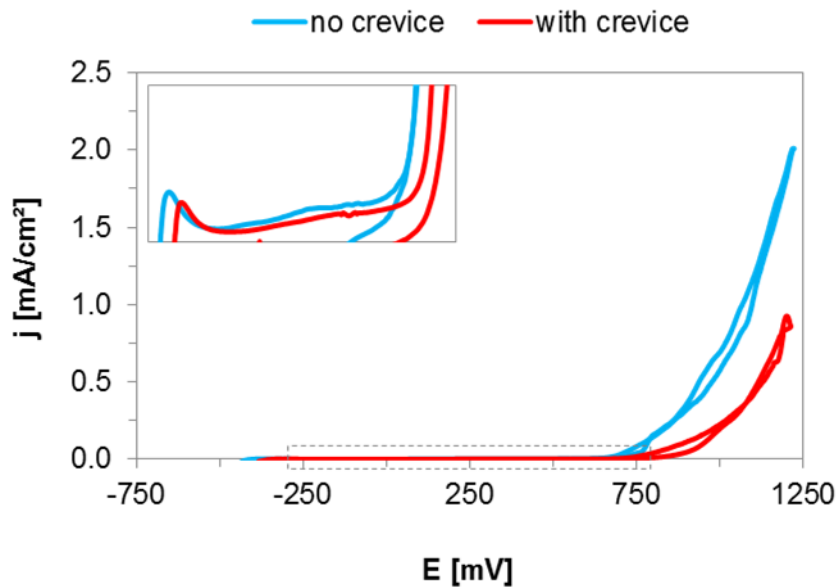


Figure 6.25 Typical cyclic polarization curve of 1.4562 in the artificial SBY geothermal brine at 100 °C with and without the crevice simulation, respectively

Table 6.12 Electrochemical data of 1.4562 determined from the cyclic polarization in the artificial SBY geothermal brine at 100 °C with and without the crevice simulation

	E_{oc} [mV]		E_{rep} [mV]		E_{pit} [mV]	
no crevice	-220	-181	869	891	932	951
with crevice	-120	-113	609	868	782	937

Visually expecting the electrode surface after the cyclic polarization test, serious corrosion was observed on the surface area where the crevice had been simulated (Figure 6.26). The evidence of the severity of the corrosion attack was the uniform removal of 3 μm deep surface layer along the entire width of the electrode and the presence of the grain boundaries. Obviously, a breakdown of the, generally, very stable and resistant passive chromium (III) layer occurred. Such finding led to the conclusion that in some point oxygen free conditions with critical acidity arose, which retarded the repassivation of the surface and caused high uniform dissolution rates, agreeing with the theories existing on this topic.^{35,188-193} Accordingly, alloy 1.4562 was susceptible to crevice corrosion in the artificial SBY geothermal brine at 100 °C under stagnant conditions.

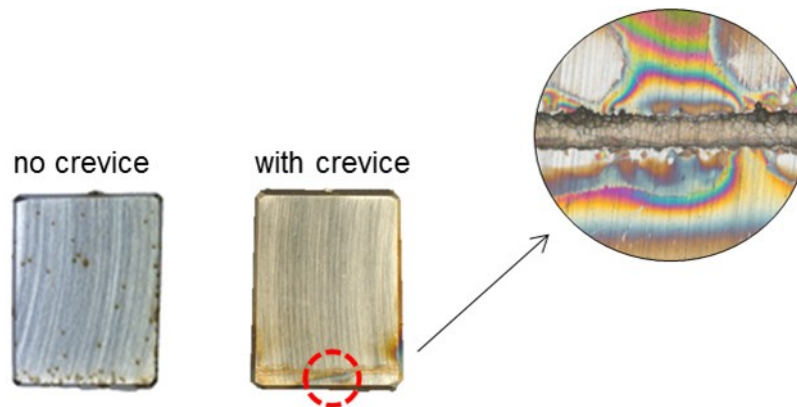


Figure 6.26 Appearance of 1.4562 electrode after the cyclic polarization in the artificial SBY geothermal brine at 100 °C with and without the crevice simulation, respectively

6.7 Investigation of stress corrosion cracking susceptibility

U-bent specimens (Figure 3.7: C) of high-alloyed stainless steel 1.4562 were exposed for 6 months in the artificial geothermal brine at 175 °C in order to determine the susceptibility of the alloy to stress corrosion cracking (SCC). Since the pitting corrosion, the main precursor for SCC, was found only on the flat coupons surface exposed in the artificial LHD-23 geothermal brine, the experiments were conducted in the latter conditions.

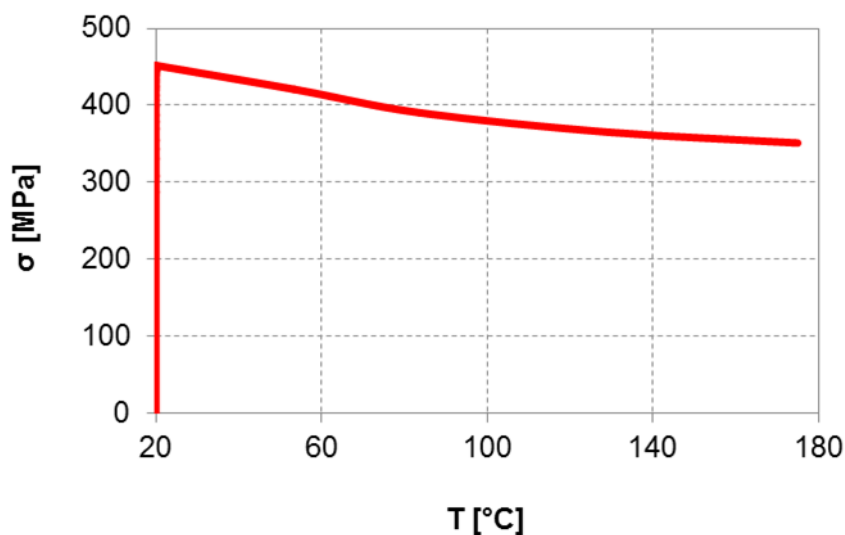


Figure 6.27 Surface relaxation of 1.4562 coupons with temperature application

In Figure 6.27 dependence of the stress, present on the coupons surface, on the applied temperature, calculated with ANSYS Workbench Mechanical computer software, is shown. The surface was approximately linearly relaxed with temperature increase. However, due to the high strength and low thermal expansion coefficient of the material, rather high stresses were present on the tension stretched surface even after exposing the specimen to

175 °C (Figure 6.28). Such behavior implied to the possibly high susceptibility to crack initiation once the pitting corrosion onsets.⁹⁷

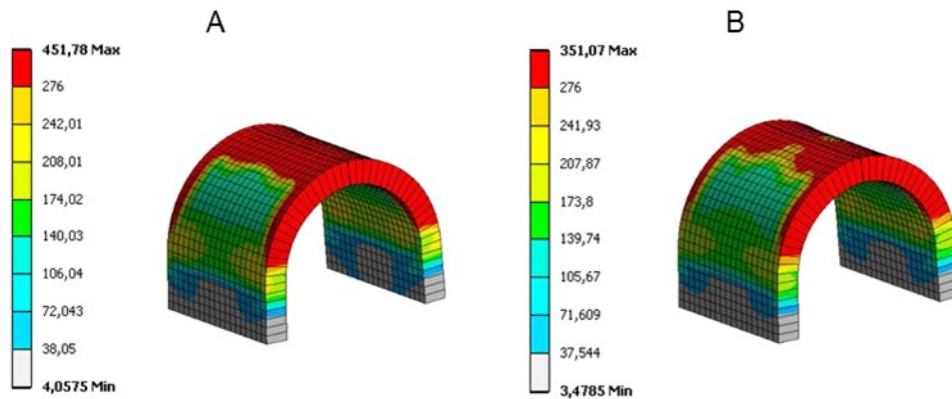


Figure 6.28 Calculated tensile stress on the surface of 1.4562 U-bend coupon at 20 °C (A) and 175 °C (B), respectively

Exposing the plastically deformed coupons for 6 months in the LHD-23 artificial geothermal brine, revealed numerous small pits on the surface (Figure 6.29: A), but none of them acted as crack initiation sites (Figure 6.29: B). However, it is not excluded that during the subsequent exposure time the cracks would not initiate from the previously formed pits.

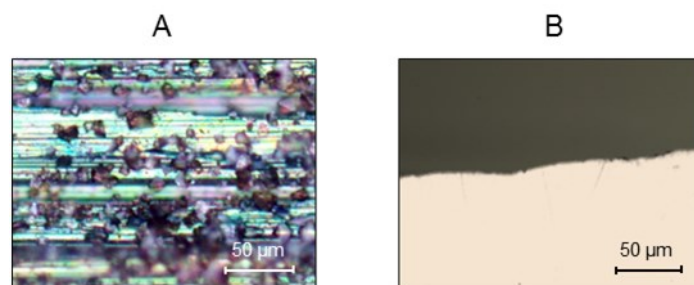


Figure 6.29 Surface (A) and cross section (B) of U-bend 1.4562 steel coupons after 6 months of exposure at 175 °C in the artificial LHD-23 geothermal brine

Chapter 7

Summary

The summary of the results obtained with electrochemical methods and exposure tests in different conditions (temperature, pH, salt concentration) is depicted in Figure 7.1 and Table 7.1, respectively. Based on the set out facts in the previous chapters, the following could be summarized:

- i. Time factor had a positive influence on the selected materials performance; a thicker and more stable corrosion film evolved on the metal surface. Low-alloyed steel 1.7218 exhibited uniform dissolution mainly of iron from the metal matrix, forming a two-layered corrosion film. Considering its stability with time, it was composed mostly of ferric compounds, which acted as a barrier between the metal and the corrosive environment, indicated by the reduction in the corrosion rate. Stainless steel 1.4404 and high-alloyed stainless steel 1.4562 exhibited excellent resistance to uniform corrosion due to the formation of a several nm thick, transparent passive film on their surface.
- ii. Increase in the temperature of the system showed variable effect on the corrosion performance of the materials. At 100 °C the corrosion rate of 1.7218 steel reached a maximum among the investigated temperatures, whilst at 175 °C the rate significantly decreased. It was concluded that such behavior was caused by the difference in the oxygen content and the system pressure; existence of only traces of oxygen in the solution at 100 °C impaired the formation of stable ferric oxides on the metal surface. However, temperature increase to 175 °C of the closed system resulted in increased oxygen solubility and formation of stable

oxides on the metal surface. Furthermore, dielectric constant of the medium was reduced causing lower solution conductivity. On the other hand, the corrosion resistance of 1.4404 and 1.4562 steels continuously decreased with temperature. Moreover, an increased susceptibility to pitting corrosion was observed as well. This led to the conclusion that the dissolution rate of the passive layer, migration rate of the aggressive ionic species toward and through the layer and their chemisorption on the metal surface increased with temperature, leading to the sooner breakdown of the protective passive layer.

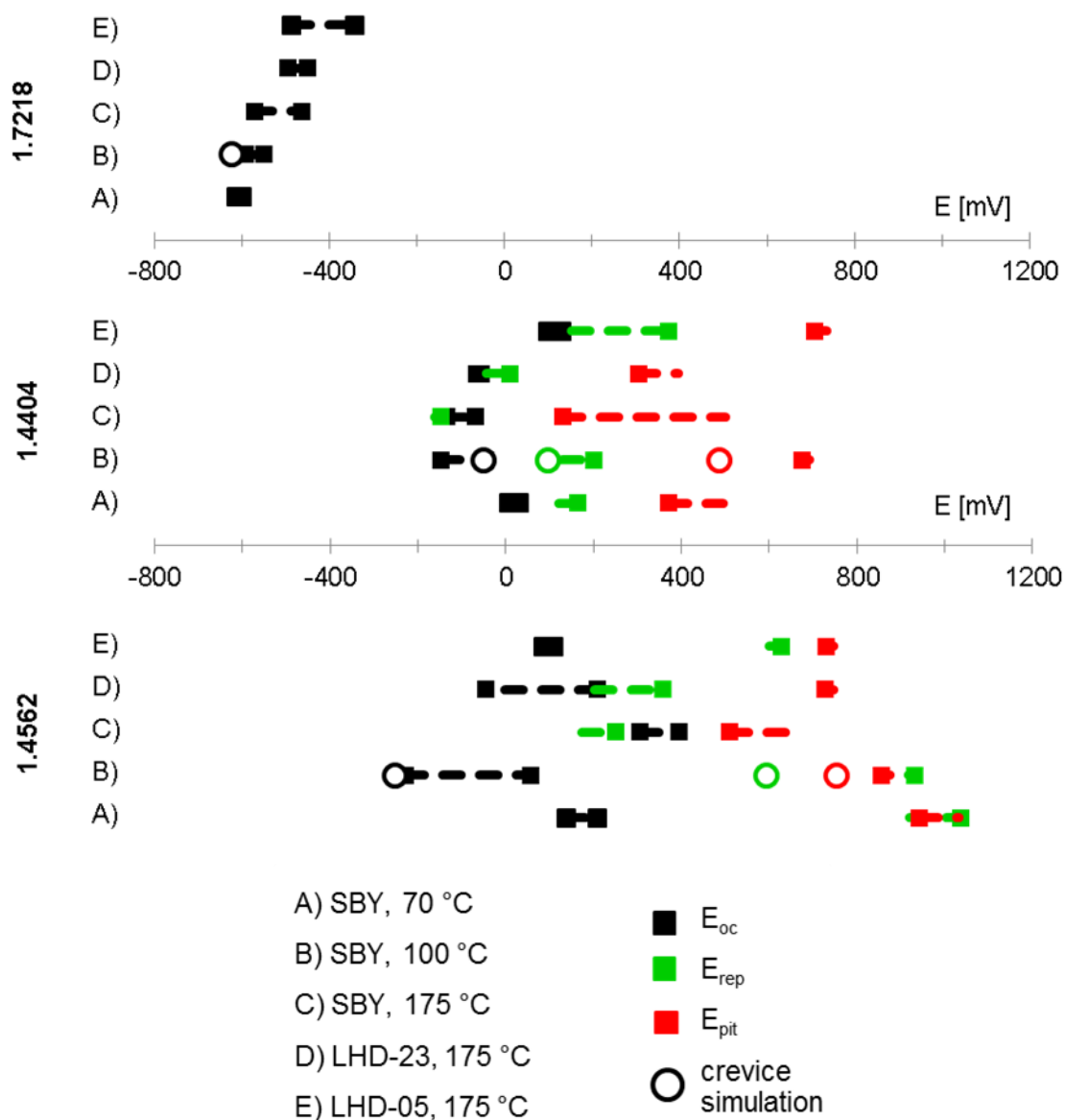


Figure 7.1 Overview and comparison of the results obtained with electrochemical methods for the selected materials 1.7218, 1.4404 and 1.4562 in the artificial geothermal brines

- iii. Increase of the solution acidity exhibited the most profound negative influence on the corrosion performance of all three selected materials among the investigated factors. The dissolution rate of 1.7218 coupons was significantly accelerated in pH 2 conditions, without the possibility of a stable film formation on the metal surface. Similar, substantial reduction in the resistance of the passive layers on 1.4404 and 1.4562 was observed, especially in case of 1.4404 steel, indicating greater general dissolution rates. Such behavior was clearly attributed to the increased concentration of the hydrogen ions present in the solution with higher acidity, which were the main species driving the cathodic reaction. However, one of the most noteworthy issues that needed understanding was the ennoblement of the pitting potentials with pH decrease. This was linked to the higher sulphate-to-chloride ratio present in pH 2 solution that caused an inhibitive effect to the localized corrosion initiation, as suggested in the literature.¹⁸⁵⁻¹⁸⁷ Nevertheless, once the pits initiated, the surface was even more severely disrupted than in the less acidic conditions due to the higher concentration of aggressive ionic species responsible for localized corrosion.
- iv. Increase in the salt concentration had a profound effect only on the highly alloyed materials. The surface of low-alloyed steel 1.7218 corroded with lower rates compared to the surface exposed in the more diluted solution. Such behavior was linked to the “salting out” phenomenon that occurred in the more concentrated solution.¹⁷⁷⁻¹⁷⁹ Lower oxygen content impeded the cathodic reaction rate, resulting in a lower metal anodic dissolution rate. Concerning 1.4404 and 1.4562 steels, an excellent resistance to uniform corrosion was shown, as expected. However, more active pitting potentials were observed, indicating sooner onset of pitting corrosion. This was clearly linked to the higher amount of chlorides present in the more concentrated solution, which are considered the main ionic species responsible for localized attack.
- v. Investigating the crevice corrosion susceptibility revealed a high vulnerability of highly alloyed steels to the presence of shielded areas. Low-alloyed steel 1.7218 did not show any significant change in the surface appearance. Conversely, both 1.4404 and 1.4562 steels experienced severe uniform corrosion at the occluded sites exhibiting high dissolution rates of the passive layers due to the oxygen depletion and formation of critical acidity in the crevice. Such behavior proved higher susceptibility of the higher alloyed steels to crevice corrosion.

- vi. Stress corrosion cracking (SCC), however, encountered certain limitations during the investigations. First; 1.7218 steel coupons cracked during the bending, which prevented to perform SCC testing on U-bend specimens, and second; the duration of the tests for other selected materials was too short to initiate a crack from the preformed pits. Based on these facts, it was possible to conclude only that 1.7218 steel could not withstand high amount of tensile stress due to its high strength and brittleness, caused by the relatively high amount of carbon (> 0.2 wt%). It was susceptible to mechanical cracking once the stress level exceeded the tensile strength of the material, even without any significant note of previous deformation. Also, 1.4404 and 1.4562 steels proved excellent resistance to SCC during the 6 months of exposure in the investigated conditions.

Table 7.1 Overview of the results after 6 months of exposure

Steel	Conditions		CR [mm/y]	Pitting	Note	
1.7218	SBY	T [°C]	70	0.1736	no	
			100	0.1788	no	
			175	0.0049	no	
	LHD-23	pH	2	0.0895	no	crevice corrosion at the place of fixation
	SBY		4	0.0049	no	
	LHD-05	c(Cl ⁻) [mg/L]	20	0.0172	no	
SBY	1,500		0.0049	no		
1.4404	SBY	T [°C]	70	-	-	
			100	< 0.06	no	
			175	< 0.06	no	crevice corrosion at the place of fixation
	LHD-23	pH	2	0.0759	yes	no SCC
	SBY		4	< 0.06	no	crevice corrosion at the place of fixation
	LHD-05	c(Cl ⁻) [mg/L]	20	-	-	
SBY	1,500		< 0.06	no	crevice corrosion at the place of fixation	
1.4562	SBY	T [°C]	70	-	-	
			100	< 0.06	no	
			175	< 0.06	no	
	LHD-23	pH	2	0.0042	yes	no SCC
	SBY		4	< 0.06	no	
	LHD-05	c(Cl ⁻) [mg/L]	20	-	-	
SBY	1,500		< 0.06	no		

The corrosion behavior differed significantly among the selected materials depending on the conditions in which they were exposed. Nevertheless, one was certain: steel grade 1.7218 exhibited active uniform corrosion, forming a visible two-layer film consistent of different ferric compounds on its surface. On the other hand, on the surface of

steel grades 1.4404 and 1.4562 a several nm thick, transparent passive layer formed, which provided a protection against uniform corrosion. The high chromium content in the alloys composition enabled the perfect passivation of the metal surface, and was thus, certainly the main reason for such excellent corrosion performance in most of the investigated conditions. However, the susceptibility to pitting corrosion was clearly observed, especially in the conditions with higher chloride content. More noble pitting potentials of 1.4562 compared to 1.4404 were attributed to higher molybdenum, nickel and nitrogen content, preventing the adsorption of aggressive ions on the active sites, stabilizing the austenitic structure of the alloy and reducing the chlorides oxidizing power.

Chapter 8

Conclusions & Outlook

In order to increase the competitiveness of the geothermal energy against the conventional energy resources, there is a great necessity for improving the geothermal systems; reducing the costs of the geothermal power plant construction and providing secure energy exploitation. One of the major problems that could affect a stable and continuous energy production is the corrosion of construction materials and equipment due to their interaction with an aggressive environment. Among all of the existing electric power generation facilities, corrosion is considered to be the most severe on geothermal power plants. This can be attributed to the extreme high temperature and pressure conditions present in geothermal systems, as well as the existence of almost an entire periodic system of elements in form of corrosive salts. Therefore, geothermal fluids are found to be extremely hostile for the construction material and equipment installed at geothermal power plants. If insufficient and inadequate measures for material selection are undertaken during the initial design phase of the plant, a huge risk of equipment degradation and system failure is present. This could not only lead to the reduction in the energy production, but also to the shutdown of the entire geothermal power plant.

Geothermal systems consist of various constructional units required for the power plants' operation. In order to exploit the geothermal fluid from the reservoir and transfer it to the turbine in the geothermal power plant, several hundred meters of transmission pipeline is installed, along with different equipment (separators, heat exchangers, turbine, etc.) necessary for the plants' performance. The most commonly used materials for construction

of these units are metallic materials, primarily steels, due to their excellent corrosion resistance in aggressive geothermal environments, appropriate mechanical properties and lower cost compared to other materials.

This research was triggered by the corrosive conditions on the geothermal fields Sibayak and Lahendong – “hotspots” of Indonesia, the country with the highest geothermal potential in the world. The main objective was to evaluate which of the steel materials currently available on the market could overcome the problem of corrosion and withstand highly aggressive conditions during the exploitation of geothermal resources in volcanic environments. It was also set out to investigate the alloys susceptibility to different types of corrosion attacks using appropriate test setups, and to study the mechanisms of their occurrence. Furthermore, the study has sought to understand the impact of different factors on the corrosion performance of the selected materials and their integrity, due to the complexity and common instability of the geothermal systems. This way the probability of the material failure would be minimized and a “safer operating window” of power plants would be achieved.

The summary of the results obtained with electrochemical methods and exposure tests is shown in Table 8.1. It was shown that low-alloyed steel 1.7218 is suitable for all of the investigated conditions except in low pH brine. The susceptibility to mechanical cracking due to its hardness could present a major obstacle in its application considering the high stresses present in geothermal power plants during the operation conditions. Austenitic stainless steel 1.4404 showed remarkable resistance to uniform corrosion in most of the investigated conditions. However, its major disadvantage is its susceptibility to localized corrosion. The integrity of the system made of this type of steel could be severely disrupted in low pH and high chloride conditions, especially in the presence of high temperatures. Austenitic high-alloyed steel 1.4562 exhibited excellent resistance to uniform and a very good resistance to pitting corrosion, even in low pH conditions. It is therefore considered to be suitable in all of the investigate conditions. However, major attention should be paid in systems where crevices at the metal/polymer connections are possible to occur.

The main application of the achieved results in this research is certainly in geothermal systems, where a sustainability and integrity of the construction materials are of great importance for the secure and reliable plant operation. Despite the same behavioral pattern of the selected materials that has already been shown in a wide literature review, this study allows a detailed insight into the corrosion performance of the alloys in particular geothermal environments. It also allows a prediction of the performance of other alloys with different chemical composition in the similar conditions. Furthermore, the change in the

materials behavior where the stability of the system is difficult to foresee has also been covered, enabling a construction of different plant units from distinctive materials, depending on the constructor’s needs. Indeed, the results are also transferable to applications other than the geothermal, as long as the environmental conditions, to which the materials are being exposed, are comparable.

Table 8.1 Results summary matrix of the performed experiments and their evaluation

Method	Conditions		1.7218	1.4404	1.4562	
Electrochemistry	Temperature [°C]	70				worse
		100				
		175				
	pH	2				
		4				
	Salt concentration [mg/L]	20				
		1,500				
Crevice corrosion						middle
Method	Conditions		1.7218	1.4404	1.4562	
Exposure	Temperature [°C]	70				best
		100				
		175				
	pH	2				
		4				
	Salt concentration [mg/L]	20				
		1,500				
Stress corrosion cracking						

Additional elements that would have provided further insight into the problems and present a complete picture of the studied problem were unfortunately not possible to conduct due to the limited amount of time within this project. Several recommendations, presented below, could complement the set of results presented in this research thesis. The list of recommendations for further work is following:

- i. It is recommended to investigate the influence of the geothermal brine flow on the corrosion performance of the selected materials since geothermal power plants are more than 90 % of their lifetime in operation.^{2,5,14,37,145,198-201}
- ii. Silica content in the brine should be considered due to its abundance in geothermal systems and possible counter effect to corrosion of the construction materials, considering its precipitation on the walls of the pipeline.^{10,12,14,17}

- iii. It is advised to perform stress corrosion cracking (SCC) testing using the slow strain rate method to accelerate the time to failure. Also, determination of critical potential range where the alloy is the most vulnerable to SCC is recommended using electrochemical potentiodynamic methods.^{97,202}
- iv. On-site testing in the real operation conditions is strongly recommended to confirm the reliability of the results obtained in the artificial conditions, and, if needed, to generate and develop new strategies and methods in the laboratory investigations to improve the off-site testing reliability.

Appendix A

Literature

1. Lund, J. W., D. H. Freeston and T. L. Boyd (2011). Direct utilization of geothermal energy 2010 worldwide review. *Geothermics* 40 (3) 159-180.
2. Rybach, L. (2010). Status and prospects of geothermal energy. World Geothermal Congress 2010, Bali, Indonesia.
3. Bertani, R. (2012). Geothermal power generation in the world 2005–2010 Update report. *Geothermics* 41 1-29.
4. Radja, V. T. (1995). The Role of Geothermal Energy in the Context of the Future Electric Power Supply in Indonesia. World Geothermal Congress 1995, Florence, Italy.
5. Mongillo, M. A., C. J. Bromley and L. Rybach (2010). The IEA Geothermal Implementing Agreement-International Efforts to Promote Global Sustainable Geothermal Development and Help Mitigate Climate Change. World Geothermal Congress 2010, Bali, Indonesia.
6. Sasradipoera, D. S. and D. Hantono (2003). Strategies for developing Lahendong geothermal field, Indonesia. Twenty-Eighth Workshop on Geothermal Reservoir Engineering, Stanford University, Stanford, California.
7. Zaidi, S. H. (2010). Geothermal Energy for Sustainable Development: An Expanded Role in Indonesia's Energy Supply Chain. World Geothermal Congress 2010, Bali, Indonesia.

8. Rybach, L. (2007). Geothermal sustainability. European Geothermal Congress, Unterhaching, Germany.
9. Stapleton, M. (2002). Scaling and Corrosion in Geothermal Operation. Nevada, USA, PowerChem Technology.
10. Baticci, F., et al. (2010). Corrosion and Scaling Detection in the Soultz EGS Power Plant, Upper Rhine Graben, France. World Geothermal Congress 2010, Bali, Indonesia.
11. Muller, J., et al. (2010). Laboratory Results of Corrosion Tests for EGS Soultz Geothermal Wells. World Geothermal Congress 2010, Bali, Indonesia.
12. Lichti, K. A. and R. H. Julian (2010). Corrosion and Scaling in High Gas (25 wt%) Geothermal Fluids. World Geothermal Congress 2010, Bali, Indonesia.
13. Lichti, K. A., et al. (2010). Acid Well Utilisation Study: Well MG-9D, Philippines. World Geothermal Congress 2010, Bali, Indonesia.
14. Stănăşel, I. (2010). Control of Corrosion and Scaling in Selected Geothermal Wells from Romania. World Geothermal Congress 2010, Bali, Indonesia.
15. Daco-ag, L. M., et al. (2010). Testing a Low Temperature Application Corrosion Inhibitor in the Upper Mahiao Power Plant Condensates. World Geothermal Congress 2010, Bali, Indonesia.
16. Conover, M., P. Ellis and A. Curzon (1980). Material Selection Guidelines for Geothermal Power Systems - An Overview. Geothermal Scaling and Corrosion: Symposia, New Orleans, LA, ASTM International.
17. Carter, J. P. and S. D. Cramer (1992). Materials of construction for high-salinity geothermal brines. U.S. Bureau of Mines.
18. Rafferty, K. D. (1998). Piping. Oregon, USA, Oregon Institute of Technology.
19. Aksoy, N. and U. Serpen (2010). Acidizing in Geothermal Wells and HCl Corrosion. World Geothermal Congress 2010, Bali, Indonesia.
20. McCawley, F. X. and J. P. Carter (1978). Materials for use in corrosive geothermal brine environments. Austin, TX, Bureau of Mines, College Park, MD.
21. Brehme, M. (2010). Lahendong geothermal field: fluid analysis 2010 (internal report). Potsdam, Germany, GFZ.

22. Brehme, M. (2011). Lahendong geothermal field: fluid analysis 2011 (internal report). Potsdam, Germany, GFZ.
23. Brehme, M., et al. (2013). Hydrochemical patterns in a structurally controlled geothermal system. *Mineralogical Magazine*.
24. Brehme, M., et al. (2014). A hydrotectonic model of a geothermal reservoir – A study in Lahendong, Indonesia. *Geothermics* 51 228-239.
25. Stáhl, G., et al. (2000). Study of calcite scaling and corrosion processes in geothermal systems. *Ibid.* 29 (1) 105-119.
26. Bäßler, R., et al. (2009). Evaluation of corrosion resistance of materials for geothermal applications. *NACE Corrosion 2009*. Atlanta, GA.
27. Klapper, H. S., et al. (2012). Evaluation of Suitability of High-Alloyed Materials for Geothermal Applications in the North German Basin. *Corrosion* 68 (1) 016001-016001-016001-016009.
28. Klapper, H. S., et al. (2011). Evaluation of Suitability of Some High-Alloyed Materials for Geothermal Applications. *NACE Corrosion 2011*. Houston, TX.
29. Kairi, N. I. and J. Kassim (2013). The Effect of Temperature on the Corrosion Inhibition of Mild Steel in 1 M HCl Solution by Curcuma Longa Extract. *Int. J. Electrochem. Sci* 8 7138-7155.
30. Vuppu, A. K. and W. P. Jepson (1994). The effect of temperature in sweet corrosion of horizontal multiphase carbon steel pipelines. SPE Asia Pacific Oil and Gas Conference, Society of Petroleum Engineers.
31. Klapper, H. S., D. Laverde and C. Vasquez (2008). Evaluation of the corrosion of UNS G10200 steel in aerated brines under hydrodynamic conditions. *Corrosion Science* 50 (9) 2718-2723.
32. Stoullil, J., et al. (2013). Influence of temperature on corrosion rate and porosity of corrosion products of carbon steel in anoxic bentonite environment. *Journal of Nuclear Materials* 443 (1–3) 20-25.
33. Tskhvirashvili, D., O. Vardigoreli and P. Acolsin (1972). On corrosion of metals in geothermal power plants. *Geothermics* 1 (3) 113-118.
34. Abd El Meguid, E. A. and A. A. Abd El Latif (2007). Critical pitting temperature for Type 254 SMO stainless steel in chloride solutions. *Corrosion Science* 49 (2) 263-275.

35. Szklarska-Smialowska, Z. (2005). *Pitting and crevice corrosion*. Houston, TX: NACE International.
36. Brondel, D., et al. (1994). Corrosion in the oil industry. *Oilfield review* 6 (2) 4-18.
37. Prasetia, A. E., A. T. N. Salazar and J. S. S. Toralde (2010). Corrosion Control in Geothermal Aerated Fluids Drilling Projects in Asia Pacific. World Geothermal Congress 2010, Bali, Indonesia.
38. Magaly, F. A., et al. (2010). The Neutralization of Acid Fluids: an Alternative of Commercial Exploitation Wells on Los Humeros Geothermal Field. World Geothermal Congress, Bali, Indonesia.
39. Revie, R. W. (2000). *Uhlig's Corrosion Handbook*. 2nd ed: John Wiley & Sons.
40. Thomas, J. G. N. (1961). Kinetics of electrolytic hydrogen evolution and the adsorption of hydrogen by metals. *Transactions of the Faraday Society* 57 1603-1611.
41. Ningshen, S., et al. (2006). Hydrogen effects on the passive film formation and pitting susceptibility of nitrogen containing type 316L stainless steels. *Corrosion Science* 48 (5) 1106-1121.
42. Guo, L. Q., et al. (2013). Effect of hydrogen on pitting susceptibility of 2507 duplex stainless steel. *Corrosion Science* 70 140-144.
43. Yu, J. G., J. L. Luo and P. R. Norton (2002). Investigation of hydrogen induced pitting active sites. *Electrochimica Acta* 47 (25) 4019-4025.
44. Khatak, H. S. and B. Raj (2002). *Corrosion of austenitic stainless steels: mechanism, mitigation and monitoring*: Woodhead publishing.
45. Sedriks, A. J. (1996). *Corrosion of Stainless Steels*: Wiley.
46. McGuire, M. F. (2008). *Stainless steels for design engineers*: ASM International.
47. Fridleifsson, I. B., et al. (2008). The possible role and contribution of geothermal energy to the mitigation of climate change. IPCC scoping meeting on renewable energy sources, Luebeck, Germany.
48. Bailey, C. and J. Kerkman. (1999). *Geothermal Energy: The Alternative of the Future [online]*. Honors Colloquium: Clarke University.

49. Bromley, C. J., M. Mongillo and L. Rybach (2006). Sustainable utilization strategies and promotion of beneficial environmental effects—Having your cake and eating it too. Geothermal Workshop 2006, New Zealand.
50. Armannsson, H. (2003). CO₂ emission from geothermal plants. International Geothermal Conference, Reykjavik, Iceland, Geothermal Association of Iceland.
51. Geothermal Technologies Office. <http://www1.eere.energy.gov/geothermal> [online]: U.S. Department of Energy [Accessed 28.09.2012.].
52. Bloomfield, K. K., J. N. Moore and R. N. Neilson (2003). Geothermal energy reduces greenhouse gases. *Geothermal Resources Council Bulletin* 32 (2) 77-79.
53. Alternative Energy Management. <http://exergy.se/goran/cng/alten/proj/98/geothermal/geo.htm> [online] [Accessed 16.10.2012.].
54. Kagel, A., D. Bates and K. Gawell (2007). A Guide to Geothermal Energy and the Environment. Geothermal Energy Association.
55. DiPippo, R. (2012). *Geothermal power plants: principles, applications, case studies and environmental impact*. 2nd ed: Butterworth-Heinemann.
56. Environmental Protection Agency. <http://www.freerepublic.com/focus/chat/2857328/posts> [online] [Accessed 17.03.2013].
57. REN21, Paris Secretariat (2011). *Renewables 2011: Global Status Report*. Secretariat Renewable Energy Policy Network for the 21st Century (REN21) Paris.
58. Maluegha, B. L. (2010). Calculation of gross electrical power from the production wells in Lahendong geothermal field in North Sulawesi, Indonesia. Perth, Australia, Murdoch University.
59. US Environmental Protection Agency. <http://www.epa.gov/climatestudents/solutions/technologies/geothermal.html> [online] [Accessed 15.03.2012.].
60. Sukhyar, R., et al. (2010). Geothermal Energy Update: Geothermal Energy Development and Utilization in Indonesia. World Geothermal Congress 2010, Bali, Indonesia.
61. Fauzi, A., S. Bahri and H. Akuanbatin (2000). Geothermal development in Indonesia: An overview of industry status and future growth. World Geothermal Congress 2000, Beppu-Morioka, Japan.

62. Koestono, H. (2010). Lahendong Geothermal Field, Indonesia: Geothermal Model Based on Wells LHD-23 and LHD-28. *Geothermal Training Programme*. Reykjavik, Iceland.
63. Enerdata (2011). Trends in global energy efficiency 2011: Indonesia Energy efficiency report.
64. Jaya, M. (2011). Notes & Summary: Indonesia Visit to PGE, BPPT, ITB, Wika Jabar Power, Star Energy (Wayang Windu), Batan, Dinas ESDM (internal report). Potsdam, Germany, GFZ.
65. Siregar, P. H. H. (2004). Optimization of electrical power production process for the Sibayak geothermal field, Indonesia. *Geothermal Training Programme*. Reykjavik, Iceland.
66. Hochstein, M. P. and S. Sudarman (2008). History of geothermal exploration in Indonesia from 1970 to 2000. *Geothermics* 37 (3) 220-266.
67. Harun, M. and T. Dwikorianto (2000). Interference test of Sibayak geothermal field North Sumatra, Indonesia. Stanford Geothermal Workshop Stanford, Stanford, CA.
68. Yani, A. (2006). Numerical modelling of Lahendong geothermal system, Indonesia. *Geothermal Training Programme*. United Nations University.
69. Indonesia Power Generation. <http://repit.files.wordpress.com/2011/09/lahendong.pdf> [online] [Accessed 14.05.2012.].
70. Nugroho, A. J. (2007). Evaluation of waste brine utilization from LHD unit III for electricity generation in Lahendong geothermal field, Indonesia. *Geothermal Training Programme*. Reykjavik, Iceland.
71. Hance, C. N. (2005). Factors Affecting Costs of Geothermal Power Development. U.S. Department of Energy.
72. Huenges, E. and P. Ledru (2010). *Geothermal Energy Systems: Exploration, Development, and Utilization*: John Wiley & Sons.
73. Tolivia, E. M. (1970). Corrosion measurements in a geothermal environment. *Geothermics* 2, Part 2 1596-1601.
74. Brockenbrough, R. L. and F. S. Merritt (2011). *Structural steel designer's handbook*. 5th ed: McGraw-Hill.

75. Rodriguez, J. J. S., F. J. S. Hernandez and J. E. G. Gonzalez (2002). Mathematical and electro-chemical characterisation of the layer of corrosion products on carbon steel in various environments. *Corrosion Science* 44 (11) 2597-2610.
76. Bartoň, K. and V. Marek (1970). Einfluß des entstehenden Rostes auf den Verlauf der atmosphärischen Korrosion von Stahl. *Materials and Corrosion* 21 (3) 182-184.
77. Groysman, A. (2010). *Corrosion for everybody*: Springer.
78. Cornell, R. M. and U. Schwertmann (2003). *The iron oxides: structure, properties, reactions, occurrences and uses*: John Wiley & Sons.
79. Zhang, X., et al. (2011). In situ Raman spectroscopy study of corrosion products on the surface of carbon steel in solution containing Cl(-) and SO₄(2-). *Engineering Failure Analysis* 18 (8) 1981-1989.
80. Panossian, Z., et al. (2012). Corrosion of carbon steel pipes and tanks by concentrated sulfuric acid: A review. *Corrosion Science* 58 1-11.
81. Landolt, D. (2010). *Corrosion and surface chemistry of metals*: CRC Press.
82. Olsson, C.-O. A. and D. Landolt (2003). Passive films on stainless steels - chemistry, structure and growth. *Electrochimica Acta* 48 (9) 1093-1104.
83. Kondo, M., et al. (2010). Corrosion of reduced activation ferritic martensitic steel JLF-1 in purified Flinak at static and flowing conditions. *Fusion Engineering and Design* 85 (7-9) 1430-1436.
84. Frankel, G. S. (1998). Pitting corrosion of metals. A review of the critical factors. *Journal of the Electrochemical Society* 145 (8) 2970-2970.
85. Almr, A., D. F. Bahr and M. Jacroux (2006). Effects of alloy and solution chemistry on the fracture of passive films on austenitic stainless steel. *Corrosion Science* 48 (4) 925-936.
86. Agarwal, D. C. (2004). Alloy 31: A Cost Effective Super 6Mo Alloy for Solving Corrosion Problems in the Process Industries. *NACE Corrosion 2004*. Houston, TX.
87. Klöwer, J., H. Schlerkmann and R. Popperling (2002). Corrosion behaviour of alloy 31 - UNSN08031 - under conditions of oil & gas production. *Materials and Corrosion-Werkstoffe Und Korrosion* 53 (10) 765-771.
88. Goldberg, A. (1976). Comments on the use of 316L stainless steel cladding at the geothermal Niland Test Facility. California Univ., Livermore (USA). Lawrence Livermore Lab.

89. Yang, Y., L. Guo and H. Liu (2011). The effect of temperature on corrosion behavior of SS316L in the cathode environment of proton exchange membrane fuel cells. *Journal of Power Sources* 196 (13) 5503-5510.
90. French, D. (1992). Austenitic stainless steel. *National Board Bulletin [online document]*.
91. Roberge, P. (2008). *Corrosion engineering: principles and practice*: McGraw Hill Professional.
92. Ahmad, Z. (2006). *Principles of corrosion engineering and corrosion control*: Butterworth-Heinemann.
93. Avesta Sheffield AB and AB Sandvik Steel (1994). *Avesta Sheffield Corrosion Handbook for Stainless Steels*.
94. Cottis, R. A. (2000). *Guides to Good Practice in Corrosion Control - Stress Corrosion Cracking*. HMSO.
95. Beavers, J. A., N. G. Thompson and R. N. Parkins (1985). Stress-corrosion cracking of low strength carbon steels in candidate high level waste repository environments: environmental effects. *Nuclear and chemical waste management* 5 (4) 279-296.
96. Bulloch, J. H. (2004). Some effects of yield strength on the stress corrosion cracking behaviour of low alloy steels in aqueous environments at ambient temperatures. *Engineering Failure Analysis* 11 (6) 843-856.
97. Jones, R. H. (1992). *Stress-corrosion cracking*: ASM International.
98. Blasco-Tamarit, E., D. M. Garcia-Garcia and J. Garcia Anton (2011). Imposed potential measurements to evaluate the pitting corrosion resistance and the galvanic behaviour of a highly alloyed austenitic stainless steel and its weldment in a LiBr solution at temperatures up to 150 °C. *Corrosion Science* 53 (2) 784-795.
99. Tsai, C. R., et al. (2006). An analytical solution for transport of oxygen in cathode gas diffusion layer of PEMFC. *Journal of Power Sources* 160 (1) 50-56.
100. McCafferty, E. (2010). *Introduction to corrosion science*: Springer.
101. Pyun, S.-I. and J.-W. Lee (2011). *Modern Aspects of Electrochemistry*, No. 47: Progress in Corrosion Science and Engineering II. Springer.
102. Owen, B. B., et al. (1961). The Dielectric Constant of Water As a Function of Temperature and Pressure. *The Journal of Physical Chemistry* 65 (11) 2065-2070.

103. Einarsson, K., et al. (2010). Acid Wells in the Krafla Geothermal Field. World Geothermal Congress 2010, Bali, Indonesia. World Geothermal Congress 2010, Bali, Indonesia.
104. Kaya, T., et al. (2010). Scale Inhibitor Application in KD-14 Well of Kizildere Geothermal Field. World Geothermal Congress 2010, Bali, Indonesia.
105. Floriano, W. B. and M. A. C. Nascimento (2004). Dielectric constant and density of water as a function of pressure at constant temperature. *Brazilian Journal of Physics* 34 (1) 38-41.
106. Ellis II, P. F. (1985). Companion Study Guide to Short Course on Geothermal Corrosion and Mitigation in Low Temperature Geothermal Heating Systems. Symposium on Operating Geothermal District Heating Systems & Short Course on Corrosion, Oregon Institute of Technology, Klamath Falls, OR.
107. Charng, T. and F. Lansing (1982). Review of corrosion causes and corrosion control in a technical facility. *Telecommunications and Data Acquisition Progress Report* 69 145-156.
108. Robinson, J. O. and T. O. Drews (1999). Resolving Flow-Accelerated Corrosion Problems in the Industrial Steam Plant. *NACE Corrosion* 99. San Antonio, TX.
109. Stănăşel, O. and H. Kristmannsdottir (2010). Scaling - the Main Obstacle in Efficient Use of Geothermal Fluids. World Geothermal Congress 2010, Bali, Indonesia.
110. Lichti, K. A., et al. (2010). Acid Well Utilisation Study: Well MG-9D, Philippines. World Geothermal Congress 2010, Bali, Indonesia.
111. Ramos, S. G., et al. (2010). Corrosion in Concrete Structures of the Leyte Geothermal Production Field, Philippines: Characterization and Implications. World Geothermal Congress 2010, Bali, Indonesia.
112. Valdez, B., M. Schorr and A. Arce (2006). The Influence of Minerals on Equipment Corrosion in Geothermal Brines. *International Mineral Extraction Conference*. Tucson, AZ.
113. Izquierdo, G., et al. (2000). Fluid acidity and hydrothermal alteration at the Los Humeros geothermal reservoir, Puebla, México. World Geothermal Congress 2000, Beppu-Morioka, Japan.
114. Remoroza, A. I. (2010). Corrosion Inhibition of Acid-Treated Geothermal Brine – Results from Pilot Testing in Southern Negros, Philippines. World Geothermal Congress 2010, Bali, Indonesia.

115. ASM International, A. (2005). *Corrosion: Materials*. 9 ed.
116. Mundhenk, N., et al. (2013). Corrosion and scaling as interrelated phenomena in an operating geothermal power plant. *Corrosion Science* 70 17-28.
117. Soylemezoglu, S. and R. Harper (1982). Oxygen ingress into geothermal steam and its effect on corrosion of low carbon steel at Broadlands, New Zealand. *Geothermics* 11 (1) 31-42.
118. Banaś, J., et al. (2007). Effect of CO₂ and H₂S on the composition and stability of passive film on iron alloys in geothermal water. *Electrochimica Acta* 52 (18) 5704-5714.
119. Steel database. <http://www.keytometals.com/page.aspx?ID=CheckArticle&site=kts&NM=62> [online] [Accessed 16.02.2011.].
120. Sandmeyer Steel Steel. <http://www.sandmeyersteel.com/images/316-316L-317L-Spec-Sheet.pdf> [online] [Accessed 24.04.2012.].
121. AZo Journal of Materials Online. <http://www.azom.com/article.aspx?ArticleID=2382> [online] [Accessed 07.02.2012.].
122. Heubner, U. and J. Klöwer (2003). *Nickel Alloys and High Alloy Special Stainless Steels: Properties, Manufacturing, Application*: expert-Verlag.
123. Heubner, U., R. Kirchheiner and M. Rockel (1991). Alloy 31, a new highly-alloyed nickel-chromium-molybdenum steel for the refinery industry and related applications. *Corrosion* 91 (321).
124. Rommerskirchen, I. and M. Kohler (1999). Nicrofer 3127 hMo and Nicrofer 3033 - materials offering marine corrosion resistance. Eurocorr '99, Aachen, Germany.
125. Marks, P. and W. Tirlir (2010). *Internationaler Stahlvergleich: Deutsch / Englisch*: Beuth Verlag GmbH.
126. National Technical University KhPi. http://www.steelnumber.com/en/steel_composition_eu.php?name_id=104 [online] [Accessed 24.11.2011.].
127. The Lucefin Group. http://www.lucefin.com/wp-content/files_mf/1.4404a316l70.pdf [online] [Accessed 14.10.2012.].
128. American Petroleum Institute (2010). Specification for Casing and Tubing. Washington, D.C.

129. ThyssenKrupp AG. <http://www.thyssenkrupp-nirosta.de/fileadmin/scripts/wbbreitband/de/blaetter/4404.pdf> [online] [Accessed 13.02.2012.].
130. ThyssenKrupp AG. http://www.thyssenkrupp-vdm.com/fileadmin/Downloads/Datenblaetter/de/Nicrofer3127hMo_d.pdf [online] [Accessed 13.02.2013.].
131. Kelly, R. G., et al. (2002). *Electrochemical techniques in corrosion science and engineering*: CRC Press.
132. Daub, K., et al. (2011). Oxide growth and conversion on carbon steel as a function of temperature over 25 and 80 °C under ambient pressure. *Electrochimica Acta* 56 (19) 6661-6672.
133. Hilbert, L. R. (2006). Monitoring corrosion rates and localised corrosion in low conductivity water. *Corrosion Science* 48 (12) 3907-3923.
134. Krakowiak, S., K. Darowicki and P. Ślepski (2005). Impedance of metastable pitting corrosion. *Journal of Electroanalytical Chemistry* 575 (1) 33-38.
135. Refaey, S. A. M. and G. Schwitzgebel (1998). Electrochemical impedance spectroscopic investigation of dissolution, passivation and pitting corrosion of tin in Na₂CO₃ solution and the effect of Cl⁻ and I⁻ ions. *Applied Surface Science* 135 (1-4) 243-253.
136. Sharer, Z. and J. Sykes (2012). Insights into protection mechanisms of organic coatings from thermal testing with EIS. *Progress in Organic Coatings* 74 (2) 405-409.
137. Garcia, S. J., et al. (2013). Unravelling the corrosion inhibition mechanisms of bi-functional inhibitors by EIS and SEM-EDS. *Corrosion Science* 69 346-358.
138. Hirschorn, B., et al. (2010). Determination of effective capacitance and film thickness from constant-phase-element parameters. *Electrochimica Acta* 55 (21) 6218-6227.
139. Cheng, X.-q., et al. (2011). Constituent phases of the passive film formed on 2205 stainless steel by dynamic electrochemical impedance spectroscopy. *International Journal of Minerals, Metallurgy, and Materials* 18 (1) 42-47.
140. Pell, W. G., A. Zolfaghari and B. E. Conway (2002). Capacitance of the double-layer at polycrystalline Pt electrodes bearing a surface-oxide film. *Journal of Electroanalytical Chemistry* 532 (1-2) 13-23.
141. Liu, L., et al. (2006). Electrochemical impedance spectroscopy (EIS) studies of the corrosion of pure Fe and Cr at 600 °C under solid NaCl deposit in water vapor. *Electrochimica Acta* 51 (22) 4736-4743.

142. Acciari, H. A., A. C. Guastaldi and C. M. A. Brett (2005). Corrosion of the component phases presents in high copper dental amalgams. Application of electrochemical impedance spectroscopy and electrochemical noise analysis. *Corrosion Science* 47 (3) 635-647.
143. Hamlaoui, Y., F. Pedraza and L. Tifouti (2008). Corrosion monitoring of galvanised coatings through electrochemical impedance spectroscopy. *Corrosion Science* 50 (6) 1558-1566.
144. Popova, A. and M. Christov (2006). Evaluation of impedance measurements on mild steel corrosion in acid media in the presence of heterocyclic compounds. *Corrosion Science* 48 (10) 3208-3221.
145. Chen, Y., et al. (2000). EIS studies of a corrosion inhibitor behavior under multiphase flow conditions. *Corrosion Science* 42 (6) 979-990.
146. Lasia, A., et al. (1999). Modern aspects of electrochemistry, vol. 32 Kluwer Academic. *New York* 143-248.
147. Mahato, N. and M. M. Singh (2011). Investigation of Passive Film Properties and Pitting Resistance of AISI 316 in Aqueous Ethanoic Acid Containing Chloride Ions using Electrochemical Impedance Spectroscopy (EIS). *Portugaliae Electrochimica Acta* 29 (4) 233-251.
148. Mohammadi, F., et al. (2011). EIS study of potentiostatically formed passive film on 304 stainless steel. *Electrochimica Acta* 56 (24) 8727-8733.
149. Richter, S. (2013). Factors Affecting Corrosion in Low Conductivity Geothermal Water. *NACE Corrosion 2013*. Orlando, FL, NACE.
150. Hirayama, R. and S. Haruyama (1991). Electrochemical impedance for degraded coated steel having pores. *Corrosion* 47 (12) 952-958.
151. Bonora, P. L., F. Deflorian and L. Fedrizzi (1996). Electrochemical impedance spectroscopy as a tool for investigating underpaint corrosion. *Electrochimica Acta* 41 (7-8) 1073-1082.
152. Scully, J. R., D. C. Silverman and M. W. Kendig (1993). *Electrochemical impedance: analysis and interpretation*: ASTM International.
153. Orazem, M. E. and B. Tribollet (2011). *Electrochemical impedance spectroscopy*: Wiley.

154. Brug, G. J., et al. (1984). The analysis of electrode impedances complicated by the presence of a constant phase element. *Journal of Electroanalytical Chemistry and Interfacial Electrochemistry* 176 (1-2) 275-295.
155. ASTM G102-89 (2010). Standard Practice for Calculation of Corrosion Rates and Related Information from Electrochemical Measurements. ASTM International, West Conshohocken, PA.
156. Genesca, J., et al. Conventional DC electrochemical techniques in corrosion testing.
157. Kapałka, A., G. Fóti and C. Comninellis (2008). Determination of the Tafel slope for oxygen evolution on boron-doped diamond electrodes. *Electrochemistry Communications* 10 (4) 607-610.
158. Zhang, X. L., et al. (2009). Effects of scan rate on the potentiodynamic polarization curve obtained to determine the Tafel slopes and corrosion current density. *Corrosion Science* 51 (3) 581-587.
159. McCafferty, E. (2005). Validation of corrosion rates measured by the Tafel extrapolation method. *Corrosion Science* 47 (12) 3202-3215.
160. Angal, R. (2010). *Principles and Prevention of Corrosion*: Alpha Science International, Limited.
161. Stupnišek-Lisac, E. (2007). *Korozija i zaštita konstrukcijskih materijala*. FKIT, Zagreb.
162. ASTM G1-03 (2011). Standard practice for preparing, cleaning, and evaluating corrosion test specimens. ASTM International, West Conshohocken, PA.
163. ASTM G30-97 (2009). Standard Practice for Making and Using U-Bend Stress-Corrosion Test Specimen. ASTM International, West Conshohocken, PA.
164. Brunelli, K., et al. (2005). Effect of HCl pre-treatment on corrosion resistance of cerium-based conversion coatings on magnesium and magnesium alloys. *Corrosion Science* 47 (4) 989-1000.
165. Scotto, V. and M. E. Lai (1998). The ennoblement of stainless steels in seawater: a likely explanation coming from the field. *Corrosion Science* 40 (6) 1007-1018.
166. Lloydis, A. C., et al. (2005). The open-circuit ennoblement of alloy C-22 and other Ni-Cr-Mo alloys. *JOM* 57(1) 31-35.

167. Frateur, I., et al. (1999). Modeling of the cast iron/drinking water system by electrochemical impedance spectroscopy. *Electrochimica Acta* 44 (24) 4345-4356.
168. Markhali, B. P., et al. (2013). Electrochemical impedance spectroscopy and electrochemical noise measurements as tools to evaluate corrosion inhibition ofazole compounds on stainless steel in acidic media. *Corrosion Science* 75 269-279.
169. Bentiss, F., et al. (2009). Enhanced corrosion resistance of carbon steel in normal sulfuric acid medium by some macrocyclic polyether compounds containing a 1,3,4-thiadiazole moiety: AC impedance and computational studies. *Corrosion Science* 51 (9) 2165-2173.
170. Lin, C. H. and J. G. Duh (2009). Electrochemical impedance spectroscopy (EIS) study on corrosion performance of CrAlSiN coated steels in 3.5 wt% NaCl solution. *Surface and Coatings Technology* 204 (6-7) 784-787.
171. Zhao, G., et al. (2009). Formation Characteristic of CO₂ Corrosion Product Layer of P110 Steel Investigated by SEM and Electrochemical Techniques. *Journal of Iron and Steel Research, International* 16 (4) 89-94.
172. Flitt, H. J. and D. P. Schweinsberg (2005). Evaluation of corrosion rate from polarisation curves not exhibiting a Tafel region. *Corrosion Science* 47 (12) 3034-3052.
173. Beverskog, B. and I. Puigdomenech (1996). Revised pourbaix diagrams for iron at 25–300 °C. *Corrosion Science* 38 2121-2135.
174. Luo, C. and Q. Su (2013). Corrosion of carbon steel in concentrated LiNO₃ solution at high temperature. *Corrosion Science* 74 290-296.
175. Sabioni, A. C. S., et al. (1992). Self-diffusion in Cr₂O₃ I. Chromium diffusion in single crystals. *Philosophical Magazine A* 66 (3) 333-350.
176. Poorqasemi, E., et al. (2009). Investigating accuracy of the Tafel extrapolation method in HCl solutions. *Corrosion Science* 51 (5) 1043-1054.
177. Groisman, A. S. and N. E. Khomutov (1990). Solubility of oxygen in electrolyte solutions. *Russian Chemical Reviews* 59 (8) 707.
178. Schumpe, A., I. Adler and W. D. Deckwer (1978). Solubility of oxygen in electrolyte solutions. *Biotechnology and Bioengineering* 20 (1) 145-150.

179. Lang, W. and R. Zander (1986). Salting-out of oxygen from aqueous electrolyte solutions: prediction and measurement. *Industrial & engineering chemistry fundamentals* 25 (4) 775-782.
180. Wallinder, D., I. O. Wallinder and C. Leygraf (2003). Influence of surface treatment of type 304L stainless steel on atmospheric corrosion resistance in urban and marine environments. *Corrosion* 59 (3) 220-227.
181. Lu, Y. F., et al. (1997). Mechanism of and method to avoid discoloration of stainless steel surfaces in laser cleaning. *Applied Physics A* 64 (6) 573-578.
182. Yang, Y., L. Guo and H. Liu (2011). The effect of temperature on corrosion behavior of SS316L in the cathode environment of proton exchange membrane fuel cells. *Journal of Power Sources* 196 (13) 5503-5510.
183. Yashiro, H., et al. (1998). The effect of permeated hydrogen on the pitting of type 304 stainless steel. *Ibid.* 40(4-5) 781-791.
184. Yang, Y., L. Guo and H. Liu (2011). The effect of temperature on corrosion behavior of SS316L in the cathode environment of proton exchange membrane fuel cells. *Journal of Power Sources* 196 (13) 5503-5510.
185. Pistorius, P. C. and G. T. Burstein (1992). Growth of corrosion pits on stainless steel in chloride solution containing dilute sulphate. *Corrosion Science* 33 (12) 1885-1897.
186. Pohjanne, P., et al. (2008). A method to predict pitting corrosion of stainless steels in evaporative conditions. *Journal of Constructional Steel Research* 64 (11) 1325-1331.
187. Ernst, P. and R. C. Newman (2002). Pit growth studies in stainless steel foils. II. Effect of temperature, chloride concentration and sulphate addition. *Corrosion Science* 44 (5) 943-954.
188. Yang, Y. Z., Y. M. Jiang and J. Li (2013). In situ investigation of crevice corrosion on UNS S32101 duplex stainless steel in sodium chloride solution. *Corrosion Science*. 76 163-169.
189. Machuca, L. L., et al. (2013). Effect of oxygen and biofilms on crevice corrosion of UNS S31803 and UNS N08825 in natural seawater. *Corrosion Science* 67 242-255.
190. Jakobsen, P. T. and E. Maahn (2001). Temperature and potential dependence of crevice corrosion of AISI 316 stainless steel. *Corrosion Science* 43 (9) 1693-1709.

191. Song, F. M. (2012). Predicting the chemistry, corrosion potential and corrosion rate in a crevice formed between substrate steel and a disbonded permeable coating with a mouth. *Corrosion Science* 55 107-115.
192. Hu, Q., et al. (2011). The crevice corrosion behaviour of stainless steel in sodium chloride solution. *Corrosion Science* 53 (12) 4065-4072.
193. Laycock, N. J., J. Stewart and R. C. Newman (1997). The initiation of crevice corrosion in stainless steels. *Corrosion Science* 39 (10-11) 1791-1809.
194. Turnbull, A. and S. Zhou (2008). Impact of temperature excursion on stress corrosion cracking of stainless steels in chloride solution. *Corrosion Science* 50 (4) 913-917.
195. Nakano, J., et al. (2014). Effects of temperature on stress corrosion cracking behavior of stainless steel and outer oxide distribution in cracks due to exposure to high-temperature water containing hydrogen peroxide. *Journal of Nuclear Materials* 444 (1-3) 454-461.
196. Lu, Z., et al. (2012). Characterization of microstructure, local deformation and microchemistry in Alloy 600 heat-affected zone and stress corrosion cracking in high temperature water. *Corrosion Science* 58 211-228.
197. Lu, Z., et al. (2008). Transient and steady state crack growth kinetics for stress corrosion cracking of a cold worked 316L stainless steel in oxygenated pure water at different temperatures. *Corrosion Science* 50 (2) 561-575.
198. Xu, L., et al. (2013). Corrosion of Cr bearing low alloy pipeline steel in CO₂ environment at static and flowing conditions. *Applied Surface Science* 270 395-404.
199. Jiang, X., Y. G. Zheng and W. Ke (2005). Effect of flow velocity and entrained sand on inhibition performances of two inhibitors for CO₂ corrosion of N80 steel in 3 % NaCl solution. *Corrosion Science* 47 (11) 2636-2658.
200. Galvan-Martinez, R., et al. (2009) Characterization of the Corrosion Kinetic of X52 Steel in Seawater with Biocides. *MRS Proceedings* [online].
201. Waanders, F. B., S. W. Vorster and G. J. Olivier (2002). Corrosion products formed on mild steel samples submerged in various aqueous solutions. *Hyperfine Interactions* 139 (1-4) 239-244.
202. ASTM G129 (2013). Standard Practice for Slow Strain Rate Testing to Evaluate the Susceptibility of Metallic Materials to Environmentally Assisted Cracking. ASTM International, West Conshohocken, PA.

Appendix B

List of Symbols

A	surface area	[m ²]
A ₈₀	elongation at fracture	[%]
B _a	anodic Tafel slope	[V/dec]
B _c	cathodic Tafel slope	[V/dec]
CPE	constant phase element	[S s ^α /m ²]
CR	corrosion rate	[mm/y]
C	true capacitance	[F/m ²]
E	Young's modulus	[Pa]
E	potential	[V]
E°	redox potential	[V]
E _{corr}	free corrosion potential	[V]
E _{oc}	open circuit potential	[V]
E _{pit}	pitting potential	[V]
E _{rep}	repassivation potential	[V]
EC	conductivity	[S/m]
f	frequency	[Hz]
F	Faraday constant	[1 F = 96 485 C/mol]
i	current	[A]
j	current density	[A/m ²]
j _{corr}	corrosion current density	[A/m ²]
M	molar mass	[g/mol]

m	mass	[kg]
Q	CPE admittance	[S s ^{α} /m ²]
R	resistance	[Ω]
R_s	solution resistance	[Ω]
$R_{p0.2}$	yield strength	[Pa]
R_m	tensile strength	[Pa]
t	time	[s]
T	temperature	[°C]
z	number of electrons	-
Z	impedance	[Ω]
Z'	real impedance	[Ω]
Z''	imaginary impedance	[Ω]
α	CPE empirical parameter	-
θ	phase angle	[°]
ν	Poisson's Ratio	-
ρ	density	[kg/m ³]
σ	stress	[Pa]

Appendix C

List of Figures

Figure 2.1 Structure of the Earth and the average geothermal gradient.....	6
Figure 2.2 Geothermal system – geothermal fluid exploitation.....	6
Figure 2.3 Operating geothermal fields in Indonesia.....	7
Figure 2.4 Uniform corrosion	16
Figure 2.5 Pitting corrosion.....	17
Figure 2.6 Crevice corrosion.....	18
Figure 2.7 Stress corrosion cracking	19
Figure 2.8 Temperature influence on corrosion of carbon steel in pure water (A) and neutral aqueous solutions of electrolyte (B).....	21
Figure 2.9 Influence of solution acidity on corrosion of steel.....	23
Figure 2.10 Influence of dissolved oxygen concentration in water of high purity on corrosion rate of carbon steel.....	24
Figure 3.1 Equivalent electrical circuits used for fitting the results obtained by EIS and their physical interpretation	33
Figure 3.2 Principle of Tafel extrapolation technique	34
Figure 3.3 Principle of cyclic polarization technique.....	35

Figure 3.4 Schematic illustration of the electrodes (A) and coupons (B) used for electrochemical and exposure testing, respectively	37
Figure 3.5 Schematic illustration of the pre-formed (A) and U-bend (B) coupons for SCC	38
Figure 3.6 Microscopic view of the metals surface after the surface treatment and prior to the corrosion investigations	39
Figure 3.7 Material sample test setup for: A) electrochemical tests, B) crevice corrosion tests using electrochemical methods, C) SCC in exposure tests, D) exposure tests	39
Figure 4.1 Monitoring of open circuit potential of 1.7218 steel in the artificial SBY geothermal brine at 100 °C during a 10-day immersion test.....	42
Figure 4.2 Typical impedance spectra for 1.7218 in the artificial SBY geothermal brine at 100 °C under E_{oc} conditions as a function of immersion time	43
Figure 4.3 Corrosion rates of low-alloyed steel 1.7218 in the artificial SBY geothermal brine at 100 °C during a 6-month exposure test	45
Figure 4.4 Cross section of 1.7218 coupons after 1 and 6 months of exposure in the artificial SBY geothermal brine at 100 °C.....	45
Figure 4.5 Open circuit potentials of low-alloyed steel 1.7218 in the artificial SBY geothermal brine at different temperatures.....	46
Figure 4.6 Typical impedance spectra for 1.7218 steel in the artificial SBY geothermal brine at different temperatures under E_{oc} conditions.....	47
Figure 4.7 Typical cathodic and anodic polarization curves of low-alloyed steel 1.7218 in artificial SBY geothermal brine at different temperatures	49
Figure 4.8 Corrosion rates of 1.7218 steel after exposure in the artificial SBY geothermal brine at different temperatures.....	51
Figure 4.9 Appearance of 1.7218 coupons after 6 months of exposure in the artificial SBY geothermal brine at 100 °C and 175 °C, respectively	51
Figure 4.10 Cross section of 1.7218 coupons after 6 months of exposure in the artificial SBY geothermal brine at 100 °C and 175 °C, respectively	52
Figure 4.11 Comparison of the corrosion rates obtained by the weight loss method after 6-month exposure test and Tafel extrapolation method	52
Figure 4.12 Open circuit potentials for 1.7218 after 20 h of immersion at 175 °C in the artificial geothermal brine pH 2 (LHD-23) and pH 4 (SBY), respectively	53

Figure 4.13 Typical impedance spectra for 1.7218 at 175 °C under E_{oc} conditions in the artificial geothermal brine pH 2 (LHD-23) and pH 4 (SBY), respectively	55
Figure 4.14 Typical cathodic and anodic polarization curves of 1.7218 in the artificial geothermal brine pH 2 (LHD-23) and pH 4 (SBY), respectively	56
Figure 4.15 Corrosion rates of 1.7218 after exposure at 175 °C in artificial geothermal brine pH 2 and pH 4, respectively	58
Figure 4.16 Appearance of 1.7218 coupons after 6 months of exposure at 175 °C in the artificial geothermal brine pH 2 (LHD-23) and pH 4 (SBY), respectively	58
Figure 4.17 Cross section of 1.7218 coupons after 6 months of exposure at 175 °C in the artificial geothermal brine pH 2 (LHD-23) and pH 4 (SBY), respectively	59
Figure 4.18 Open circuit potentials of 1.7218 after 20 h of immersion at 175 °C in the artificial geothermal brine containing 20 mg/L (LHD-05) and 1,500 mg/L (SBY) chlorides	59
Figure 4.19 Typical impedance spectra for 1.7218 at 175 °C under E_{oc} conditions in the artificial geothermal brine containing 20 mg/L (LHD-05) and 1,500 mg/L (SBY) chlorides	61
Figure 4.20 Typical cathodic and anodic polarization curves of 1.7218 at 175 °C in the artificial geothermal brine containing 20 mg/L (LHD-05) and 1,500 mg/L (SBY) chlorides	62
Figure 4.21 Corrosion rates of 1.7218 after exposure at 175 °C in the artificial geothermal brine containing 20 mg/L (LHD-05) and 1,500 mg/L (SBY) chlorides, respectively	63
Figure 4.22 Appearance of 1.7218 coupons after 6 months of exposure at 175 °C in the artificial geothermal brine containing 20 mg/L (LHD-05) and 1,500 mg/L (SBY) chlorides	64
Figure 4.23 Cross section of 1.7218 coupons after 6 months of exposure at 175 °C in the artificial geothermal brine containing 20 mg/L (LHD-05) and 1,500 mg/L (SBY) chlorides	64
Figure 4.24 Typical cathodic and anodic polarization curves of 1.7218 with and without the crevice simulation in the artificial SBY geothermal brine at 100 °C	65
Figure 4.25 Appearance of 1.7218 electrode after the cyclic polarization in the artificial SBY geothermal brine at 100 °C with and without the crevice simulation, respectively	65
Figure 4.26 Calculated tensile stress in 1.7218 U-bend coupon just before the break point (A) and appearance of the broken coupon (B).....	66
Figure 5.1 Monitoring of open circuit potential of 1.4404 steel in the artificial SBY geothermal brine at 100 °C during a 10-day immersion test.....	68
Figure 5.2 Typical impedance spectra for 1.4404 in the artificial SBY geothermal brine at 100 °C under E_{oc} conditions as a function of immersion time.....	69

Figure 5.3 Typical cyclic polarization curves of 1.4404 after 1 and 10 days of immersion in the artificial SBY geothermal brine at 100 °C.....	70
Figure 5.4 Appearance of 1.4404 coupon after 6 months of exposure in the artificial SBY geothermal brine at 100 °C.....	71
Figure 5.5 Open circuit potentials of 1.4404 steel in the artificial SBY geothermal brine at different temperatures	72
Figure 5.6 Typical impedance spectra for 1.4404 steel in the artificial SBY geothermal brine at different temperatures under E_{oc} conditions.....	73
Figure 5.7 Typical cyclic polarization curves of 1.4404 in the artificial SBY geothermal brine at different temperatures	74
Figure 5.8 Appearance of 1.4404 electrodes after cyclic polarization in the artificial SBY geothermal brine at different temperatures.....	75
Figure 5.9 Amount and average width-to-depth ratio of the pits observed on 1.4404 after cyclic polarization in the artificial SBY geothermal brine at different temperatures.....	76
Figure 5.10 Appearance of 1.4404 coupons after 6 months of exposure in the artificial SBY geothermal brine at 100 °C and 175 °C, respectively	77
Figure 5.11 Surface of 1.4404 coupons after 6 months of exposure in the artificial SBY geothermal brine at 100 °C and 175 °C, respectively	77
Figure 5.12 Open circuit potentials for 1.4404 after 20 h of immersion at 175 °C in the artificial geothermal brine pH 2 (LHD-23) and pH 4 (SBY), respectively	78
Figure 5.13 Typical impedance spectra for 1.4404 at 175 °C under E_{oc} conditions in the artificial geothermal brine pH 2 (LHD-23) and pH 4 (SBY), respectively	79
Figure 5.14 Typical cyclic polarization curve of 1.4404 at 175 °C in the solution pH 2 (LHD-23) and pH 4 (SBY), respectively.....	81
Figure 5.15 Appearance of 1.4404 electrodes after the cyclic polarization test at 175 °C in the solution pH 2 (LHD-23) and pH 4 (SBY), respectively	82
Figure 5.16 Amount and average width-to-depth ratio of the pits observed on 1.4404 after cyclic polarization in the solution pH 2 (LHD-23) and pH 4 (SBY) at 175 °C, respectively.....	82
Figure 5.17 Calculated corrosion rates and measured pits depth of 1.4404 after exposure in the artificial geothermal brine pH 2 (LHD-23) at 175 °C.....	83
Figure 5.18 Appearance of 1.4404 coupons after 6 months of exposure in the artificial geothermal brine pH 2 (LHD-23) and pH 4 (SBY), respectively	84

Figure 5.19 Surface (A) and cross section (B) of 1.4404 coupons after 6 months of exposure in the artificial geothermal brine pH 2 (LHD-23).....	84
Figure 5.20 Open circuit potentials of 1.4404 after 20 h of immersion at 175 °C in the artificial geothermal brine containing 20 mg/L (LHD-05) and 1,500 mg/L (SBY) chlorides	85
Figure 5.21 Typical impedance spectra for 1.4404 at 175 °C under E_{oc} conditions in the artificial geothermal brine containing 20 mg/L (LHD-05) and 1,500 mg/L (SBY) chlorides	86
Figure 5.22 Typical cyclic polarization curve of 1.4404 at 175 °C in the artificial geothermal brine containing 20 mg/L (LHD-05) and 1,500 mg/L (SBY) chlorides, respectively	88
Figure 5.23 Appearance of 1.4404 electrodes after the cyclic polarization test at 175 °C in the artificial geothermal brine containing 20 mg/L (LHD-05) and 1,500 mg/L (SBY) chlorides	89
Figure 5.24 Average amount and width-to-depth ratio of the pits observed on 1.4404 electrodes after cyclic polarization at 175 °C in artificial geothermal brine containing 20 mg/L (LHD-05) and 1,500 mg/L (SBY) chlorides, respectively	90
Figure 5.25 Typical cyclic polarization curve of 1.4404 in the artificial SBY geothermal brine at 100 °C with and without the crevice simulation, respectively	91
Figure 5.26 Appearance of 1.4404 electrode after the cyclic polarization in the artificial SBY geothermal brine at 100 °C with and without the crevice simulation, respectively	92
Figure 5.27 Surface relaxation of 1.4404 coupons with temperature application	93
Figure 5.28 Calculated tensile stress on the surface of 1.4404 U-bend coupon at 20 °C (A) and 175 °C (B), respectively	93
Figure 5.29 Surface (A) and cross section (B) of U-bend 1.4404 steel coupons after 6 months of exposure at 175 °C in the artificial LHD-23 geothermal brine.....	94
Figure 6.1 Monitoring of open circuit potential of 1.4562 steel in the artificial SBY geothermal brine at 100 °C during a 11-day immersion test.....	96
Figure 6.2 Typical impedance spectra for 1.4562 in the artificial SBY geothermal brine at 100 °C under E_{oc} conditions as a function of immersion time.....	97
Figure 6.3 Typical cyclic polarization curves of 1.4562 after 1 and 11 days of immersion in the artificial SBY geothermal brine at 100 °C.....	98
Figure 6.4 Appearance of 1.4562 coupon after 6 months of exposure in the artificial SBY geothermal brine at 100 °C.....	99
Figure 6.5 Open circuit potentials of 1.4562 steel in the artificial SBY geothermal brine at different temperatures	99

Figure 6.6 Typical impedance spectra for 1.4562 steel in the artificial SBY geothermal brine at different temperatures under E_{oc} conditions.....	101
Figure 6.7 Typical cyclic polarization curves of 1.4562 in the artificial SBY geothermal brine at different temperatures	102
Figure 6.8 Appearance of 1.4562 electrode surface after anodic polarization in artificial SBY geothermal brine at different temperatures.....	103
Figure 6.9 Amount and average width-to-depth ratio of the pits observed on 1.4562 after cyclic polarization in the artificial SBY geothermal brine at different temperatures.....	104
Figure 6.10 Appearance of 1.4562 coupons after 6 months of exposure in the artificial SBY geothermal brine at 100 °C and 175 °C, respectively	105
Figure 6.11 Surface of 1.4562 coupons after 6 months of exposure in the artificial SBY geothermal brine at 100 °C and 175 °C, respectively	105
Figure 6.12 Open circuit potentials for 1.4562 after 20 h of immersion at 175 °C in the artificial geothermal brine pH 2 (LHD-23) and pH 4 (SBY), respectively	106
Figure 6.13 Typical impedance spectra for 1.4562 at 175 °C under E_{oc} conditions in the artificial geothermal brine pH 2 (LHD-23) and pH 4 (SBY), respectively	107
Figure 6.14 Typical cyclic polarization curve of 1.4562 at 175 °C in the artificial geothermal brine pH 2 (LHD-23) and pH 4 (SBY), respectively.....	108
Figure 6.15 Appearance of 1.4562 electrode after the cyclic polarization test at 175 °C in the artificial geothermal brine pH 2 (LHD-23) and pH 4 (SBY), respectively	109
Figure 6.16 Amount and average width-to-depth ratio of the pits observed on 1.4562 after cyclic polarization in the solution pH 2 (LHD-23) and pH 4 (SBY) at 175 °C, respectively...	110
Figure 6.17 Calculated corrosion rates and measured pits depth of 1.4562 after exposure in the artificial geothermal brine pH 2 at 175 °C	111
Figure 6.18 Appearance of 1.4562 coupons after 6 months of exposure in the artificial geothermal brine pH 2 (LHD-23) and pH 4 (SBY), respectively	112
Figure 6.19 Surface (A) and cross section (B) of 1.4562 coupons after 6 months of exposure in the artificial geothermal brine pH 2 (LHD-23).....	112
Figure 6.20 Open circuit potentials of 1.4562 after 20 h of immersion at 175 °C in the artificial geothermal brine containing 20 mg/L (LHD-05) and 1,500 mg/L (SBY) chlorides	113
Figure 6.21 Typical impedance spectra for 1.4562 at 175 °C under E_{oc} conditions in the artificial geothermal brine containing 20 mg/L (LHD-05) and 1,500 mg/L (SBY) chlorides ..	114

Figure 6.22 Typical cyclic polarization curves of 1.4562 at 175 °C in the artificial geothermal brine containing 20 mg/L (LHD-05) and 1,500 mg/L (SBY) chlorides, respectively	115
Figure 6.23 Appearance of 1.4562 electrodes after the cyclic polarization test at 175 °C in the artificial geothermal brine containing 20 mg/L (LHD-05) and 1,500 mg/L (SBY) chlorides ..	116
Figure 6.24 Average amount and width-to-depth ratio of the pits observed on 1.4562 electrodes after cyclic polarization at 175 °C in artificial geothermal brine containing 20 mg/L (LHD-05) and 1,500 mg/L (SBY) chlorides, respectively	117
Figure 6.25 Typical cyclic polarization curve of 1.4562 in the artificial SBY geothermal brine at 100 °C with and without the crevice simulation, respectively	118
Figure 6.26 Appearance of 1.4562 electrode after the cyclic polarization in the artificial SBY geothermal brine at 100 °C with and without the crevice simulation, respectively	119
Figure 6.27 Surface relaxation of 1.4562 coupons with temperature application	119
Figure 6.28 Calculated tensile stress on the surface of 1.4562 U-bend coupon at 20 °C (A) and 175 °C (B), respectively	120
Figure 6.29 Surface (A) and cross section (B) of U-bend 1.4562 steel coupons after 6 months of exposure at 175 °C in the artificial LHD-23 geothermal brine.....	120
Figure 7.1 Overview and comparison of the results obtained with electrochemical methods for the selected materials 1.7218, 1.4404 and 1.4562 in the artificial geothermal brines.....	122

Appendix D

List of Tables

Table 2.1 Characteristics of the brines produced from the wells SBY (SBY-03 and SBY-05), LHD-05 and LHD-23 on the geothermal fields Sibayak and Lahendong	9
Table 2.2 The list of known iron oxides.....	13
Table 3.1 Equivalent grades of the selected materials.....	28
Table 3.2 Chemical composition of the selected materials in wt% (Fe bal.)	29
Table 3.3 Mechanical properties of the selected materials	29
Table 3.4 Chemical composition and the resulting acidity of the artificial geothermal brines.	30
Table 4.1 Electrochemical data obtained by EIS for 1.7218 during a 10-day immersion test in the artificial SBY geothermal brine at 100 °C under E_{oc} conditions	44
Table 4.2 Electrochemical data obtained by EIS for 1.7218 in the artificial SBY geothermal brine under E_{oc} conditions at different temperatures	48
Table 4.3 Electrochemical data for 1.7218 obtained by Tafel extrapolation method in the artificial SBY geothermal brine at different temperatures	50
Table 4.4 Electrochemical data obtained by EIS for 1.7218 at 175 °C under E_{oc} conditions in the artificial geothermal brine pH 2 (LHD-23) and pH 4 (SBY), respectively	55
Table 4.5 Electrochemical data of 1.7218 in the artificial SBY and LHD-23 geothermal brines at 175 °C obtained by Tafel extrapolation method	57

Table 4.6 Electrochemical data of 1.7218 determined from the polarization curves at 175 °C in the artificial geothermal brine containing 20 mg/L (LHD-05) and 1,500 mg/L (SBY) chlorides.....	62
Table 4.7 Electrochemical data of 1.7218 determined from the polarization curves in the artificial SBY geothermal brine at 100 °C with and without the crevice simulation, respectively	66
Table 5.1 Electrochemical data obtained by EIS for 1.4404 during a 10-day immersion test in the artificial SBY geothermal brine at 100 °C under E_{oc} conditions	69
Table 5.2 Electrochemical data of 1.4404 determined from the cyclic polarization curves after 1 and 10 days of immersion in the artificial SBY geothermal brine at 100 °C.....	70
Table 5.3 Electrochemical data obtained by EIS for 1.4404 in the artificial SBY geothermal brine under E_{oc} conditions at different temperatures	73
Table 5.4 Electrochemical data of 1.4404 determined from the cyclic polarization curves in the artificial SBY geothermal brine at different temperatures	74
Table 5.5 Characterization of the pits observed on 1.4404 electrode surface in the artificial SBY geothermal brine at different temperatures	75
Table 5.6 Electrochemical data obtained by EIS for 1.4404 at 175 °C under E_{oc} conditions in the artificial geothermal brine pH 2 (LHD 23) and pH 4 (SBY), respectively.....	80
Table 5.7 Electrochemical data of 1.4404 determined from the cyclic polarization at 175 °C in the solution pH 2 (LHD-23) and pH 4 (SBY), respectively.....	81
Table 5.8 Characterization of the pits observed on 1.4404 electrode surface after the cyclic polarization test in the solution pH 2 (LHD-23) and pH 4 (SBY) at 175 °C, respectively.....	82
Table 5.9 Electrochemical data obtained by EIS for 1.4404 at 175 °C under E_{oc} in the artificial geothermal brine containing 20 mg/L (LHD-05) and 1,500 mg/L (SBY) chlorides	87
Table 5.10 Electrochemical data of 1.4404 determined from cyclic polarization at 175 °C in the solution containing 20 mg/L (LHD-05) and 1,500 mg/L (SBY) chlorides.....	88
Table 5.11 Characterization of the pits observed on 1.4404 electrode surface after the cyclic polarization test at 175 °C in the artificial geothermal brine containing 20 mg/L (LHD-05) and 1,500 mg/L (SBY) chlorides, respectively	90
Table 5.12 Electrochemical data of 1.4404 determined from the cyclic polarization in the artificial SBY geothermal brine at 100 °C with and without the crevice simulation	91

Table 6.1 Electrochemical data obtained by EIS for 1.4562 during a 11-day immersion test in the artificial SBY geothermal brine at 100 °C under E_{oc} conditions	97
Table 6.2 Electrochemical data of 1.4562 determined from the cyclic polarization curves after 1 and 11 days of immersion in the artificial SBY geothermal brine at 100 °C.....	98
Table 6.3 Electrochemical data obtained by EIS for 1.4562 in the artificial SBY geothermal brine under E_{oc} conditions at different temperatures	101
Table 6.4 Electrochemical data of 1.4562 determined from the cyclic polarization curves in the artificial SBY geothermal brine at different temperatures	103
Table 6.5 Characterization of the pits observed on 1.4562 electrode surface after cyclic polarization in the artificial SBY geothermal brine at different temperatures	104
Table 6.6 Electrochemical data obtained by EIS for 1.4562 at 175 °C under E_{oc} conditions in the artificial geothermal brine pH 2 (LHD-23) and pH 4 (SBY), respectively	107
Table 6.7 Electrochemical data of 1.4562 determined from the cyclic polarization at 175 °C in the artificial geothermal brine pH 2 (LHD-23) and pH 4 (SBY), respectively	109
Table 6.8 Characterization of the pits observed on 1.4562 electrode surface after the cyclic polarization test in the solution pH 2 (LHD-23) and pH 4 (SBY) at 175 °C, respectively.....	110
Table 6.9 Electrochemical data obtained by EIS for 1.4562 at 175 °C under E_{oc} in the artificial geothermal brine containing 20 mg/L (LHD-05) and 1,500 mg/L (SBY) chlorides	114
Table 6.10 Electrochemical data of 1.4562 determined from cyclic polarization at 175 °C in the solution containing 20 mg/L (LHD-05) and 1,500 mg/L (SBY) chlorides.....	116
Table 6.11 Characterization of the pits observed on 1.4562 electrode surface after the cyclic polarization test at 175 °C in the artificial geothermal brine containing 20 mg/L (LHD-05) and 1,500 mg/L (SBY) chlorides, respectively	117
Table 6.12 Electrochemical data of 1.4562 determined from the cyclic polarization in the artificial SBY geothermal brine at 100 °C with and without the crevice simulation	118
Table 7.1 Overview of the results after 6 months of exposure	124
Table 8.1 Results summary matrix of the performed experiments and their evaluation.....	129

Appendix E

Publications

E.1 Journals

Keserovic A., Bäßler R. Material evaluation for application in geothermal systems in Indonesia. *Materials Performance* (in revision)

Keserovic A., Bäßler R. Suitability of UNS S31603 steel for geothermal brines in volcanic areas - Influence of different physicochemical conditions on its corrosion behavior. *Geothermics* (in revision)

E.2 Conferences

E.1.1 Papers

Keserovic A., Bäßler R. (2015). Geothermal systems of Indonesia – Influence of different factors on the corrosion performance of carbon steel API Q125. World Geothermal Congress (WGC 2015), Melbourne, Australia (in revision).

Bäßler R., Keserovic A., Sobetzki J., Sarmiento Klapper H. (2014). Materials Evaluation for Geothermal Applications. 9th International Materials Technology Conference & Exhibition (IMTCE2014), Kuala Lumpur, Malaysia.

Keserovic A., Bäßler R., Kamah Y. (2014). Suitability of alloyed steels in highly acidic geothermal environments. NACE Corrosion 2014, paper no. 4031, San Antonio, TX.

Keserovic A., Bäßler R. (2013). Material evaluation for application in geothermal systems in Indonesia. NACE Corrosion 2013, paper no. 2269, Orlando, FL.

E.1.2 Presentations

Keserovic A., Bäßler R., Kamah Y. (2014). Suitability of alloyed steels in highly acidic geothermal environments. NACE Corrosion 2014, San Antonio, TX.

Keserovic A., Bäßler R. (2013). Results of corrosion study in artificial geothermal brine in volcanic area. International Geothermal Conference, Bandung, Indonesia.

Keserovic A., Bäßler R. (2013). Corrosion performance of different steel grades in highly acidic geothermal brine in Indonesia”, Eurocorr 2013, Estoril, Portugal.

Keserovic A., Bäßler R. (2013). Electrochemical behavior of different steel grades in low pH geothermal brines. 2nd International Conference on Materials for Energy, Karlsruhe, Germany.

Keserovic A., Bäßler R. (2013). Material evaluation for application in geothermal systems in Indonesia. NACE Corrosion 2013, Orlando, FL.

Keserovic A., Bäßler R. (2012). Contribution to material qualification for geothermal application. Eurocorr 2012, Istanbul, Turkey.

E.1.3 Posters

Keserovic A., Bäßler R. (2013). Corrosion performance of steel grades in artificial LHD-23 acidic brine. International Geothermal Conference, Bandung, Indonesia.

Keserovic A., Bäßler R. (2012). Korrosionsverhalten von metallischen Werkstoffen für den Einsatz in geothermischen Anlagen in Indonesien. GTV, Karlsruhe, Germany.

Keserovic A., Bäßler R. (2012). Korrosionsverhalten von metallischen Werkstoffen für den Einsatz in geothermischen Anlagen in Indonesien. GfKORR annual conference, Frankfurt, Germany.

E.1.4 Awards

(2012) “Best poster” prize. GfKORR annual conference, Frankfurt, Germany.

Appendix F

Acknowledgments

First and foremost, I thank my supervisor Dr. Ralph Bäßler for making my 26th birthday one of the most memorable ones by giving me the chance to conduct the Ph. D. research within the BAM's corrosion group, for supporting me during this time and for having so much understanding and patience through these years. I would also like to thank on a professional and personal level to all of my colleagues in Federal Institute for Materials Research and Testing (BAM), especially Dr. Oleksandra Yevtushenko; for her valuable advices, encouragement and emotional support through the hard times, Rita Karras; for the metallographic analysis and all those nice complements she frequently gave me, Thomas Schneider; for the support in the lab, Dr. Eichler Thorsten for help with EIS data interpretation and Ulrich Klein; for his enviable engineering capabilities to repair all of my broken goods. ☺

Special thanks go to the professors Dr. Ernst Huenges and Dr. Uwe Tröger for reviewing my thesis and their inputs.

I would also like to express my sincere gratitude to all of my colleagues in German Research Centre for Geosciences (GFZ), especially within the project, for the unforgettable social activities, technical support on the fieldtrips and with the PhD thesis submission procedure, their kindness, patience, and tolerance of my energetic character. Some of them are (in the alphabetical order!): Muhamad Andhika, Maren Brehme, Dr. Fiorenza Deon, Dr. Kemal Erbaş, Dr. Alireza Hassanzadegan, Dr. Simona Regenspurg, Dr. Günter Zimmermann and many others...

My appreciation is also extended to the BPPT and PGE team in Jakarta, as well as at Sibayak and Lahendong sites, for allowing me the access to the data and the fields.

Finally, I owe a special gratitude to my family; my parents and my sister, and my caring boyfriend Mario for their continuous and unconditional support, encouragement and understanding.

The financial support of the German Federal Ministry of Education and Research, BMBF (03G0753A) is gratefully acknowledged.

Resume

Personal Data

Name	Amela Keserović
Date of birth	19 th August 1984
Place of Birth	Nikšić, Montenegro

Education

2003 – 2009	Master of Chemical Engineering Faculty of Chemical Engineering and Technology University of Zagreb, Croatia
1999 – 2003	Gymnasium Križanićeva 4 Zagreb, Croatia

Professional Experience

11/2010 – present	Research Scientist Federal Institute for Materials Research and Testing, Berlin, Germany
11/2010 – 12/2013	Research Scientist German Research Centre for Geosciences, Potsdam, Germany
09/2010 – 10/2010	Junior Scientist/Medical Chemist Galapagos Research Centre, Zagreb, Croatia
11/2009 – 08/2010	Junior Scientist/Medical Chemist GlaxoSmithKline Research Centre, Zagreb, Croatia
10/2008 – 12/2008	Research Scientist Cortec Corporation, St. Paul, Minnesota, USA
11/2003 & 01/2005	President of the Electorate on the political elections City Hall, Zagreb, Croatia
